Measurement of the Leptonic Angular Distribution in W-Boson Decay as a Function of the W Transverse-Momentum Using the CDF Detector at the Tevatron

a thesis by

Lucio Cerrito

Rutherford Appleton Laboratory

and

University College London

Submitted to the University of London
in fulfilment of the requirements
for the degree of Doctor of Philosophy

April 2002

Abstract

A measurement of the angular distribution of leptons from the analysis of W-boson decay data is presented.

Although the properties of the leptonic angular distribution from W decays have been studied extensively in the past decades, the amount of data collected at the Tevatron is sufficient to observe Quantum Chromo Dynamics (QCD) corrections. When QCD is included, the lepton polar-angle distribution is best described by two parameters, α_1 and α_2, functions of p_T^W:

$$\frac{\mathrm{d}\sigma}{\mathrm{d}\cos\theta^*} \propto (1 \pm \alpha_1 \cos\theta^* + \alpha_2 \cos^2\theta^*),$$

where θ^* is measured in the W rest-frame with respect to the proton beam. Both the W asymmetry measurement and the W mass precision measurement at CDF rely on the accurate understanding and simulation of the leptonic angular distribution.

The data analysed in this thesis, which include both the electron and the muon channels, were collected with the CDF detector at the Tevatron proton-antiproton collider during Run Ib (1994−1996). The coefficient α_2 of the polar-angle distribution is measured as a function of the W-boson transverse-momentum up to 100 GeV. The measurement strategy consists of fitting the transverse-mass distribution to a set of templates from a Monte Carlo event and detector simulation. A log-likelihood method is used to determine α_2.

The measured values of α_2 confirm the Standard Model expectation for the W-polarisation at high transverse-momentum. A study for a measurement of α_1 is also presented. However, there is insufficient sensitivity for the measurement of α_1 with the CDF Run I detector.

Acknowledgements

I would like to thank the Council of the Central Laboratory for the Research Councils (CCLRC) and the Rutherford Appleton Laboratory (RAL), for providing the financial support for my Ph.D. program. I am particularly in debt to my supervisor, Dr. Stephen Haywood (RAL). Stephen's comments, remarks and suggestions are present throughout this work and I really appreciated the way Stephen has been willing to discuss and help at anytime. A special thank to Dr. Mark Lancaster (UCL) for suggesting this analysis and providing most of the analysis code, documentation and help. I'm thankful to Prof. Ken Peach, director of the Particle Physics Department at RAL, and Dr. Bill Scott (RAL) for their attention and support to my work.

Many people have contributed, at different times, to boost my understanding and enthusiasm in the last two years. Dr. John Lane (UCL) introduced me to particle tracking. I had many helpful discussions with Dr. Aseet Mukharjee (Fermilab) on the physics and operations of the CDF main tracker. Dr. David Waters and Dr. Farrukh Azfar (Oxford) have been good colleagues and friends when I first arrived at Fermilab, in the United States. I enjoyed their friendship and much appreciated their help. I have benefited from David's comments and the discussions we had on this analysis. Dr. Rob Snihur (UCL) has been very encouraging.

I'm thankful to my fellow graduate students at Fermilab, with whom I enjoyed sharing both complaints and joys of living in the American Midwest. Finally, I would like to thank my parents for their constant encouragement.

Lucio Cerrito
Fermilab (USA) – March 2002

Contents

Introduction

Ever since the lepton angular distribution from W-boson decays was first studied in the decay of polarised Co^{60} nuclei [1], it has provided a handle for studying the structure of the electroweak current. The data collected by the CERN $Sp\bar{p}S$ collider, between 1982 and 1985, later confirmed that the $W \to e\nu$ angular distribution is consistent with the predictions of the Standard Model with a V−A electroweak current. That is, the polar-angle distribution of the outgoing electron corresponds to the decay of a fully polarised spin-1 boson coupled to left-handed fermions.

The Standard Model also predicts that when W-bosons are produced with high transverse-momentum (p_T^W), their polarisation is affected by initial-state gluon radiation and quark-gluon scattering. The lepton polar-angle distribution is best described by two parameters, α_1 and α_2, functions of p_T^W:

$$\frac{\mathrm{d}\sigma}{\mathrm{d}\cos\theta^*} \propto (1 \pm \alpha_1 \cos\theta^* + \alpha_2 \cos^2\theta^*).$$

In the equation above, θ^* is measured in the W rest-frame with respect to the proton beam. These effects, calculated in Quantum Chromo Dynamics (QCD) in terms of $\alpha_1(p_T^W)$ and $\alpha_2(p_T^W)$, should be visible when the transverse-momentum of the W's is about 20 GeV or higher.

The data available from the collisions produced by the Tevatron proton-antiproton machine, between 1989 and 1996, contains several thousand high-p_T W-bosons.

The CDF Run I detector collected the data from proton-antiproton collisions at a centre-of-mass energy[1] ($\sqrt{s}$) of 1.8 TeV.

Therefore, the analysis of the CDF data should allow the testing of the QCD expectations for the W polarisation. Moreover, as the lepton distribution is crucial for other electroweak measurements, like the W mass and the asymmetry in the W rapidity, the accurate understanding of the QCD corrections to the polar-angle distribution is very important to reduce systematics in those measurements.

This thesis is divided into 8 chapters. The first four chapters contain a description of the physics of the W-bosons, the CDF detector and a preliminary study of the measurement. The last four chapters describe the analysis of the data to determine the polar-angle distribution coefficients. The following is an outline of the chapters:

- Chapter 1 presents the phenomenology of W production and decay at a $p\bar{p}$ collider. It contains details of the lepton angular distribution from QCD, and the connection with other measurements within the electroweak-physics sector.

- Chapter 2 is a review of the detector and the accelerator. It describes the experimental apparatus (the CDF detector) and the accelerator facility (the Tevatron Collider).

- Chapter 3 is dedicated to the central tracker of CDF. It contains studies for the internal alignment of the CDF Run II tracking chamber (COT). The internal alignment of the tracker is a crucial aspect in precision electroweak-physics and in this analysis.

---

[1] The Tevatron started the Run II phase in 2001, after undergoing a machine upgrade to deliver higher luminosity and a centre-of -mass energy of $\sqrt{s}$=2.0 TeV.

- Chapter 4 contains the simulation of the measurement. It shows the measurement technique and the expected sensitivity.
- Chapter 5 opens the second part the thesis. The chapter presents the data handling and the event selection.
- Chapter 6 gives a description of the Monte Carlo event-simulation, with emphasis on those parts developed for this analysis. The simulation includes the W production and decay and the detector response.
- Chapter 7 presents the estimate of the background to the $W \to e\nu$ and $W \to \mu\nu$ event-candidates. Since the background changes the shape of the distributions used to extract the angular coefficients, it needs to be estimated and included in the simulation.
- Chapter 8 contains the results of the measurement of α_2 and a discussion on the prospects for a measurement of α_1.

A summary of the conclusions is given at the end of the thesis, after Chapter 8. My contribution to this work consists of:

- Studying the alignment of the COT, alongside the people involved in the drift-model calibration.
- All the work for the study of the angular distributions for the W decay. This has been based in part on the analysis for the W mass

Chapter 1

The Angular Distribution of Leptons from W-bosons

The chapter presents the basic elements of W production and leptonic decay at a proton-antiproton collider. The lepton angular distribution is discussed in detail in the simple version of the Quark Parton Model and Quantum Chromo Dynamics. The definition of several kinematic variables is given in Section 3. The last section contains a brief review of the relevance of the lepton angular distribution in electroweak physics.

1.1 Phenomenology of W production at a hadron collider

The W-bosons were first observed [7, 8, 9, 10, 11, 12, 13] in 1983 in high-energy experiments at the CERN (European Centre for Nuclear Research) proton-antiproton $Sp\bar{p}S$ collider. The particles colliding at a $p\bar{p}$ machine consist of quarks (q), antiquarks ($\bar{q}$) and gluons (g), the so-called "partons", each carrying a fraction of the total beam energy. The partons share the beam energy in such a way that about half of the proton momentum is carried by the gluons. The remaining part is carried by the valence-quarks and the sea-quarks. The invariant masses accessible in the collision of the partons $q\bar{q}$, qg, $\bar{q}g$ or gg are distributed from 0 to the total centre-of-mass energy ($\sqrt{s} = 2E_{beam}$). This distribution is approximately a decaying exponential. When the energy is sufficiently high, W-bosons (M_W=80.422±0.047 GeV)[1] [2, 3] are directly produced from the annihilation of a quark and an antiquark. Figure 1.1 shows the Feynman graph for a $p\bar{p}$ collision in which a quark (q) and an antiquark ($\bar{q}$) combine to form a W-boson, decaying via the weak interaction into a lepton (l) and a neutrino (ν_l).

The cross-section for the process $p\bar{p} \to W \to X + l + \nu_l$ (where l indicates a generic lepton) is therefore given by the parton-level cross-section ($\hat{\sigma}_{ij}$), convoluted with the distribution of quark momenta inside the proton:

$$\sigma = \sum_{i,j} \int \mathrm{d}x_i \mathrm{d}x_j f_i^h(x_i, Q^2) f_j^h(x_j, Q^2) \hat{\sigma}_{ij}(\hat{s}), \tag{1.1}$$

where i and j are indices for the colliding partons. The f functions are called parton distribution functions (PDF's) and express the probability of finding a parton of type i, within the hadron h, carrying a fraction x of the hadron momentum,

---

[1] For simplicity c will be set to 1 throughout this thesis, so that mass and momentum are expressed in GeV.

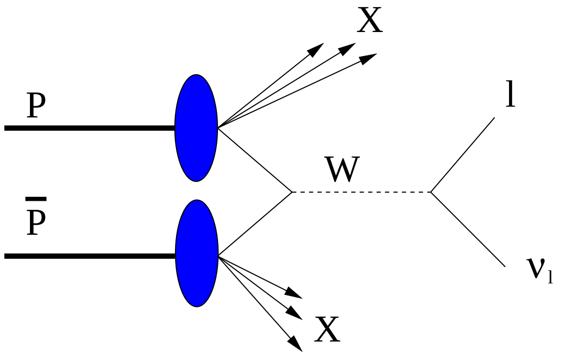

Figure 1.1: *Tree-diagram of the annihilation of quark and antiquark, from a proton-antiproton collision, that leads to direct W-boson production.*

at the energy-scale Q^2. The energy-scale Q^2 is set equal to $\hat{s} = x_i x_j s$. Modern PDF's are mostly measured from HERA [4] electron-proton collision data, but also constructed from muon, electron and neutrino scattering off nucleons, as well as from the Tevatron $p\bar{p}$ data.

The parton-level total cross-section $\hat{\sigma}_{ij}$ for $q_i \bar{q}_j \to W^+ \to e^+ \nu$ is given by [22, 15]:

$$\hat{\sigma}_{ij}(\hat{s}) = \frac{1}{3} \frac{|V_{ij}|^2}{3\pi} \left(\frac{G_F M_W^2}{\sqrt{2}} \right)^2 \frac{\hat{s}}{(\hat{s} - M_W^2)^2 + (\hat{s}\Gamma_W / M_W)^2}, \tag{1.2}$$

where M_W and Γ_W are the W-boson mass and width. The factor $\frac{1}{3}$ accounts for the requirement that the colliding partons must have the same colour, the $\hat{s}$ dependent term is the relativistic Breit-Wigner distribution that gives the resonance shape to the total cross-section. Equation 1.1, with Equation 1.2 expressing $\hat{\sigma}_{ij}$, is the production cross-section for W-bosons in proton-antiproton collisions. The W-bosons can decay subsequently into one of several channels. In the leptonic decay, the W produces a lepton (e, μ or τ) plus the corresponding lepton neutrino.

1.2 Angular distribution of leptons from W decay

The angular distribution of leptons from W-bosons is directly related to the behaviour of the electroweak (EW) current. As a consequence of the V−A structure of the charged weak current, the lepton is not produced isotropically in the W rest-frame.

Free-quark scattering:

In a simple free-quark scattering, the angular dependence is given according to the EW theory by the well known formula [16]:

$$\frac{\mathrm{d}\sigma^{l}}{\mathrm{d}\cos\theta} \propto (1 - Q \cdot \cos\theta)^2, \tag{1.3}$$

where θ is defined to be the charged lepton polar-angle in the W rest-frame, measured with respect to the direction of the quark, and Q is the lepton charge. The cross-section is maximal when the outgoing lepton (antilepton) moves in the direction of the incoming quark (antiquark). There is a simple angular momentum argument for this. Because in the massless limit of the Standard Model the W couples to negative helicity fermions and positive helicity antifermions, in the center-of-mass frame scattering proceeds from an initial state with $J_z = -1$ to a final state with $J_{z'} = -1$, where z, z' axes are along the ingoing quark and outgoing negatively-charged lepton directions respectively (see Figure 1.2).

The reaction proceeds via an intermediate W-boson of spin 1, and therefore the amplitude is proportional to the rotation matrix:

$$d^1_{-1-1}(\theta) = \frac{1}{2}\,(1 + \cos\theta)\,. \tag{1.4}$$

If the final state is a positively-charged lepton plus a neutrino then $J_{z'} = +1$, hence for l^+ the amplitude is proportional to the rotation matrix:

$$d^1_{-1+1}(\theta) = \frac{1}{2}\,(1 - \cos\theta)\,. \tag{1.5}$$

The square of the amplitudes gives the angular dependence in the cross-section of Equation 1.3, and embodies the requirement that the amplitude for the process of Figure 1.2 must vanish in the backward direction, because here the net helicity is not conserved.

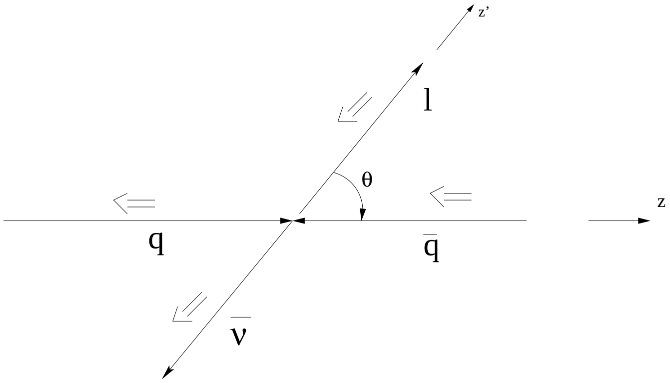

Figure 1.2: *Simple angular momentum conservation arguments explain why outgoing fermions are emitted preferentially in the direction of the incoming fermion, as shown here. The lepton moves away preferentially in the quark direction.*

Proton-antiproton scattering:

When W-bosons are produced by a collision of protons and antiprotons, instead of free fermions, the lepton angular distribution is the result of the sum of all the possible parton processes, therefore its structure is slightly more complex than Equation 1.3, and is given by:

$$\frac{\mathrm{d}\sigma^l}{\mathrm{d}\cos\theta} \propto \textit{valence} \text{ quarks} \times (1 - Q \cdot \cos\theta)^2 + \textit{sea} \text{ quarks} \times (1 + \cos^2\theta). \quad (1.6)$$

The role of the sea-quarks can be seen from Figure 1.3. When the scattering involves valence-quarks only, $W^{\pm}$ are always polarised opposite to the proton beam direction. Sea-quarks give instead either a same-polarity contribution or an opposite-polarity contribution, the latter when an antiquark from the proton collides with a quark from the antiproton. Since the same-polarity contribution and the opposite-polarity contribution are equally likely, the term in Equation 1.6 involving the sea-quarks has only a $\cos^2\theta$ dependence. The lepton angular distribution in the W rest-frame is shown in Figure 1.4. The distribution does not vanish at $\cos\theta{=}{+}1$ because of the sea-quarks contribution.

The laboratory frame:

The lepton angular distribution in the laboratory frame is the convolution of Equation 1.6 with the boost of the W. The W-bosons produced in $p\bar{p}$ collisions are not produced at rest in the lab-frame and show a forward-backward asymmetry. In other words, the rapidity distribution for W^+ and W^- is not symmetric around $y = 0$. Neglecting the sea-quark contribution, a W^+ is produced from the annihilation of a u quark from the proton with a $\bar{d}$ quark in the antiproton. Since u quarks in a proton carry more momentum than d quarks on average, the resulting W^+ will move preferably in the proton direction, and the W^- will be preferentially produced in the antiproton direction.

Before describing how Quantum Chromo Dynamics (QCD) modifies the lepton angular distribution from W-bosons, in Section 1.5, the next two sections will define some of the kinematic variables that will be used in the analysis in order to complete the description of the phenomenology of W production.

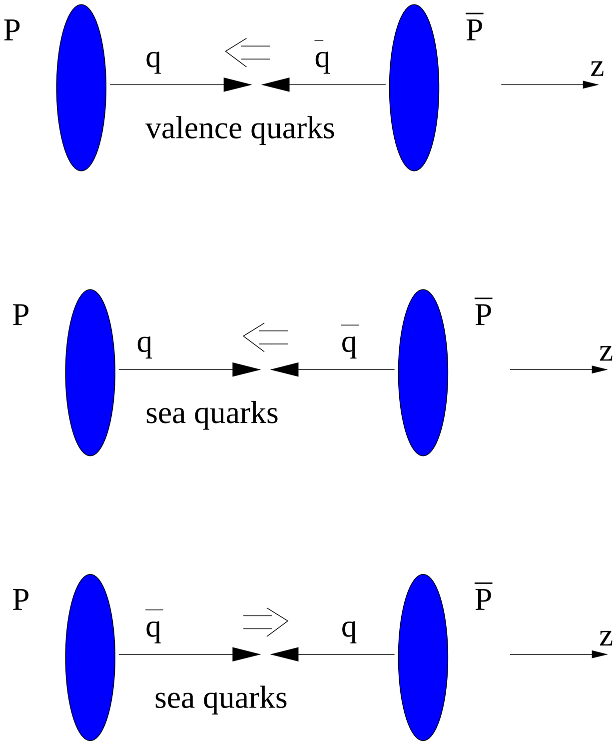

Figure 1.3: *The role of the sea-quarks in the polarisation of the W-bosons, indicated here with the arrow above the collision point. As a consequence of the collision between antiquarks from the proton and quarks from the antiproton (the sketch on the bottom), the lepton polar-angle distribution contains a term of opposite-polarity contribution.*

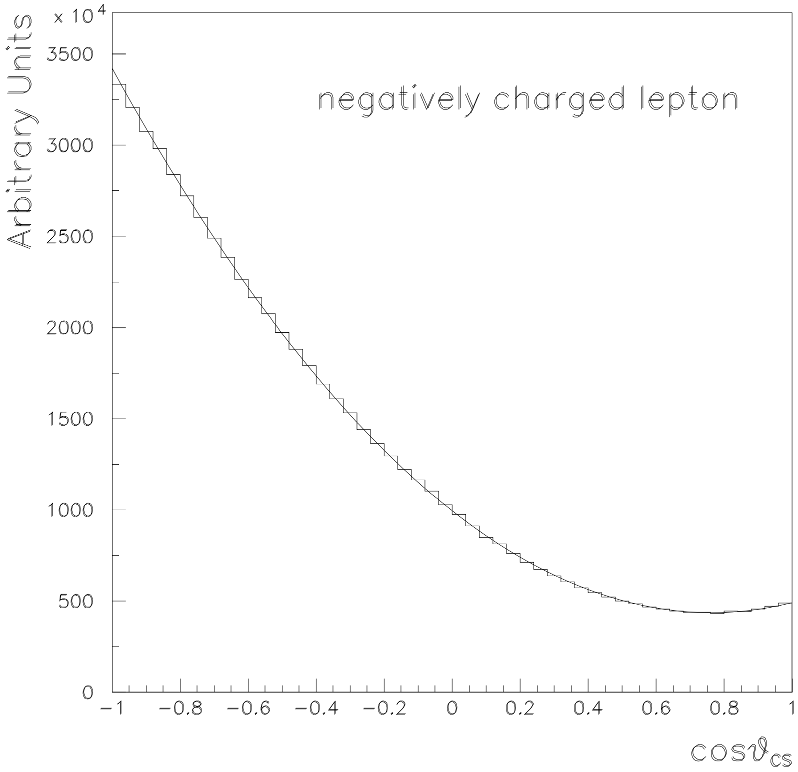

Figure 1.4: *Lepton angular distribution in the W rest-frame. The distribution is V−A plus a sea-quark component, as described by the set of parton distribution functions MRS-R1 [37].*

1.3 Kinematic variables

The centre-of-mass of the parton-parton scattering is normally boosted with respect to that of the two incoming hadrons, it is therefore useful to write the final state in terms of variables which transform simply under longitudinal boosts. For this reason the variables: rapidity (y), transverse-momentum (p_T) and azimuthal-angle (ϕ) are the most convenient. The four-momentum components of a particle of mass m may be written as:

$$\begin{aligned} p^\mu &= (E, p_x, p_y, p_z) \\ &= (m_T \cdot \mathrm{cosh}y, p_T \cdot \sin\phi, p_T \cdot \cos\phi, m_T \cdot \mathrm{sinh}y), \end{aligned} \tag{1.7}$$

where the transverse-mass is defined as $m_T = \sqrt{(p_T^2 + m^2)}$ and the rapidity y is defined by:

$$y = \frac{1}{2}\mathrm{ln}\left(\frac{E + p_z}{E - p_z}\right). \tag{1.8}$$

The rapidity y is additive under Lorentz boosts along the z-direction, i.e. rapidity differences are boost invariant. Often the rapidity is replaced by the pseudo-rapidity variable η:

$$\eta = -\mathrm{ln}\ \tan(\theta/2) \tag{1.9}$$

which coincides with the rapidity in the mass limit: $m \to 0$.

1.4 Transverse quantities and the Jacobian Edge

Since the proton remnants of a $p\bar{p}$ event are mostly undetected, the longitudinal momentum of the W is unmeasured, and the longitudinal momentum of the neutrino cannot be reconstructed or measured either. In fact the W rest-frame cannot be recovered from the measured kinematic quantities in the lab-frame.

Transverse quantities are used instead. In the W rest-frame, the angular distribution of the lepton, averaged over W^+ and W^- production, is:

$$\frac{1}{\sigma}\frac{\mathrm{d}\sigma}{\mathrm{d}\cos\theta} = \frac{3}{8}(1+\cos^2\theta), \tag{1.10}$$

Assuming that the W has zero transverse-momentum, then $\cos\theta$ is given in terms of the transverse-momentum (p_T^l) of the lepton by:

$$\cos\theta = \left(1 - \frac{4{p_T^l}^2}{M_W^2}\right)^{\frac{1}{2}}, \tag{1.11}$$

and inserting Equation 1.11 into Equation 1.10 gives the differential cross-section in the lepton transverse-momentum:

$$\frac{1}{\sigma}\frac{\mathrm{d}\sigma}{\mathrm{d}{p_T^l}^2} = \frac{3}{M_W^2}\left(1 - \frac{4{p_T^l}^2}{M_W^2}\right)^{-1/2}\left(1 - \frac{2{p_T^l}^2}{M_W^2}\right). \tag{1.12}$$

This distribution has a pole at $p_T^l = M_W/2$ (called the Jacobian peak), and can therefore provide a measurement of M_W. In practice the singularity of the distribution is smeared out by the finite width of the W resonance and by the non-zero transverse-momentum of the W. Including information about the missing transverse-momentum (i.e. the neutrino), by identifying magnitude and azimuthal-angle of the missing transverse-energy with the undetected neutrino, a distribution of transverse-mass (M_T) is obtained, which is less sensitive to the transverse-momentum of the W-boson:

$$M_T^2 = 2|p_T^l||p_T^\nu|(1-\cos\Delta\phi_{l\nu}). \tag{1.13}$$

At leading order and without any quark transverse-momentum, it follows that $|p_T^l| = |p_T^\nu|$, $\Delta\phi_{l\nu} = \pi$ and $M_T = 2|p_T^l|$. Hence, the transverse-mass distribution also has a Jacobian peak, like the lepton transverse-momentum distribution, at $M_T = M_W$. The shape of the distribution of the transverse-mass is used in proton-antiproton collider experiments to measure the mass of the W-boson.

1.5 QCD corrections to the lepton angular distribution

In the previous sections of this chapter it was explained how, in the parton model, W-bosons are produced in head-on collisions of $q\bar{q}$ constituents of the proton and antiproton. The Feynman diagram is a tree-level diagram, as in Figure 1.1. Moreover, in the simple picture of the Quark Parton Model, the lepton pair coming from the decaying boson has zero transverse-momentum, so there is no source that produces a transverse-momentum for the W's. Nevertheless the idea of parton probability distribution can be generalised to take into account an "intrinsic" transverse-momentum of the partons within the colliding hadrons. Such a distribution leads to a corresponding transverse-momentum of the lepton pair of the order of a typical hadronic mass-scale (few GeV).

The observation of an excess of events at large transverse-momentum was historically evidence for a new mechanism that generates large p_T. Leading-Order QCD explains these events via the two scattering processes: $q\bar{q} \to Wg$ and $qg \to Wq$ (see Figure 1.5). At large transverse-momentum ($p_T > 20$ GeV), the cross-section is dominated by the radiation of a single parton and perturbative QCD is expected to be reliable in this regime.

Not only the transverse-momentum distribution of the W-boson is altered in the high-p_T region, but also the rather simple lepton angular spectrum, expressed in Equation 1.6, is no longer accurate. The lepton angular distribution is modified for high-p_T events, and tends to the QPM prediction for $p_T^W \to 0$. In other words, the polarisation status of the W-boson is subject to a correction dependent on the transverse-momentum.

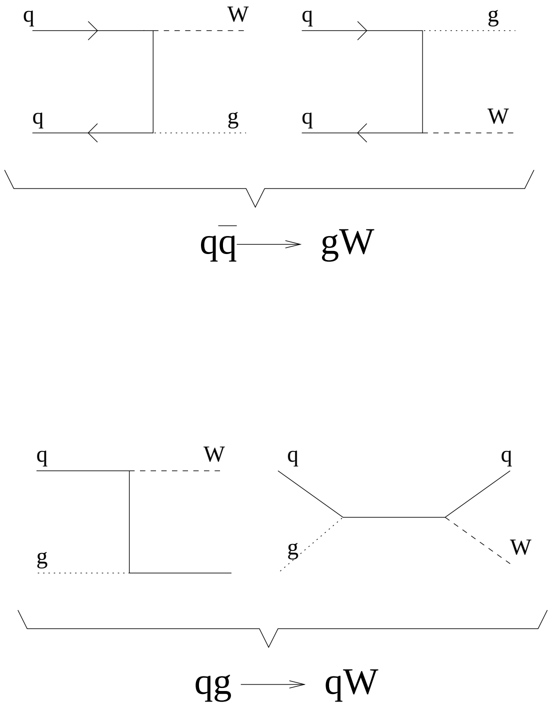

Figure 1.5: *The QCD-Leading Order processes that produce large-*p_T *events in W production. In the top diagrams a gluon is radiated from one of the scattering quarks. In the bottom diagrams a quark-gluon scattering produces a W, together with a quark.*

The general expression for the hadronic cross-section is given by:

$$\begin{aligned}\frac{\mathrm{d}\sigma^{h_1h_2}}{\mathrm{d}q_T^2\mathrm{d}y\mathrm{d}\Omega} &= \sum_{ab}\int \mathrm{d}x_1\mathrm{d}x_2 f_a^{h_1}(x_1,M^2)f_b^{h_2}(x_2,M^2)\times \\ &\quad \frac{s\mathrm{d}\tilde{\sigma}_{ab}}{\mathrm{d}t\mathrm{d}u\mathrm{d}\Omega}(x_1P_1,x_2P_2,\alpha_s(\mu^2)), \qquad (1.14)\end{aligned}$$

where s, t, u are the Mandelstam variables [17], the indices a, b indicate a quark, antiquark or gluon, and $f_a^h(x,M^2)$ is the parton distribution function for the parton a inside the hadron h. In Equation 1.14, $\mathrm{d}\Omega = \mathrm{d}\cos\theta\mathrm{d}\phi$, where θ and ϕ are the polar and azimuthal decay angles of the leptons in the gauge-boson rest-frame. The scale is explicitly set by M^2 here and $d\tilde{\sigma}_{ab}$ is the parton level cross-section for the process:

$$a(x_1P_1)+b(x_2P_2)\rightarrow W+X. \qquad (1.15)$$

The way the parton cross-section is most generally expressed is by the contraction of a lepton tensor $L_{\mu\nu}$ with the hadron tensor $H_{ab}^{\mu\nu}$. $L_{\mu\nu}$ acts as an analyser of the W polarisation. Nine independent helicity cross-sections ($\tilde{\sigma}_i$) are obtained from the decomposition of the hadron tensor. They correspond to linear combinations of the nine density matrix elements from three polarisation vectors for the gauge-boson. The result is the linear combination:

$$\frac{\mathrm{d}\sigma^{h_1h_2}}{\mathrm{d}q_T^2\mathrm{d}y\mathrm{d}\mathrm{cos}\theta\mathrm{d}\phi} = \sum_{i\in M} g_i(\theta,\phi)\frac{3}{16\pi}\frac{\mathrm{d}\tilde{\sigma}^i}{\mathrm{d}q_T^2\mathrm{d}y}, \qquad (1.16)$$

where $g_i(\theta,\phi)$ are angular coefficients and $M = \{U+L, L, T, A, I, P, 7, 8, 9\}$ is the set of nine helicity cross-sections. A detailed calculation is presented in [38]. For completeness, the cross-section using the explicit form of the coefficients is:

$$\begin{aligned}\frac{\mathrm{d}\sigma}{\mathrm{d}q_T^2\mathrm{d}y\mathrm{d}\cos\theta\mathrm{d}\phi} &= \frac{3}{16\pi}\frac{\mathrm{d}\sigma^{U+L}}{\mathrm{d}q_T^2\mathrm{d}y}[(1+\cos^2\theta)+ \\ &\quad +\frac{1}{2}A_0(1-3\cos^2\theta)+A_1\sin 2\theta\cos\phi+ \\ &\quad +\frac{1}{2}A_2\sin^2\theta\cos 2\phi+A_3\sin\theta\cos\phi+\end{aligned}$$

$$+A_4 \cos\theta + A_5 \sin^2\theta \sin 2\phi +$$
$$+A_6 \sin 2\theta \sin\phi + A_7 \sin\theta \sin\phi] \tag{1.17}$$

where σ^{U+L} is the total rate (production cross-section for unpolarised bosons), and the A_i are ratios of the helicity cross-sections to the total cross-section:

$$A_0 = \frac{2\mathrm{d}\sigma^L}{\mathrm{d}\sigma^{U+L}}, \quad A_1 = \frac{2\sqrt{2}\mathrm{d}\sigma^I}{\mathrm{d}\sigma^{U+L}}, \quad A_2 = \frac{4\mathrm{d}\sigma^T}{\mathrm{d}\sigma^{U+L}}, \quad A_3 = \frac{4\sqrt{2}\mathrm{d}\sigma^A}{\mathrm{d}\sigma^{U+L}},$$

$$A_4 = \frac{2\mathrm{d}\sigma^P}{\mathrm{d}\sigma^{U+L}}, \quad A_5 = \frac{2\mathrm{d}\sigma^7}{\mathrm{d}\sigma^{U+L}}, \quad A_6 = \frac{2\sqrt{2}\mathrm{d}\sigma^8}{\mathrm{d}\sigma^{U+L}}, \quad A_7 = \frac{4\sqrt{2}\mathrm{d}\sigma^9}{\mathrm{d}\sigma^{U+L}}. \tag{1.18}$$

The parameters α_1 and α_2:

Integrating Equation 1.17 over the azimuthal-angle ϕ leads to the simple expression:

$$\frac{\mathrm{d}\sigma}{\mathrm{d}q_T^2 \mathrm{d}y \mathrm{d}\cos\theta_{CS}} = C(1 + \alpha_1 \cos\theta_{CS} + \alpha_2 \cos^2\theta_{CS}), \tag{1.19}$$

where:

$$C = \frac{3}{8}\frac{\mathrm{d}\sigma^{U+L}}{\mathrm{d}q_T^2 \mathrm{d}y}[1 + \frac{A_0}{2}], \quad \alpha_1 = \frac{2A_4}{2 + A_0}, \quad \alpha_2 = \frac{2 - 3A_0}{2 + A_0}. \tag{1.20}$$

Notice that Equation 1.19 becomes the familiar angular dependence of Equation 1.3, the V−A angular dependence, for α_1=2 and α_2=1. The most recent QCD-NLO (Next-to-Leading Order) calculation for A_i is also reported in [38]. The calculation is done in the Collins-Soper frame. The Collins-Soper frame (see Figure 1.6) is a W rest-frame where the proton-antiproton pair lies in the *xz*-plane, with the *z*-axis chosen to bisect the angle between the proton and the negative antiproton direction. The proton and antiproton axes are seen to make an angle because of the transverse boost of the W-boson. The θ-angle of the lepton direction is measured with respect to the *z*-axis, whereas the ϕ-angle is measured with respect to the *xz*-plane.

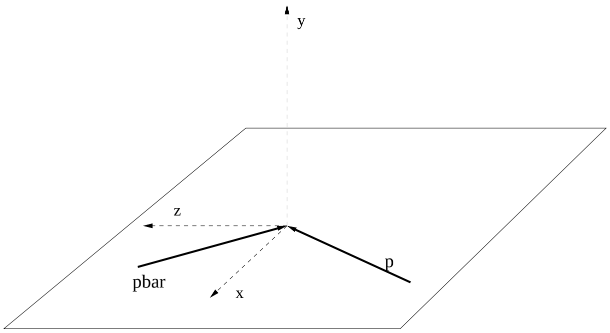

Figure 1.6: *A sketch of the Collins-Soper W rest-frame.*

Figure 1.7 shows the QCD expectation for α_2 versus the transverse-momentum of the boson. The limit $p_T^W \to 0$ is the QPM limit. Also shown is the theoretical prediction for α_1 up to 100 GeV. The lower-right plot is a 2D view of the angular distribution according to QCD. The $p_T^W = 0$ limit is the only one that gives zero cross-section for a certain configuration, when the W-boson is fully polarised and the lepton(antilepton) moves along(opposite) the W polarisation direction. The expectation is that α_2 decreases by 20%, and α_1 decreases by 75%, already at $p_T^W = 20$ GeV. Therefore it should be possible to observe such effect at the Tevatron Collider. The difference between Leading Order and Next-to-Leading Order is much smaller than the sensitivity given by the available proton-antiproton datasets.

1.6 The role of the lepton angular distribution in electroweak precision measurements

The full measurement of the lepton angular distribution is important because:

- it is a test of the Standard Model and was historically used to confirm the

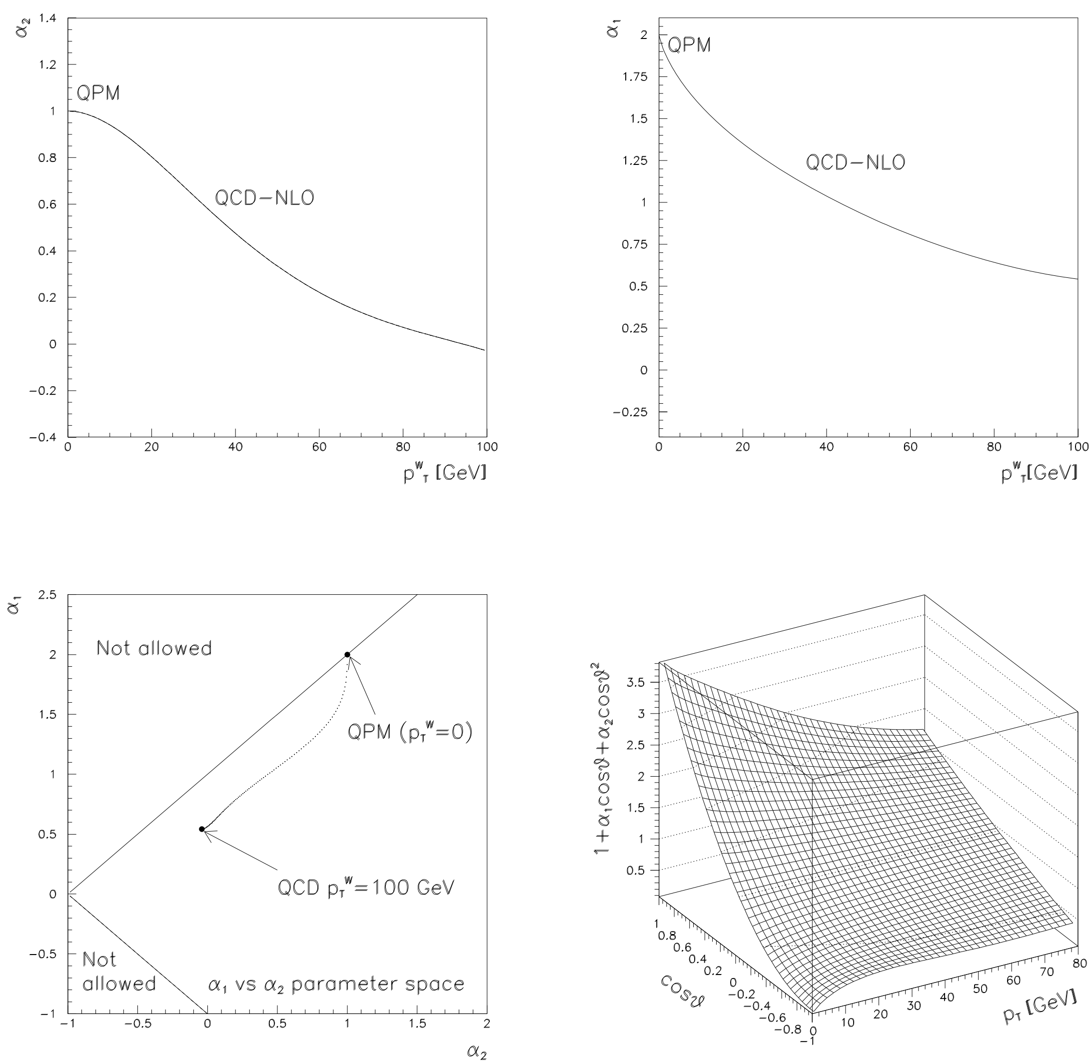

Figure 1.7: *Upper-left: theoretical NLO-QCD calculation of* α_2 *vs.* p_T^W*. The limit* $p_T^W \to 0$ *is the Quark Parton Model, for which* $\alpha_2 = 1$*. Upper-right: theoretical NLO-QCD calculation for* α_1 *vs.* p_T^W*. Lower-left: The* α_1 *vs.* α_2 *parameter space. The regions marked with "not-allowed" are where the cross-section, as expressed by Equation 1.19, would have zero or negative values. Lower-right: 2D view of the NLO-QCD angular distribution. The* $p_T^W = 0$ *limit is the only one that forbids one of the configurations, when the W-boson is fully polarised and the lepton(antilepton) moves along(opposite) the W polarisation direction.*

parity violating characteristics of the electroweak theory .

- at high transverse-momentum of the W-boson it provides a test of QCD. Moreover, the azimuthal angular distribution is potentially a handle to measure the gluon distribution function in the proton.

The first measurement of the lepton angular distribution, at $p_T^W < 15$ GeV, comes from the CERN proton-antiproton collision data collected between 1982 and 1985. The UA1 and UA2 collaborations measured the average value of $Q\cos\theta$, where Q is the lepton charge and θ is measured in the W rest-frame. The quantity $< Q\cos\theta >$ can be directly related to the spin J of the W-boson [35], so that:

$$\begin{aligned} < Q\cdot\cos\theta > &= (<\lambda><\mu>)/J(J+1) \qquad \text{if } J>0 \\ < Q\cdot\cos\theta > &= 0 \qquad\qquad\qquad\qquad\quad\; \text{if } J=0\ . \end{aligned} \tag{1.21}$$

The parameter λ measures the global helicity of the lepton-neutrino system (=+1) and μ measures the global helicity of the production system (=+1 only in the Quark Parton Model). For $J=1$ it follows that $< Q\cdot\cos\theta >= 0.5$; this can be compared with the measured value of 0.43±0.07 [5, 6], thus confirming the vector-boson nature of the W particles. The review of the results was well summarised in the statement [14]: "[...] the $W\to e\nu$ decay angular distribution was found to be consistent with the predictions of the V−A Standard Model".

The polar-angle distribution is an important component in other electroweak measurements. Two examples are given here.

The W charge asymmetry measurement:

The forward/backward asymmetry of W charge [18] is the fact that W^+'s follow preferentially the direction of protons, whereas W^-'s follow preferentially the antiproton direction. The W asymmetry is useful to constrain the parton density functions in the proton, as it measures the ratio of the pdf's u/d [20]. However, since the W rapidity is experimentally undetermined, the following *lepton* asymmetry is used instead:

$$A(y_l) = \frac{\mathrm{d}\sigma^+/\mathrm{d}y_l - \mathrm{d}\sigma^-/\mathrm{d}y_l}{\mathrm{d}\sigma^+/\mathrm{d}y_l + \mathrm{d}\sigma^-/\mathrm{d}y_l}. \tag{1.22}$$

$A(y_l)$ is effectively the convolution of the W charge asymmetry with the lepton decay asymmetry, therefore a reliable simulation and understanding of the lepton decay distribution is important and reduces the systematics of the measurement. Figure 1.8 shows the lepton charge asymmetry measurement at CDF [19]. The plot shows the W decay lepton asymmetry as a function of the rapidity. Positive leptons are preferentially found in the positive rapidity region as a result of the charge asymmetry in the W boost.

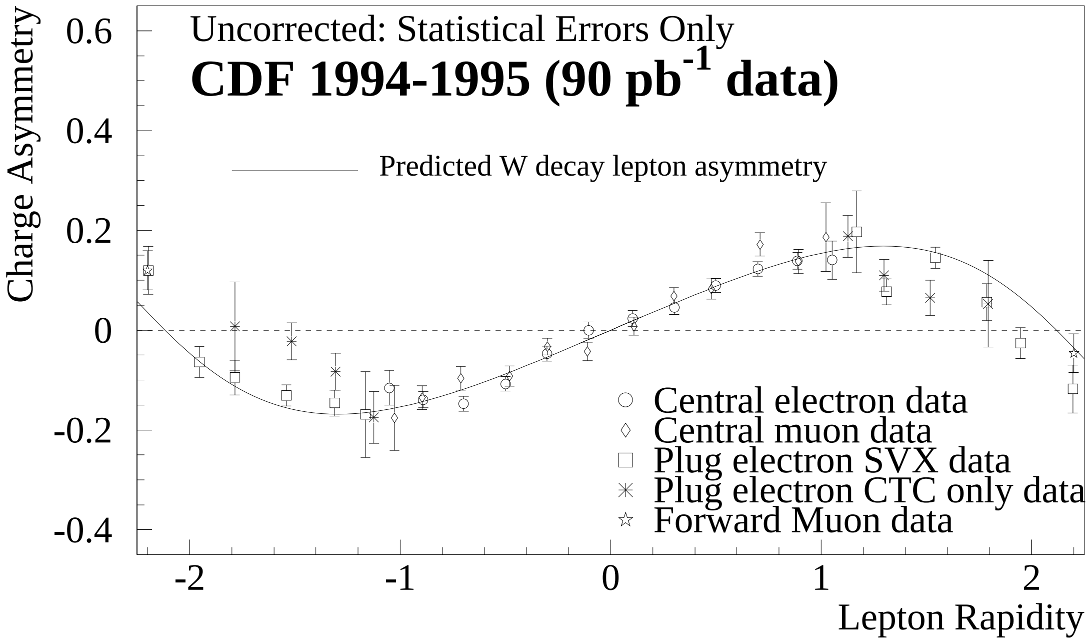

Figure 1.8: *The measurement of the lepton charge asymmetry at CDF.*

The W mass precision measurement:

The W mass precision measurement is another example where the lepton angular spectrum is particularly relevant. The search for the Higgs boson [23, 24, 25] has prompted increasing precision in the measurement of the W mass in order to predict the Standard Model Higgs mass. The W-boson mass at a hadron collider is measured using the Jacobian peak of the transverse-mass distribution. Technically the value is determined by fitting the transverse-mass distribution with a set of Monte Carlo templates, obtained by varying the input mass. The lepton angular distribution is relevant to the W mass measurement because the transverse-mass has a first order dependence on the square of the $\cos\theta$ distribution, and hence on α_2:

$$M_T = f(\cos^2\theta). \tag{1.23}$$

Therefore the simulation of the lepton angular spectrum affects the systematics of the W mass measurement. Figure 1.9 shows the typical transverse-mass distribution for the W mass analysis at CDF (from the data collected in 1992-1996, Run I) [21]. Figure 1.10 is an example of how the transverse-mass distribution is sensitive to a change in the lepton angular distribution parameter α_2 between 1.0 and 0.8. The study of the sensitivity of the transverse-mass on the lepton angular distribution is detailed in Chapter 4.

A quantitative estimate of the effects of α_2 on the measured value of the W-boson mass can be derived from Figure 1.11. The plot shows the contour lines of the likelihood function in a simultaneous α_2 and M_W fit at CDF. The orientation of the ellipse in the M_W vs. α_2 plane measures the correlation between the two parameters, here approximately 10 GeV/0.01. Since in the W mass measurement it is typically required p_T^W less than 20 GeV, and in the Standard Model the average value of α_2 in this range is approximately 0.95, the measured W-boson mass at the Tevatron would be shifted by 50 MeV if the p_T^W dependence of α_2 were not taken into account.

In the Run I W mass measurement at CDF, α_2 was set to the Standard Model theoretical expectation, with no associated systematic error. Although the results from the Run I phase of the Tevatron were dominated by statistical errors, the start of the new run in 2001 and the luminosity projection, make the case that statistics will become of comparable size to the systematic uncertainty, and therefore it will be crucial that all the major contributions to the systematic error are fully understood and minimised. This analysis will provide a direct measurement of α_2 and a systematic study of the dependence of the leptonic angular distribution parameters on the W-boson transverse mass distribution.

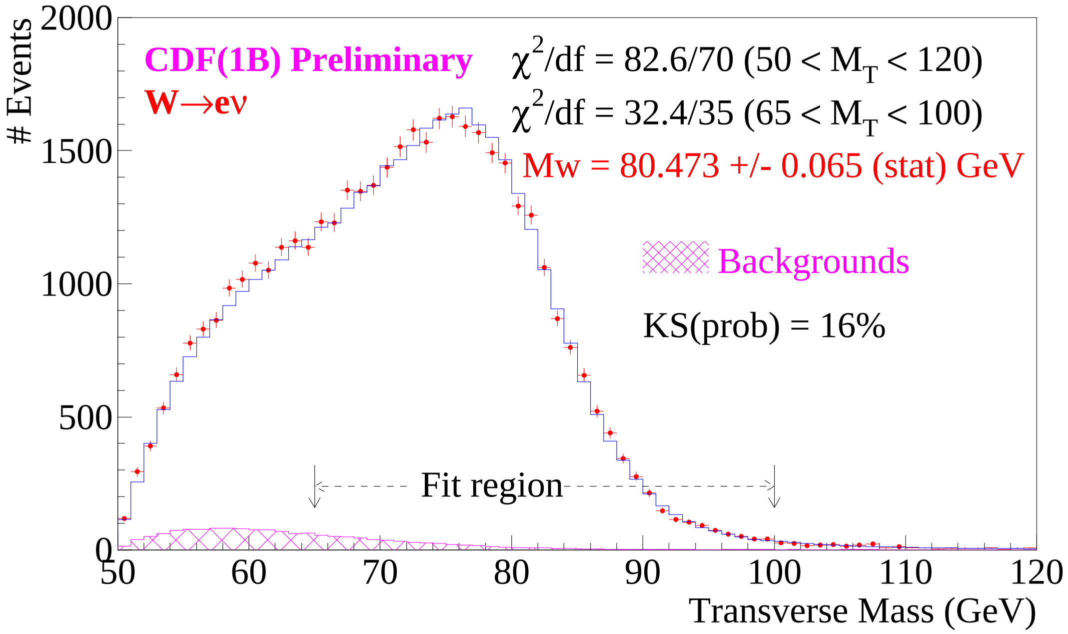

Figure 1.9: *The transverse-mass distribution used to obtain the W mass for CDF Run Ib.*

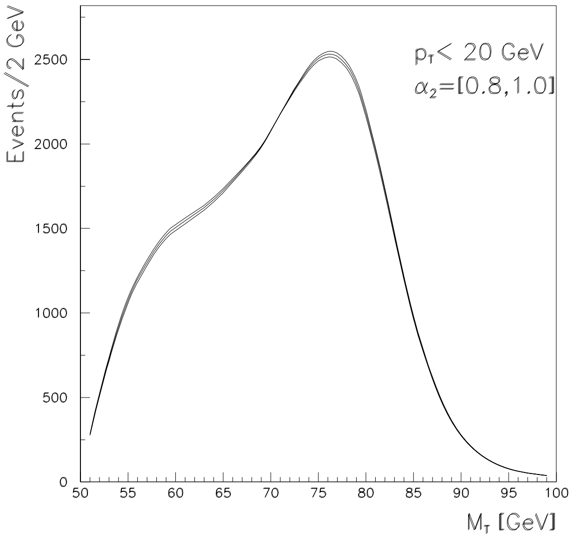

Figure 1.10: *The transverse-mass distribution, used in the W mass determination, is sensitive to the lepton angular distribution with a first order dependence on* α_2*. Here is an example of the sensitivity of the distribution to* α_2*. The lines show* α_2*=0.8, 0.9, 1.0.*

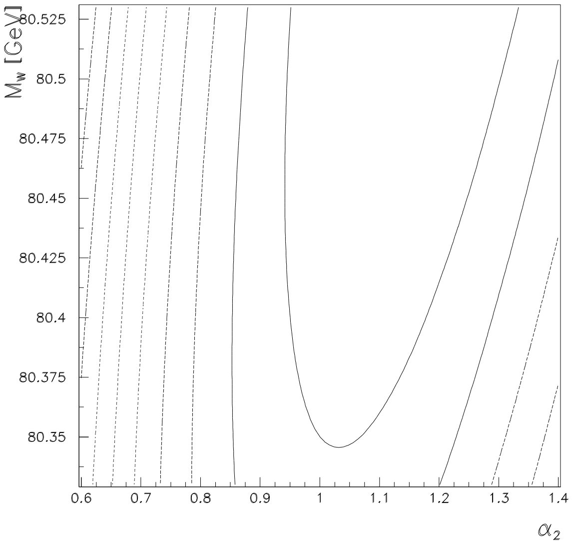

Figure 1.11: *Contour lines of the likelihood function in a simultaneous* α_2 *and* M_W *fit at CDF.*

Chapter 2

The CDF Experiment at the Tevatron Collider

The Collider Detector at Fermilab (CDF), is a general purpose experiment for the study of $p\bar{p}$ collisions at the Fermilab Tevatron Collider. The Tevatron is the highest-energy proton-antiproton accelerator in the world. The CDF detector was built in 1988, and has undergone several hardware upgrades between periods of data taking. This chapter describes the Tevatron and the CDF detector, emphasising the differences between the Run I configuration and the upgrades performed for the Run II phase, currently under commissioning. For a complete review see [42, 43].

2.1 The Tevatron

The Tevatron is a circular proton synchrotron 1 km in radius, located at the Fermi National Accelerator Laboratory, in the United States. It produces proton-antiproton collisions with a centre-of-mass energy of $\sqrt{s}$=2.0 TeV. The data presented in this thesis have been collected between 1994 and 1996 at $\sqrt{s}$=1.8 TeV. Figure 2.1 shows a schematic view of the Fermilab chain of accelerators.

The protons begin as H^- ions, produced from a bottle of hydrogen gas. The ions are accelerated through a 145 m linear accelerator (the Linac) to an energy of 400 MeV. At the end of the Linac, the electrons from the H^- ions are stripped off by copper foil, and the resulting protons are passed into the Booster ring. The Booster ring is a synchrotron that takes protons up to an energy of 8 GeV and also forms them into bunches. For the Tevatron Run I operations, the 8 GeV proton bunches were then injected into the 1 km radius Main Ring synchrotron, where they were accelerated to 150 GeV. Today the existing Main Ring has been replaced by a new accelerator, the Fermilab Main Injector, which provides a factor $\sim$2 increase in luminosity beyond that projected with the Main Ring alone, as well as providing a platform from which an additional increase in luminosity could be achieved. The 150 GeV proton bunches are finally injected into the evacuated beam pipe of the Tevatron ring and brought to an energy of 1000 GeV.

The production of the anti-protons begins with 120 GeV protons focused to a small spot-size on a nickel target. Antiprotons are produced over a large spread of angles centred on the forward direction, and with energies of approximately 8 GeV, and are collected and focused by a lithium lens. After being focused into the Antiproton Injection Line, they are injected into a Debuncher ring, which reduces the spread of energies through a process known as “stochastic cooling”. The antiprotons are then stored in the Accumulator ring to form a “stack”. When the stack is large enough, bunches of anti-protons are transferred into the

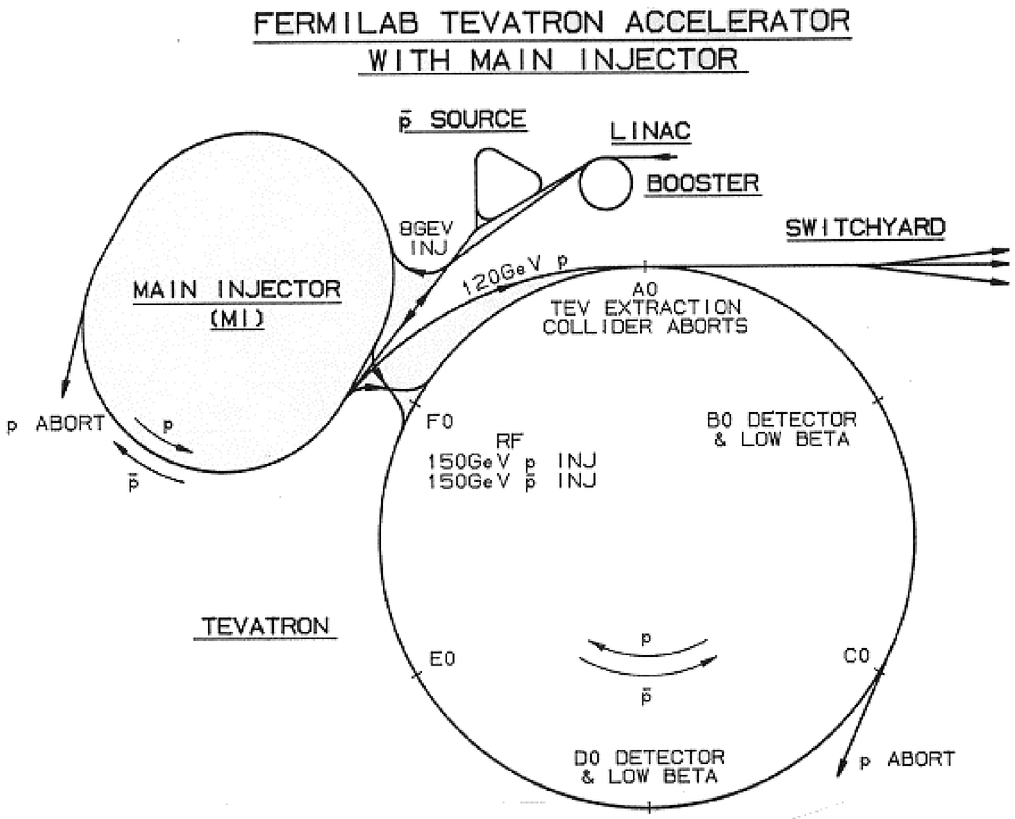

Figure 1-2. Schematic View of the Main Injector Connections to the Booster, Antiproton Source, Tevatron and Switchyard.

Figure 2.1: *A schematic view of the Tevatron accelerator system [44], with the new Main Injector which is part of the Run II upgrade, shown on the left. The CDF detector is located at the point labelled B0 on the Tevatron Ring.*

	Run Ib	Run II
Beam energy	900 GeV	1000 GeV
Proton bunches	6	36, 140
Antiproton bunches	6	36, 121
Bunch length (rms)	60 cm	37 cm
Bunch spacing	$\sim$ 3500 ns	396, 132 ns
Typical luminosity	1.6×10^{31} cm^{-2}s^{-1}	0.9×10^{32}, 1.6×10^{32} cm^{-2}s^{-1}
Data sets	90 pb^{-1}	$\sim$ 2 fb^{-1}

Table 2.1: *The Tevatron operational parameters. There are two operational modes for Run II, an initial phase with 36×36 bunches and a subsequent phase with 140×121 bunches.*

Tevatron ring and accelerated to 1000 GeV. As part of the Tevatron upgrade for Run II, a new Antiproton Recycle Ring has been installed in the old Main Injector enclosure. The role of the Recycler Ring is to provide more antiprotons for the Tevatron, which proportionally increases the luminosity. This is accomplished by acting as a post-Accumulator and receptacle for recycled antiprotons from previous Collider stores.

Table 2.1 summarises the operational parameters of the Tevatron: beam energy, number of bunches, luminosity etc. and compares the Run I values with those expected for Run II. The higher luminosity for Run II comes mainly from the increase in the number of bunches, reduced bunch spacing, and slightly higher proton and antiproton bunch intensities.

There are two instrumented collision points along the ring. One is labelled B0, where the CDF detector is located, and the other D0, for the D0 detector. Before the bunches of protons and anti-protons enter the collision points, they are focused by quadrupole magnets. The bunches continue to circle around the ring until the luminosity becomes too small, due to the increase in size of the beam as well as the reduction of protons and antiprotons bunches. A continuous period of collider operation (a "store") lasts typically 10 hours (7 for Run II). During Run Ib, the typical luminosity has been 1.6×10^{31} $\text{cm}^{-2}\text{s}^{-1}$ and the collected data set presented in this analysis is of 90 pb^{-1}. The goal for Run II is a typical luminosity of 1.6×10^{32} $\text{cm}^{-2}\text{s}^{-1}$ and a data set of $\sim$ 2 fb^{-1} within two years of operation.

2.2 The CDF Detector

2.2.1 Overview

The CDF detector is a solenoidal magnetic spectrometer with cylindrical symmetry surrounded by 4π calorimetry, designed to study a broad range of final states in $p\bar{p}$ collisions. The detector combines precision charged-particle tracking with fast projective calorimetry and fine-grained muon detection.

The detector is shown schematically in Figure 2.2 and in 3D in Figure 2.3. Tracking systems are contained in a superconducting solenoid, 1.5 m in radius and 4.8 m in length, which generates a 1.4 T magnetic field parallel to the beam axis. CDF uses a coordinate system where the polar-angle θ is measured from the proton direction, the azimuthal angle ϕ is measured around the beam direction, and the pseudo-rapidity is defined as $\eta = -\ln(\tan(\theta/2))$.

The high-luminosity Tevatron of Run II has required extensive changes to the experimental apparatus for CDF. In particular, the tracking system has been replaced with a new and more optimal combination of drift chamber and silicon vertex detector. The calorimetry is now exclusively scintillator-based, the electronics and trigger are fully compliant with the new pipelined configuration, and all the software has been re-written using C++ and an Object Oriented architecture. A sketch of the detector evolution from 1988 to 1999 is shown in Figure 2.4. The remaining part of this chapter describes the essentials of the Run Ib tracking systems, calorimetry, muon systems and triggers, as the analysis presented in this thesis only uses Run Ib data. However, the major upgrades to the detector systems will be mentioned frequently.

2.2.2 Tracking Systems

There are 3 primary tracking detectors in CDF I: a Silicon Vertex Detector (SVX′), a Vertex Time Projection Chamber (VTX) and the Central Tracking Chamber (CTC). For this analysis the CTC is used for the tracking and VTX and SVX are only used to provide vertex information. The CTC track is “beam constrained” to point at this vertex and this produces a significant improvement in the CTC resolution. A description of the CTC and its Run II replacement, the COT, are described in the next chapter.

Silicon Vertex Detector:
The silicon vertex detector [45] is a four-layer silicon microstrip detector that covers a region in radius from 2.86 to 7.87 cm. In the region $1.1 < |z| < 26.6$ cm, it provides $r - \phi$ measurements with 13 μm resolution. It is divided into two identical “barrels” which surround the beam-pipe on opposite sides of the z=0 plane. Each barrel consists of four radial layers of silicon strip detectors, and each layer is divided in azimuth into 30° wedges.

For Run II, the silicon detector system (Layer00 + SVX II + Intermediate Silicon Layers) [46] is completely new, and is made of an integrated system with stereo capabilities, stand-alone tracking capabilities, and high-η coverage.

Vertex Time Projection Chamber:

Figure 2.2: *One quarter of the CDF detector. The detector is symmetric about the interaction point. This is the configuration for Run Ib.*

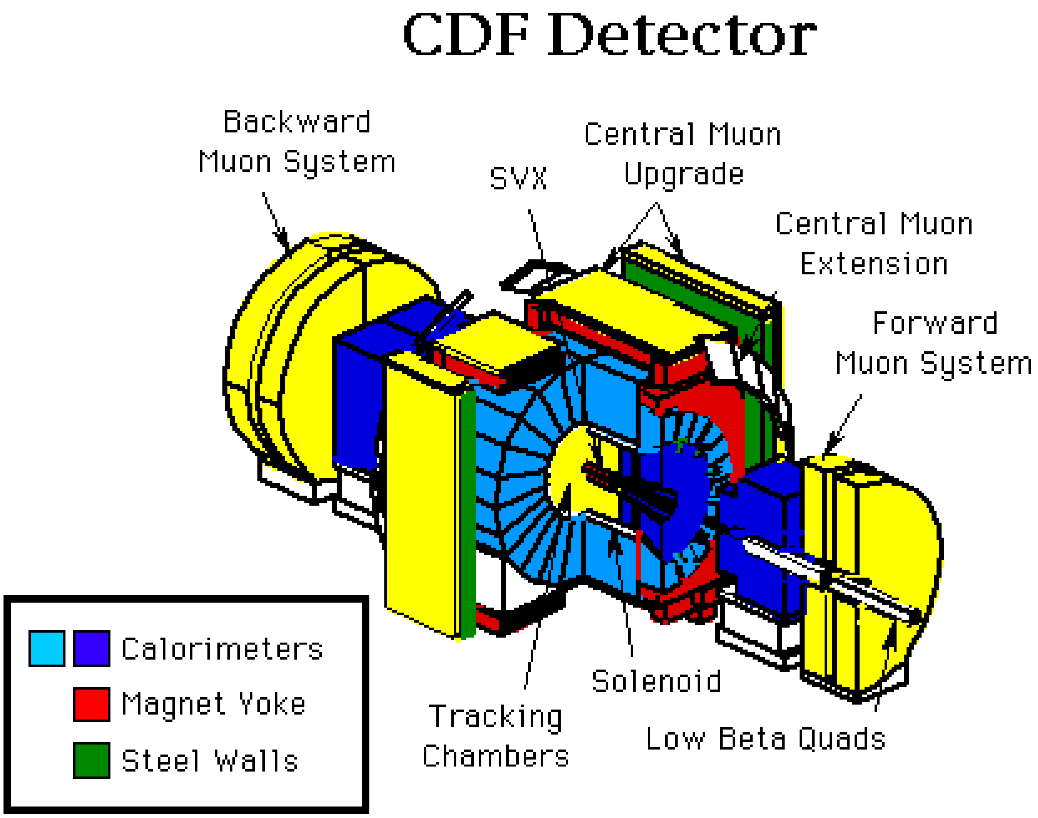

Figure 2.3: *A 3D schematics of the CDF Run I detector.*

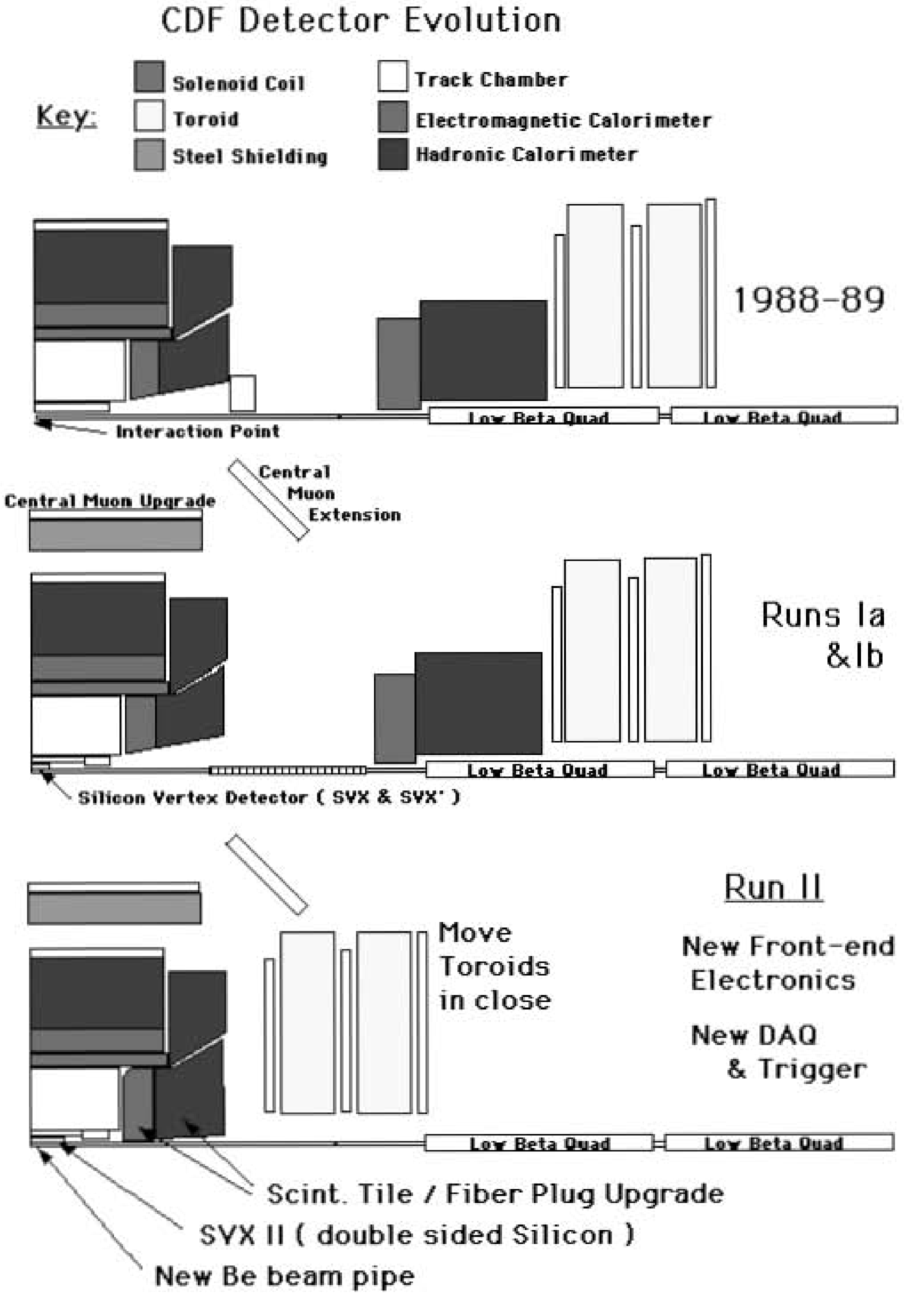

Figure 2.4: *The CDF detector evolution from Run 0 to Run II.*

The VTX is a set of 28 time projection chambers, each 9.4 cm in length, providing 24 z measurements ($\sigma \approx 200$ μm) between r=6.5 cm and r= 21 cm for 85< $|z|$ <132 cm and 16 z measurements between r= 11.5 cm and r= 21 cm for $|z| <$ 85 cm. Each module is segmented octagonally in ϕ; adjacent modules are offset 11.25° in ϕ to allow three-dimensional reconstruction of track segments that cross module boundaries.

The VTX is used in this analysis for finding the z position of the proton-antiproton interaction (the event vertex). The event vertex is necessary for event selection, lepton track reconstruction, and the calculation of the transverse component of calorimeter energies. The positions of z-vertices are used as seeds in the $r - z$ component of the CTC track reconstruction. A z-vertex measurement is also necessary for determining the beam-position in the $x - y$ plane, as the Tevatron beam-line has a significant slope (dx/dz and dy/dz). The transverse component of calorimeter energies, for each calorimeter cell i, is calculated as: $E_T^i = E_{total}^i \sin\theta_i$, where θ_i depends upon z_{vertex}.

2.2.3 Calorimetry

There are four different calorimeter systems at CDF, and these provide nearly contiguous coverage out to $|\eta| = 4.2$, seen from z=0. They are called "Central" (CEM, CHA), "Wall" (WHA), "Plug" (PEM, PHA) and "Forward" (FEM, FHA) (see Figure 2.2 for their location). Three of the four systems have both electromagnetic (EM) and hadronic (HA) calorimetry, and all the calorimeters are segmented into towers which point back to the nominal interaction point. All are used to measure missing transverse-energy, and the central electromagnetic calorimeter provides the energy measurement for the primary electron of $W \rightarrow e\nu$ events. They are all scintillator based, except the Plug Calorimeters,[1] which are

---

[1] For Run II, the Plug calorimeters have been replaced with scintillator based calorimeters.

a sandwich of proportional tubes arrays with lead (PEM) or steel (PHA).

CDF has also several regions of low calorimeter response ("cracks"), through which energetic particles can escape undetected: the $\theta = 90^\circ$ region between the east and the west halves of the CEM; the azimuthal boundaries between CEM wedges; the $\theta \sim 30^\circ$ region between the CEM and PEM, and the $\theta \sim 10^\circ$ region between the PEM and the FEM. Fortunately, all but the 10° region are well covered by the CTC, which can identify escaping charged particles in the crack regions.

Central Electromagnetic Calorimeter (CEM):

The central electromagnetic calorimeter [47] provides electron and photon energy measurements in the region $|\eta| < 1.1$ with a resolution:

$$\frac{\sigma_E}{E} = \frac{13.5\%}{\sqrt{E_T}} \oplus 1.5\% \ . \tag{2.1}$$

The first term is called "stochastic" and it is due to the shower fluctuations and PMT photoelectron fluctuations [48, 49]. The second term is called "constant" and it is due to the limited amount of data available for calibration.

The CEM is 18 radiation lengths thick and is physically separated into two halves, one covering $\eta > 0$ (east) and one covering $\eta < 0$ (west). Both halves are divided in azimuth into 24 wedges that subtend 15° each. Each wedge extends along the z-axis for 246 cm and is divided into 10 projective towers of approximately 0.1 units in η (see Figure 2.5 (left)). The active volume of the east and west halves begins at $|z| \approx 4$ cm. The two halves are pushed against each other at z=0, but a dead region remains between them of approximately $\Delta z = 8$ cm. The CEM has a radial thickness of 32 cm and consists of 31 layers of plastic scintillator interleaved with 30 layers of lead sheets. The scintillators are cut into projective towers which are viewed on both sides in azimuth by wave-length shifter sheets. The light is then collected by light guides and converted to electrical signals by

Figure 2.5: *Left: A central calorimeter wedge. The local coordinate system, in which x points azimuthally, is illustrated. The region between the lead/scintillator sandwich and the phototubes is where the CHA resides. Right: The structure of the CES chamber.*

At a depth of 5.9 X_0 (including the solenoid), which is approximately the depth at which shower energy deposition peaks, the central strip chamber (CES) measures the transverse shower shape with 1.4−2 cm segmentation, to be compared with the approximately 25 cm × 50 cm tower segmentation. A sketch of the CES is shown in Figure 2.5. The CES module in each wedge is a multi-wire proportional chamber with 64 anode wires oriented parallel to the beam axis, spaced 0.73 cm apart. The cathodes are segmented into 128 strips and an electron and photon shower typically spans several CES channels in each dimension. When CTC tracks from W-electrons are extrapolated to the CES ($r \approx 184$ cm), the CES and CTC shower positions match to 0.22 cm (rms) in azimuth and 0.46 cm (rms) in z. Both CES/CTC position matching and the CES shower shape are useful electron identification variables and are mentioned later in the analysis.

2.2.4 Muon Systems

CDF uses four systems of scintillators and proportional chambers in the detection of muons over the region $|\eta| < 2.0$. The absorbers for these systems are the calorimeter steel, the magnet return yoke, additional steel walls and the forward muon toroids. Four-layer drift chambers, embedded in the wedge directly outside (in radius) of the CHA, form the central muon detection system (CMU) [50, 51]. The CMU covers the region $|\eta| < 0.6$. Outside of these systems there is an additional absorber of 0.6 m of steel followed by a system of four-layer drift chambers (CMP) [52]. Approximately 84% of the solid angle for $|\eta| < 0.6$ is covered by CMU, 63% by CMP, and 53% by both. Additional four-layer muon chambers (CMX) with partial (70%) azimuthal coverage subtends $0.6 < |\eta| < 1$. Figure 2.6 shows the $\eta - \phi$ coverage of the muon system. For Run II, new chambers have been added to the CMP and CMX systems to close gaps in the azimuthal coverage.

In this analysis, muons from W decays are required to produce a track (called a “stub”) in the CMU or CMX that matches a track in the CTC. The CMP is used in this measurement only in Level 1 and Level 2 triggers.

2.3 Trigger and Data Acquisition

The CDF trigger is a three-level system that selects events for recording to magnetic tape. The crossing rate of proton and antiproton bunches in the Tevatron is 286 kHz, with a mean interaction rate of 1.7 interactions per crossing at a

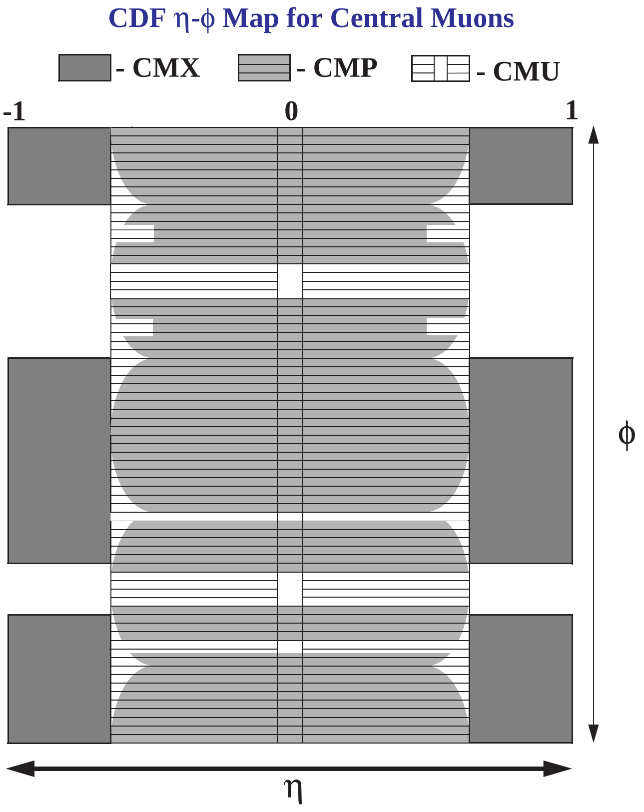

Figure 2.6: *The $\eta - \phi$ coverage of the muon systems in Run Ib.*

luminosity of ~1×10^{31} cm^{-2}s^{-1}. The first two levels of the trigger [53] consist of dedicated electronics with data paths separate from the data acquisition system. The third level [54], which is initiated after the event information is digitised and stored, uses a farm of commercial computers to reconstruct events. The triggers selecting $W \rightarrow e\nu$ and $W \rightarrow \mu\nu$ events are described below.

At Level 1, electrons were selected by the presence of an electromagnetic trigger-tower with E_T above 8 GeV (one trigger tower is two physical towers, which are adjacent in pseudorapidity). Muons were selected by the presence of a track stub in the CMU or CMX, and, where there is coverage, also in the CMP.

At Level 2, electrons from W decays could satisfy one of several triggers. Some required a track to be found in the $r-\phi$ plane by a fast hardware processor [55] and matched to a calorimeter cluster; the most important required an electromagnetic cluster with E_T above 16 GeV and a track with p_T above 12 GeV. This was complemented by a trigger which required an electromagnetic cluster with E_T above 16 GeV matched with energy in the CES [56] and net missing transverse-energy in the overall calorimeter of at least 20 GeV, with no track requirements. The muon Level 2 trigger required a track of at least 12 GeV that matches to a CMX stub (CMX triggers), both CMU and CMP stubs (CMUP triggers), or a CMU stub but no CMP stub (CMNP triggers). Due to bandwidth limitations, only about 43% of the CMX triggers and about 39% of the CMNP triggers were recorded.

At Level 3, reconstruction programs included three-dimensional track reconstruction. The muon triggers required a track with p_T above 18 GeV, matched with a muon stub. There were three relevant electron triggers. The first required an electromagnetic cluster with E_T above 18 GeV matched to a track with p_T above 13 GeV. It included also requirements on track and shower maximum matching, little hadronic energy behind the cluster, and transverse profile in z in both the towers and the CES. Because such requirements may create subtle biases, the second trigger required only a cluster above 22 GeV with a track above 13 GeV as well as 22 GeV net missing transverse-energy in the overall calorimeter. The third trigger required an isolated 25 GeV cluster with no track requirement and with 25 GeV missing transverse-energy.

Events that passed the Level 3 triggers were sorted and recorded. The integrated luminosity of the data sample in Run Ib was ~ 80 pb^{-1} in the muon sample and ~ 84 pb^{-1} in the electron sample.

Chapter 3

Studies of Internal Alignment for the Central Outer Tracker of the CDF Run II Detector

This chapter describes in detail the main tracker of the CDF Run II detector. The configuration and the drift properties are discussed in the first two sections. The third section gives a review of the internal alignment in Run I, and the implementation of the alignment code in Run II. The fourth and fifth sections show a study of the track-fit residuals in the context of the internal alignment of the COT.

3.1 The Central Outer Tracker for CDF Run II

The Central Outer Tracker (COT) [26] is an open-cell drift chamber designed to replace, in the region $|\eta| \leq 1.0$, the Central Tracking Chamber (CTC) used at CDF in Run 0 and Run I. The CTC would suffer from severe occupancy problems at luminosities $\mathcal{L} \geq 1 \times 10^{32}$ cm^{-2}s^{-1} typical of Run II. The design goal of the COT was to reproduce the functionality of the CTC, but using smaller drift-cells and a fast gas to limit drift-times to less than 100 ns (compared with 706 ns for the CTC). This requirement implies a maximum drift-distance of ~ 1 cm, about 1/4 that of the CTC. The COT has therefore about 4 times the number of cells, with a total of 2,520 drift-cells and 30,240 readout channels for the entire detector. The smaller drift-length also allows a smaller cell tilt-angle. With an electric field of approximately 2.5 kV/cm (compared with 1.3 kV/cm in the CTC), the Lorentz angle for the COT is 35° (compared with 45° in the CTC).

The basic drift-cell has a line of 12 sense-wires [30] alternating with shaper-wires every 3.8 mm, running between two gold-on-mylar cathode planes which are separated by ~ 2 cm (see Figure 3.1). The wires and cathode planes are strung between the slots on the two precision-milled end-plates. Stereo cells are strung using an offset between slots on opposing end-plates. The complete chamber is roughly 1.3% of a radiation length at normal incidence.

The cells in the COT are grouped in 8 super-layers (SL), covering a radial span between 44 cm and 132 cm. A super-layer is the set of all cells located at the same radius in the chamber. A layer is the set of all wires located at the same radius. Since the COT has 8 super-layers, and a cell has 12 sense-wires, the total number of layers is 96. A drawing of the arrangement of the cells in the COT is shown in Figure 3.2. The deficiency in CTC stereo reconstruction, caused by the small number of stereo measurements (24 out of the 84 total), is removed by increasing the number of stereo measurements to 48 out of the total of 96

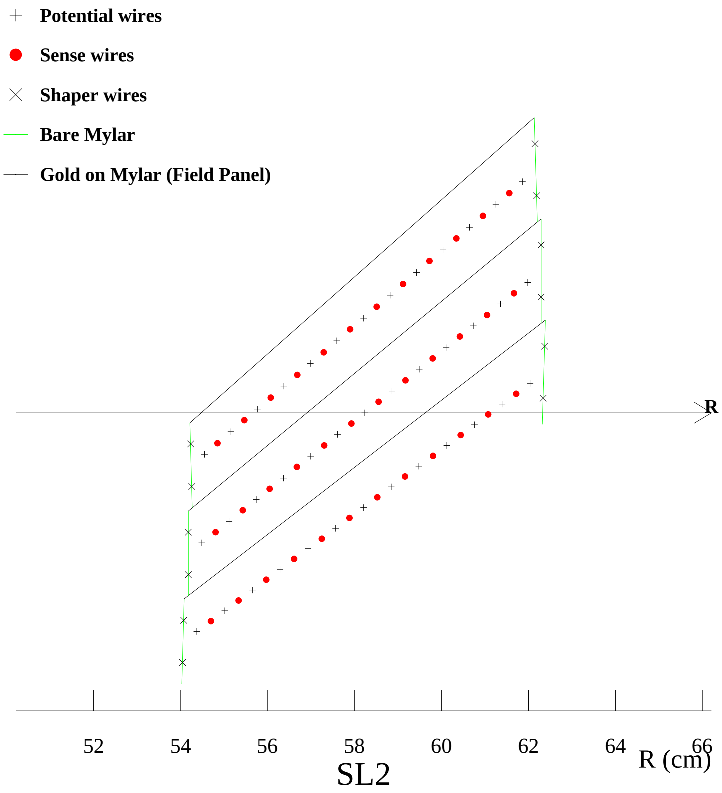

Figure 3.1: *Details of cells in super-layer 2 of the COT.*

measurements. Starting from the inner SL, the COT has alternating stereo and axial super-layers. Table 3.1 summarises the COT configuration.

3.2 A review of the physics in the CTC and COT

The ionisation mechanism:

A charged particle traversing the COT ionises [27, 28] the detector gas, leaving localised clusters of several electrons along its track. The ionisation electrons created along the particle's track drift toward the wires. Since their drift-velocity

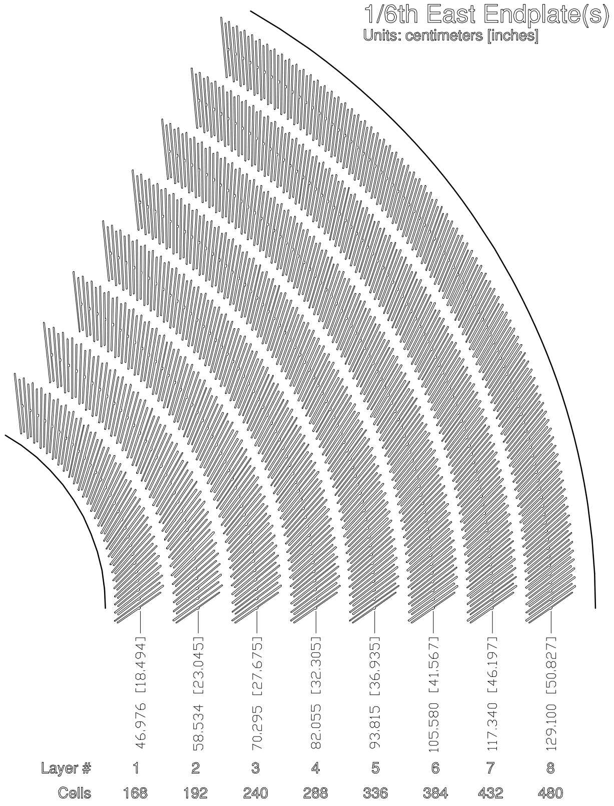

Figure 3.2: *The arrangements of cells in super-layers in the COT.*

is perpendicular to the magnetic field, they are deflected, i.e. the electron drift-direction is different from the electric field direction. The angle between drift-velocity vector and electric field vector is called the Lorentz angle. The nominal drift-fields in the COT are 1.8 kV/cm for the Ar/Ethane 50/50 mixture and 2.5 kV/cm for the Ar/Ethane/CF_4 50/35/15 gas mixture which gives the desired Lorentz angle of 35 degrees.

Close to the wire, the electrons gain enough energy to cause ionisation of the gas atoms themselves, which results in the development of an avalanche. Typically the first multiplication happens at a distance of about one wire diameter from the surface (20 μm for the COT). However, since the avalanche is an exponential process, the centre of gravity of the ion cloud is very close to the wire ($2-3$ μm).

Radial coverage:	44−132 cm for $\lvert\eta\rvert \le 1$
Operational:	• maximum drift-time 100 ns
	• E field 2.5 kV/cm, cell tilt 35°
	• luminosity $\geq 1 \times 10^{32}$ cm^{-2} s^{-1}
Configuration:	• 4 Axial+4 Stereo SL
	• 12 sense-wires per cell
	• 30,240 channels

Table 3.1: *A summary table of the COT parameters.*

The COT operates at a gas gain of 2×10^4, meaning that a single electron arriving at the wire creates on average 20,000 electrons. Finally the movement of the positively-charged avalanche-ions away from the wire induces a current signal which is sensed by the front-end electronics.

The movements of both the electrons and ions induce the signal on the wire. If a charged particle passes through the centre of a parallel-plate geometry, the electrons moving to the anode plane and the ions moving to the cathode plane induce each half of the signal. However, in a wire chamber the avalanche electrons are created very close to the wire, so the movement of the electrons induces only a small portion of the total signal (a few percent) while the movement of the ions away from the wire to the anode plane (field sheet) is responsible for the largest part of the signal charge. The avalanche electrons move at very high speed for a very short time, so their movement induces a short current spike. The induced charge during the first 20 ns is about 7% of the total. The ions induce a current until they reach the field sheets, which takes about 200 μs.

Thresholds vs. distance from the wire:

After the signal is amplified and filtered, it is discriminated in order to obtain a logic-pulse that can be measured by the TDC (Time to Digital Converter). The turn-on time of the discriminator depends on the discriminator threshold. A low discriminator threshold is crucial for a good position measurement. The lower limit of the threshold is determined by the noise level, hence good resolution requires the noise to be as low as possible. Various effects enter the threshold crossing time:

- For tracks passing at a distance from the wire less than $1-2$ mm, the distribution of crossing-time is very non-Gaussian with a long tail, because the signal is built up from electrons with very different path lengths. Moreover, the time-distance relation, i.e. the peak position of the threshold crossing-time distribution versus the distance of the track from the wire, is non-linear since the electric field increases rapidly. The drift-direction follows typically radial paths toward the wire.
- For a track far from the wire, the electrons are drifting perpendicular to the particle-track and it is very probable that the required number of electrons arrive all within a short time. The time-distance relationship is linear from 0.2 to 0.8 cm, since the drift-field is constant.
- For a drift-distance greater than 0.8 cm, the threshold-crossing is shifted to later times than the ones from linear relation, due to two effects: the first electrons arriving at the wire are no longer from a track segment that is along the perpendicular from the wire, so the drift-distance is greater than the perpendicular distance. The second reason is that the signals are smaller since there is less charge arriving at the wire, which means that the signal takes longer to cross the threshold.

Calibration corrections:

Effects like the threshold-crossing time versus the distance from the wire have to be accounted for in the drift-model [29]. These and other divergences from linearity are part of the calibration procedure. In the following are listed the typical corrections in the COT.

The *aspect-angle* correction takes into account the fact that tracks may traverse the cell making an angle with respect to a radial line. For radial tracks, i.e. infinite momentum tracks coming from the centre of the chamber, the drift-velocity is perpendicular to the track, by construction. When the drift is not perpendicular to the track, the drift-distance should be corrected by:

$$\Delta D = \rho \left(1 - \frac{1}{\cos\alpha} \right), \tag{3.1}$$

where α is the aspect-angle (see Figure 3.3), and ρ is the distance from the wire where the drift becomes radial. In the drift-model of the CTC, used for Run I, Equation 3.1 is empirically represented by [40]:

$$\Delta D = \rho \frac{\sin^2\alpha}{\sin^2\alpha - 1.238}, \tag{3.2}$$

and called the *quadratic aspect-angle* correction.

The so called β *correction* is due to the difference between the nominal drift-direction and the actual drift. The angle between these two directions is β, typically less than 0.5°. The drift-distance is altered by:

$$d' = \frac{d}{\sin\beta\tan\alpha + \cos\beta}, \tag{3.3}$$

where α is the aspect-angle of the track.

Since close to the wires the drift-speed increases, a *near-wire* correction to the drift-distance is also normally required. During Run I, this was corrected by adjusting the drift-times shorter than 200 ns. Such an approach has the advantage of not requiring the knowledge of the track-parameters. In Run II, the correction uses the estimated drift-distance from the wire, and is made after the track-fit.

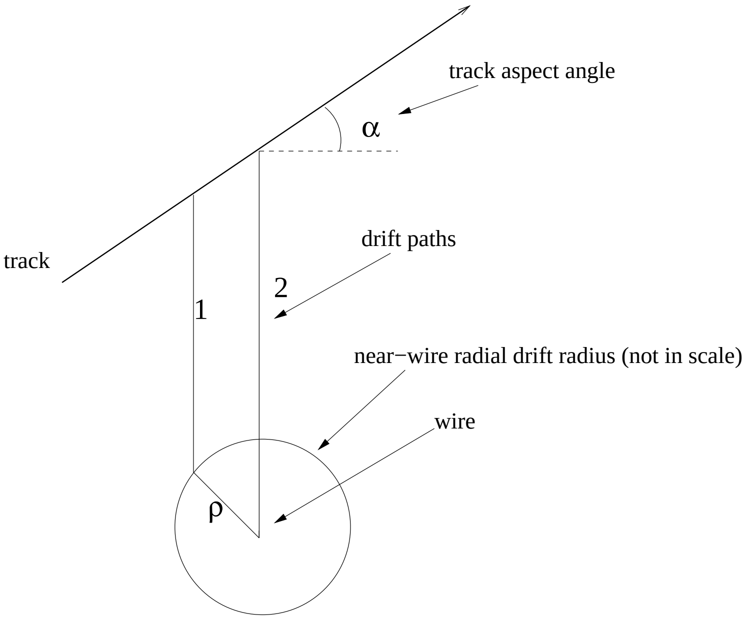

Figure 3.3: *Sketch of the drift-model showing the drift-paths, the near-wire radial drift and the aspect-angle of a track with respect to the radial direction. The drift is shown perpendicular to a radial track.*

The track-fit in the CTC and COT:

The track-fit is the process that starts with a set of hits in the detector, identified as belonging to a track by the pattern-recognition code, and fits them with a helix, using all the available information of the tracking chamber. The trajectory of a charged particle in a uniform magnetic field $\vec{B}$ is a helix, of which the projection onto the $r - \phi$ plane (perpendicular to $\vec{B}$) is a circle with radius:

$$R = p_T/q \cdot B, \tag{3.4}$$

where q is the electric charge and p_T is the momentum of the particle in the $r - \phi$ plane. The helix is parametrised by five numbers: curvature c (inverse radius of the circle in $r-\phi$); impact parameter d_0 (distance of closest approach to $r=0$); ϕ_0 (azimuthal direction at the point of closest approach to $r=0$); z_0 (the z position at the point of closest approach to $r=0$); and $\cot\theta$, where θ is the polar-angle.

The fit in CTC and COT is done using a χ^2 minimisation technique [32], searching for the parameters $\vec{p}$ such that:

$$\vec{\nabla}_{\vec{p}}\chi^2 = 0, \tag{3.5}$$

where $\vec{p}$ are the set of track parameters. The χ^2 is defined as:

$$\chi^2 = \sum_{hits} \frac{(\tilde{D}_h(\vec{p}) - D_h)^2}{\sigma_h^2}, \tag{3.6}$$

where $\tilde{D}_h(\vec{p})$ is the predicted drift-distance, D_h is the measured drift-distance, and σ_h is the resolution of D_h. The predicted drift-distance is evaluated by using the drift-direction, the sense-wires position and the parameters of the track. The measured drift-distance is obtained by combining the measured drift-time and the drift-properties. The expected drift-distance is the distance of the fitted track from the wire, along the drift-velocity direction. The equations are of the form:

$$\left\{ \begin{array}{l} D_h = (t - t_0)\cdot|\vec{v}| \\ \tilde{D}(\vec{p}) = (\vec{r}(\vec{p}) - \vec{r}_w)\cdot\hat{v} \end{array} \right. , \tag{3.7}$$

where $\hat{v}$ is an unit-vector along the drift-direction ($\vec{v}$), $\vec{r}_w$ and $\vec{r}(\vec{p})$ are the position of the wire and that of the hit respectively. Often the short-comings of the linear drift model are treated by adjusting t_0. The correction can use both the measured properties of the hit (the turn-on time and the time-over-threshold) and, when this information is available, the track-parameters.

3.3 Internal alignment in Run I

The internal alignment is an off-line procedure in place to insure that the tracking software computes unbiased track-parameters, with the best hit resolution. The precise knowledge of the geometry of the chamber is a crucial aspect. If, for instance, a small mechanical twist has not been accounted for in the track-reconstruction, the measured helix will have a biased curvature. In addition, random wire misplacements can affect the hit resolution, and ultimately the momentum resolution of the chamber, worsening the performance. Normally this is a smaller problem, as calibration dominates the resolution.

During the early stage of Run I, tracking bias was dealt with by correcting helix parameters. The W mass analysis working group observed that the beam-constrained curvature of tracks needed to be corrected by the following terms:

$$\frac{q}{p_T} \rightarrow \frac{q}{p_T} - 0.000056 - 0.00040 \cdot \sin(\phi_0 - 3.0) - 0.00028 \left(\cot\theta + \frac{z_0}{81 \text{ cm}}\right), \quad (3.8)$$

where q is the particle's charge. Physically the constant term, the $\cot\theta$ and the z_0 dependent terms, correspond to separate distortions of the east and west end-plates. The ϕ-dependent term may correspond to a displacement of the SVX, and hence the SVX-derived beam-line, with respect to the CTC axis. The $\cot\theta$ of the track also needed a correction factor:

$$\cot\theta \rightarrow 0.9986 \cdot \cot\theta. \quad (3.9)$$

At the end of Run Ib, an internal alignment procedure was developed to eliminate most of these corrections [41]. The procedure is the following: three of the five helix parameters of a track are constrained with external informations. z_0 is determined with the vertex z position measured with the VTX. The impact parameter (d_0) is constraint to the beam-line, measured with the SVX, and the curvature is measured with the calorimeter energy (a sample of electron tracks from $W \to e\nu$ is used for the alignment). The residuals of the track-fit are minimised by fitting to a set of wire-position offsets (WPO's). The model for the WPO's is to rotate each layer by:

$$\Delta\phi_i = A_i + B_i z \ , \tag{3.10}$$

where i is the layer's index, A, B are the WPO's constants determined from the fit and z is the longitudinal position. This represents a coherent (i.e. ϕ independent) twist of each end-plate and a rotation of the rings of position holes for each layer of sense-wires. The linear slope in z of the ϕ offsets allows for the different deformations in the east and west end-plates. Figure 3.4 shows the WPO offsets evaluated at the end-plates ($z = \pm$ 150 cm) [34].

The displacements that vary rapidly at inner and outer layers of some super-layers[1], are believed to be caused by the small correlation between alignment and calibration, i.e some drift-model effects can be absorbed by the alignment constants. A false curvature can be seen here as a difference of about 0.2 mrad from inside to outside in the east end-plate alignment. A much smaller effect can be seen in the west end-plate.

The WPO correction in the CTC tracking code was included by adjusting the drift-distance, and not by modifying the geometry itself in the reconstruction code. The first step for Run II has been to implement the same type of correction as in Equation 3.10, but by changing the geometry of the tracking chamber in the reconstruction code. The position of a wire is altered by rotating the wire-ends according to Equation 3.10. The sag of the wires is also taken into account by allowing for a quadratic term in the equation that describes the wire. A wire is

---

[1] In the CTC there are 9 super-layers, 5 axial and 4 stereo. Axial and stereo SL's have 12 and 6 layers respectively, so the total number of layers is 84.

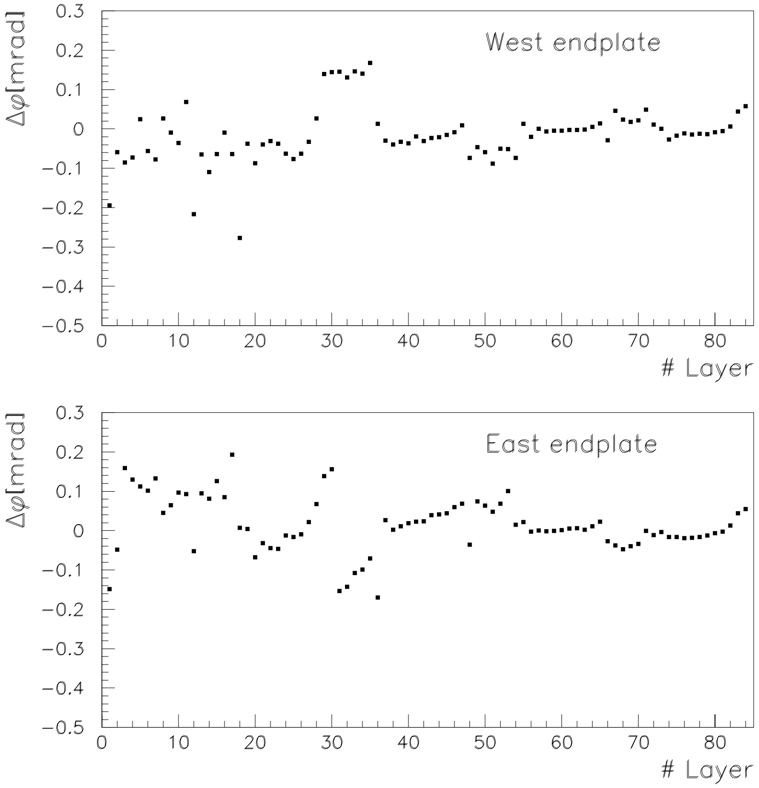

Figure 3.4: *Run Ib ϕ-offsets vs. CTC layer number at the end-plates.*

described by a parabola:

$$\begin{pmatrix} x \\ y \end{pmatrix}(z) = \begin{pmatrix} x_0 \\ y_0 \end{pmatrix} + \begin{pmatrix} a_x \\ a_y \end{pmatrix} z^2 + \begin{pmatrix} b_x \\ b_y \end{pmatrix} z. \qquad (3.11)$$

Gravity only affects y and leads to $a_y > 0$. In principle electrostatic distortions [31] can be accommodated by $a_x \neq 0$. In the COT there is a support that runs across the wire-plane at z=0. Therefore a, b are different for $z > 0$, $z < 0$ for COT. In the yz-plane, the coefficients are taken as the estimated sense-wire sag[2]

---

[2] The sense-wires sag by 230 μm for the CTC and 180 μm for the COT.

(s). The equation of a wire in the $y - z$ plane is:

$$y = (y_0' - s) + \left(\frac{s}{z_{end}^2}\right) z^2 + b_y z. \tag{3.12}$$

b is determined by the stereo angle and by the relative-rotation at the end-plates. Figure 3.5 shows the effect of the alignment corrections on high-energy muon tracks recorded in Run I. Plotted is the difference $\Delta(1/p_T)$, in percentage, between the tracks fitted *with* and *without* alignment correction. The Run II fitter has been used here to re-process a sample of Run I data, with the new alignment code. The mean value for positive tracks, is shifted by $+0.22 \pm 0.05$ %, whereas for negative tracks is shifted by -0.27 ± 0.05 %. The charge-dependent shift is typical of internal misalignments. The uncorrected wire-position misalignments are therefore responsible for generating a “false curvature” of about 0.2% for muons coming from the Z.

Despite the efforts to correct for internal alignment during the track reconstruction stage, in Run I data there was a known disagreement of the energy-scale determined from the Z mass (using $Z \to ee$ events), with that determined by E/p distributions [33]. This suggested a problem of systematics between the tracking for muons and that for electrons, or a systematic difference between the actual tracking and the tracking simulation. Ideally, the E/p distribution would be used to transfer the energy-scale from the tracker to the E_{cal}, where the momentum-scale is determined by the J/ψ and $\Upsilon \to \mu\mu$ data, because of the smaller statistical uncertainty. The strategy for Run II has been to use the best knowledge of the geometry of the tracking chamber from the beginning. Therefore the COT has been accurately surveyed and the measurements put into the geometry description used by the reconstruction code.

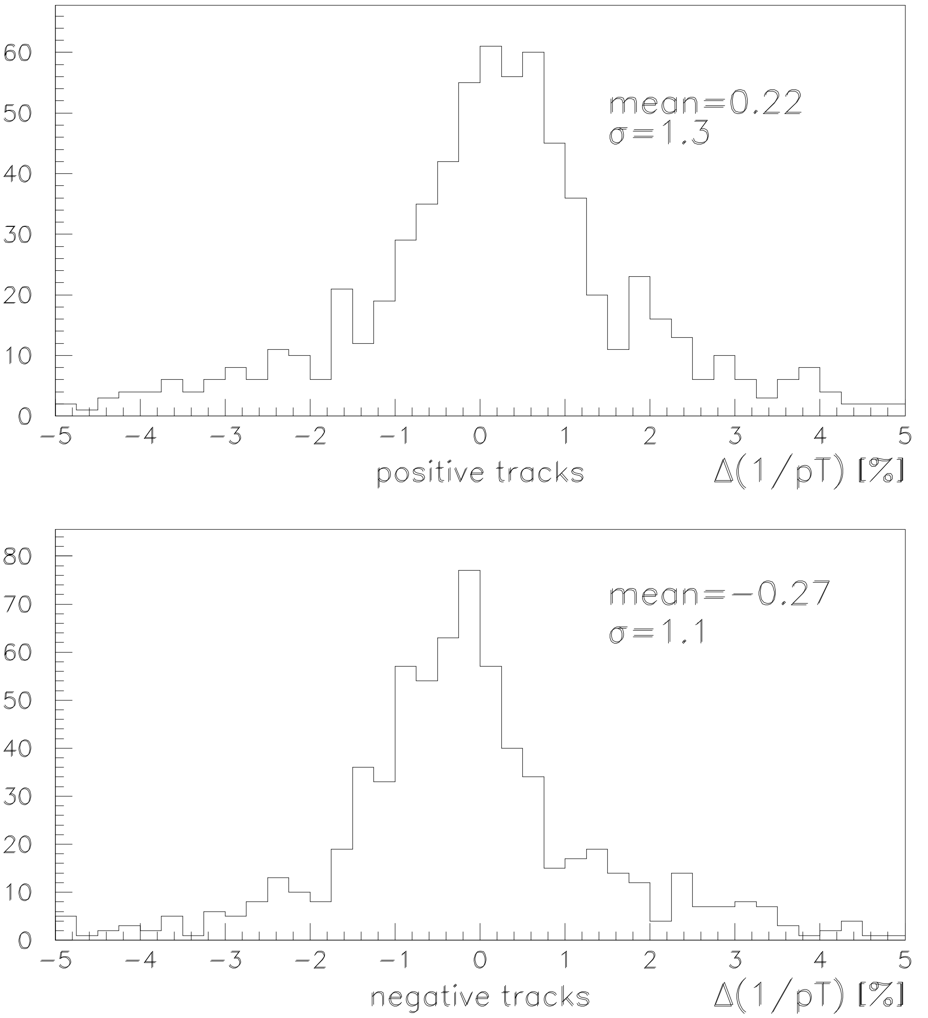

Figure 3.5: *Impact of the alignment corrections on positive and negative high-energy muon tracks (upper and lower plots) in Run I using the CTC. The difference of* $1/p_T$ *has been taken between tracks fitted with and without alignment corrections.*

3.4 The track-residuals in Run II

A tool to study the internal misalignments of a tracking chamber is provided by the residuals of the track-fits. Despite the fact that some tracking bias is only visible when compared to external information, such as the electron energy from the calorimeter, the track-residual patterns can show many of the problems in a track-fit. The quantity in the numerator of Equation 3.6 defines the residuals of the track-fit:

$$ResD_h = (|\tilde{D}_h(\vec{p})| - |D_h|). \tag{3.13}$$

When looking at internal alignment it is convenient to multiply the residuals by the sign of the drift-velocity:

$$ResY_h = \text{sign}[\tilde{D}_h(\vec{p})] \cdot ResD_h = \text{sign}[\tilde{D}_h(\vec{p})] \cdot (|\tilde{D}_h(\vec{p})| - |D_h|). \tag{3.14}$$

The sign of the drift-velocity is given by the position of the hit around the wire (to one side or the other along the drift-velocity direction). With this choice of the sign, $ResY$ as seen as a function of the true hit position is a symmetric function for sense-wire displacements, and anti-symmetric for most of the calibration effects. Hence, the mean of $ResY$ is sensitive to the sense-wire alignment, whereas most calibration effects cancel.

The impact of the COT survey measurements:

At the end of the construction of the COT a set of measurements of slot positions, end-plate deflection etc., were recorded. This set of data goes into the geometric description of the COT used by the reconstruction code. A comparison between the track-fit that uses the COT nominal geometry and the one with a more complete chamber description shows clearly the improvement in the resolution and in the residuals distributions. It also highlights the correlation between residuals and geometric distortions. It is worth stressing here that it is not the distortions of the chamber that cause a track-bias *per se*, but rather the inadequate representation of the geometry in the reconstruction code. Three versions of the chamber's geometry, in the reconstruction code, are considered here for comparison. The first is the nominal COT geometry, described in the CDF Technical Design Report [42] (TDR). The second is the geometry improved with the measured radii of the super-layers, determined from the measured slot positions , averaged over all the slots in a given super-layer (C1). The third is the complete geometry description, that includes corrections at the cell level (C2).

Figure 3.6 shows the signed residuals versus layer number from the tracks seen in the COT. The data were collected in October and November 2000. Tracks and hits are selected according to the following quality cuts:

Good super-layer:	at least two hits on each side of the track and at least 6 hits in total
Good Track:	$\lvert p_T \rvert > 400$ MeV ; $\lvert d_0 \rvert < 1$ cm $\lvert z_0 \rvert < 50$ cm ; $\lvert z_{at\ r=120} \rvert < 100$ cm $\geq$2 good Axial SL ; $\geq$2 good Stereo SL
Good Hit:	$\lvert \mathrm{WireDist} \rvert > 0.2$ cm ; $\lvert \mathrm{SheetDist} \rvert < 0.2$ cm $\lvert \sin\alpha \rvert < 0.1$; Width=15−50 ns

The residuals plot in Figure 3.6 shows the difference between using TDR and the C1 correction. It has consecutive slopes, interrupted at the boundaries of each super-layer − ideally it should be approximately flat. The difference between TDR and C1 is an adjustment in the average radius of the super-layers[3]:

---

[3] The COT construction specifications were different from the TDR values, but the reconstruction code used the TDR as base geometry at first, and the difference is shown here as an example.

	Resolution [μm]		
SL number	C1 geometry	C2 geometry	Improvement [μm]
SL1	279	260	-19
SL2	273	264	-9
SL3	217	208	-9
SL4	230	221	-9
SL5	217	211	-6
SL6	213	212	-1
SL7	199	198	-1
SL8	229	227	-2

Table 3.2: *The hit resolution (in μm) seen on each super-layer. The two columns compare the track-fits based on two versions of the chamber's geometry (C1 and C2, see text for the definition).*

ΔR(SL)=0.77,0.51,0.28,0.05,$-$0.18,$-$0.41,$-$1.64, $-$1.88 cm for SL = 1$-$8. The reason why the SL radii affect the residuals arises from the fact that within a SL, tracks cross several cells due to the significant tilt angle and the small cell width. Just making this correction dramatically improves the residuals.

Using the C2 geometry further improved the track-fit. Figure 3.7 (upper-left) shows the hit residuals averaged over all super-layers. The width is 235 μm, a very good result for such an early stage, when the calibration of the drift model was still being refined. The best resolution which could be expected is 180 μm – this is limited by the ionisation and charge collection mechanisms. The resolution on each super-layer also improved, as shown in Table 3.2. The remaining pictures in Figure 3.7 show the residuals versus aspect-angle, hit-distance from the field-sheet in the cell and z-coordinate of the hit. The dependencies are slightly reduced and no strong patterns can be seen. However, the residuals versus wire-number

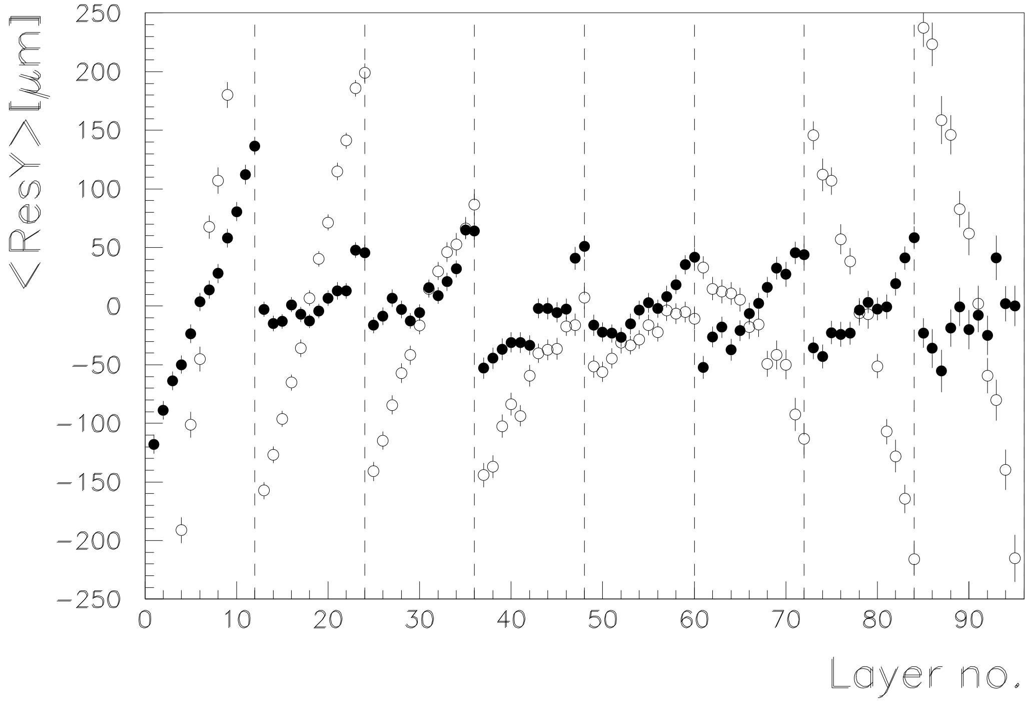

Figure 3.6: *The difference between track-fitting with COT nominal geometry (TDR) and the geometry corrected with the measured radii of the super-layers (C1). Open circles are TDR geometry, filled circles use C1. The dashed lines indicate the super-layer boundaries, the COT has a total of 8 super-layers.*

dependence did not change significantly.

In conclusion, the COT survey measurements indicate that the chamber has a compression in SL radii, i.e. a radial movement to larger radii of the first few SL's, and to smaller radii of the outer SL's. Also the end-plates are curved as result of the wire tensions. The biggest correction is on the first SL, where the curvature of the end-plates is biggest. Aspect-angle dependences are improved only when including the complete COT geometry (C2), which allows for the measured tilt of each cell.

3.5 Mapping super-layer distortions against residuals' patterns

The calibration of the drift-model was completed during the first few months of the commissioning run, and all the available data from the COT survey was implemented in the geometric description. However, the residuals from the track-fit of the data of June 2001 still had a pattern of slopes as a function of layer number, as shown in Figure 3.9 (upper-left). The biggest effect is about 80 μm and is visible on the first super-layer; on other SL's, the effects are less than 50 μm. Assuming that this is a measure of the current internal misalignments, then at this level the pattern-recognition[4] should be largely unaffected, as long as hits are efficiently matched to tracks. The remaining concern is that of systematic biases for physics analysis.

The residuals patterns like the one shown in Figure 3.9 can have several causes. In order to study the relationship between geometrical effects and these patterns,

---

[4] Several detector triggers rely on the pattern-recognition, so it's crucial that the misalignment of the chamber is small enough to leave the pattern-recognition efficiency unaffected.

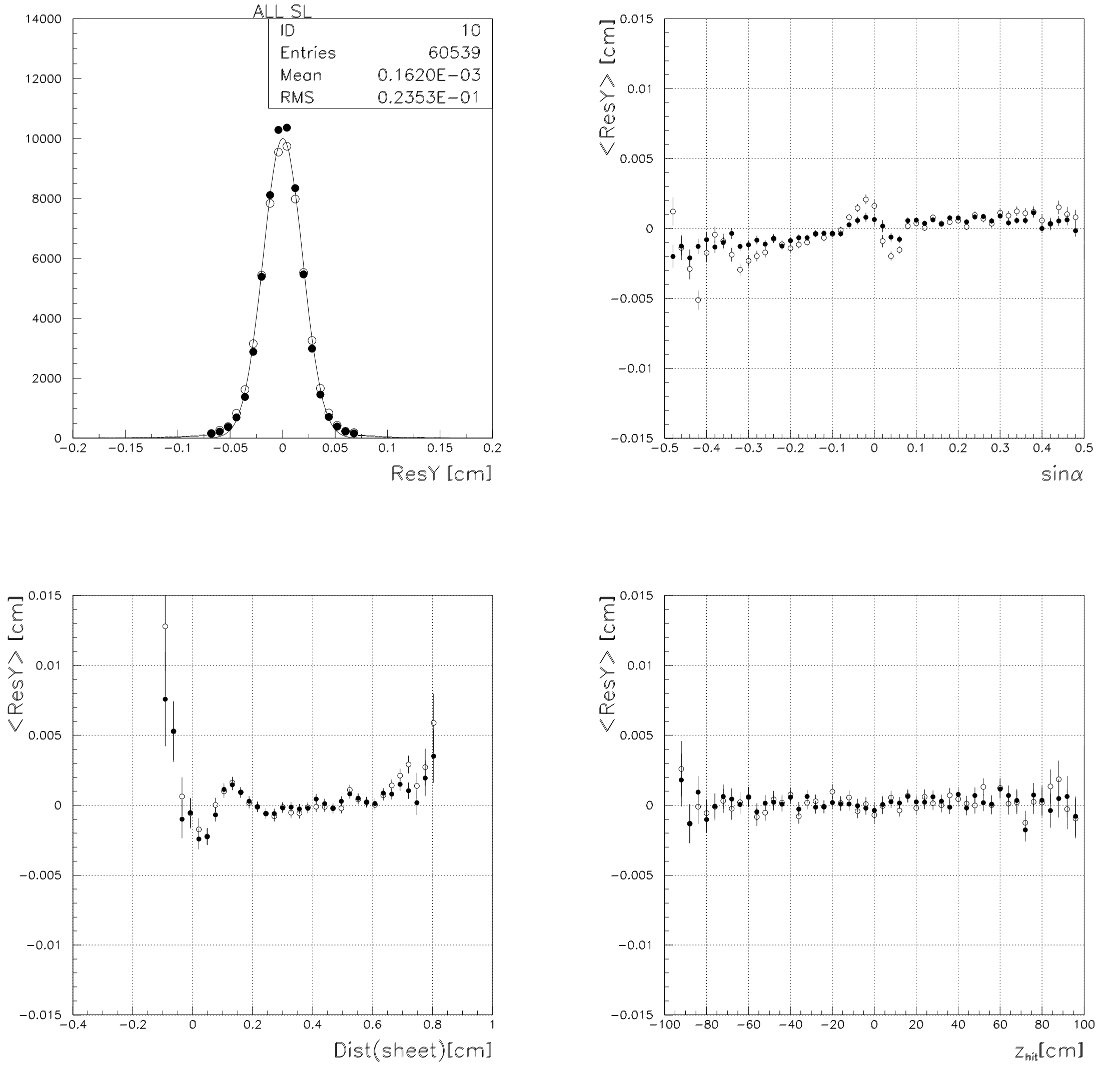

Figure 3.7: *Plot of the signed residuals: upper-left is the distribution integrated over all the super-layers, the remaining plots show the signed residuals versus the track aspect-angle (upper-right), the hit distance from the field sheet (lower-left), the z-position of the hit (lower-right). Open circles are obtained using the geometry corrected with the measured radii at the super-layers (C1), filled circles are obtained using the geometry improved with the complete COT survey (C2).*

the track-fit applied to a set of data has been repeated with different types of misalignments which may be expected, so as to observe the related patterns of residuals. The following is a summary of this exercise.

The first step is to identify some representative misalignments to apply to the chamber's geometric description. The first super-layer is chosen for this study. Each cell is considered as a rigid body with three degrees of freedom in the $r - \phi$ plane (2 translations + 1 rotation around the centre). A factor that scales the inter-wire distance is also allowed. The following distortions have been applied: 1) a cell rotation (correlated to a change in the Lorentz-angle); 2) translations of the whole cell along a radial line from the COT centre, or perpendicular to it (as in a ϕ rotation); 3) a change to the inter-wire separation. When these effects are parametrised as smooth functions of r and ϕ, they correspond to large scale distortions of the complete COT, such as differential rotations in ϕ as a function of r, or multi-pole (elliptical, pear-shaped) distortions. Each misalignment is applied to all cells of SL1 together. The tracks are then reconstructed with the modified geometry and the patterns of residuals are considered. The following quantities are determined to monitor the patterns:

- the slope of the means of the residuals versus wire-number (S-plot)
- the slope of the *difference* of the means of the residuals from positive and negative aspect-angle tracks versus wire-number (A-plot)

If the geometrical description is correct, the residuals of positive and negative aspect-angle tracks should look the same and the A-plots should not exhibit any effects. Figure 3.8 illustrates the results of a radial wire-offset. Consequently, the tracking code reconstructs the hit in a shifted position: the hit will be displaced away from the wire, with respect to the actual track, for a negative aspect-angle track; but it will be displaced toward the wire for a positive aspect-angle

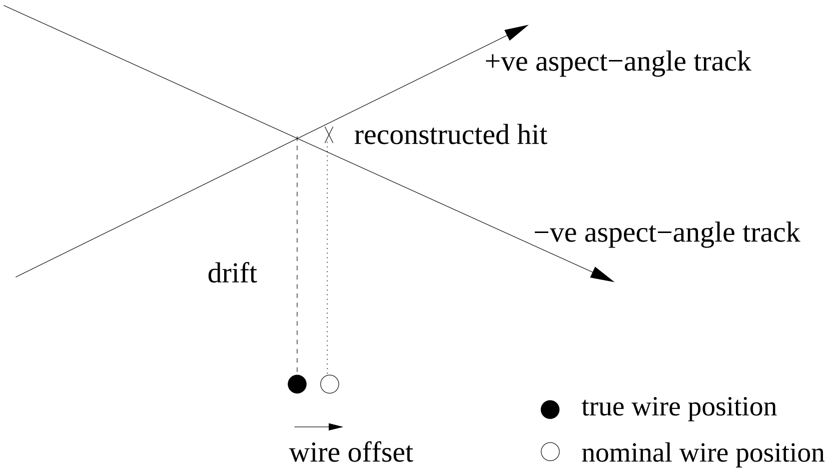

Figure 3.8: *Sketch of the effect of radial wire-offsets on positive and negative aspect-angle tracks.*

track. Therefore, looking at the difference of the residuals for the two signs of the aspect-angle (A-plot) will enhance the effect of radial wire-offsets. Figure 3.9 (upper-right) shows the residuals in the A-plot, from COT data.

By applying each of the described misalignments to the first super-layer, a set of resulting patterns can be observed. These are described qualitatively in Table 3.3. A slope of the residuals versus wire number (the S-plot) can be caused by a small cell tilt, as well as by a radial shift of the cells (as seen in Figure 3.6), or by a small correction to the wire-to-wire distance. All these are due to the fact that within a SL, tracks cross several cells. If a SL is rotated (in ϕ around the origin of the chamber), the set of hits on that SL, from a radial track for instance, would be reconstructed coherently shifted. Therefore, most commonly this appears as a shift in the S-plot (but not a slope). Slopes in the A-plot mean that the positive and negative aspect angle tracks have different residuals distributions. They appear when the inner and outer wires of a SL have a radial offset in opposite directions. This may be caused by a cell tilt, or a wire-to-wire separation. A radial shift would offset the inner and the outer layers in the same direction, and cause mainly an offset in the plot. Another useful quantity is the impact parameter. The distribution of this should be centred on zero, but a rotation which causes different SL's to be rotated by different amounts (as a twist of the inner versus outer SL's) will cause the tracks to tend to converge to a circle centred on the interaction point, corresponding to a non-zero mean of the impact parameter. At times, other misalignments on the inner SL's may also offset the impact parameter, depending on how the particular misalignment affects the track-fit.

Observed pattern or effect	Probable cause
S-plot: slope versus wire-number	– cell tilt – radial shift – wire-to-wire separation
S-plot: shift versus wire-number	– SL rotation
A-plot: slope versus wire-number	– cell tilt – wire-to-wire separation
A-plot: shift versus wire-number	– radial shift
Impact parameter offset	– SL rotation – radial shift – wire-to-wire distance – cell tilt

Table 3.3: *Observable patterns and their possible causes.*

Although several misalignments appear causing the same residual patters, the amounts for each of those to cause a given slope or shift, can be very different. For example, a radial shift of the order of several millimetres is needed to observe slopes like the ones in Figure 3.6. Just a few microns correction to the cell tilt or

distortion	slope in S-plot [μm/wire]	slope in A-plot [μm/wire]
cell tilt	(5.4 ± 0.2)/mrad	(0.55 ± 0.17)/mrad
wire separation	$(0.54 \pm 0.01)/\mu$m	$(-0.133 \pm 0.025)/\mu$m
SL radial shift	$(0.0062 \pm 0.002)/\mu$m	$\leq 0.003/\mu$m
SL ϕ rotation	a horiz. shift, no slope	$< 0.002/\mu$m

Table 3.4: *The residual patterns, seen in the S and A plots, resulting from various distortions in the first COT super-layer.*

to the wire distance are sufficient for the same effect. Table 3.4 summarises the magnitude of the effects seen in the residuals resulting from a given distortion. The table is constructed using the first super-layer. Since the measured slopes from data are:

$$(16.3\pm0.2)\ \mu\text{m/wire} \qquad \text{(S-plot)}$$

and:

$$(2.46\pm0.42)\ \mu\text{m/wire} \qquad \text{(A-plot)}$$

when these are combined with the information of Table 3.4, the first observation is that a radial misplacement would need to be of the order of 2500 μm to produce the slope seen in the data. Hence, is excluded because the precision on the geometrical survey is approximately 100 μm. Also a SL rotation is excluded because its pattern is mainly a shift of the residuals rather than a slope. What is left is a cell tilt and an inter-wire separation term. Solving the system of two equations, results in the following corrections:

$$\Delta\ \text{tilt} = 3.4\pm1.8\ \text{mrad}$$
$$\Delta\ \text{wire separation} = -4.6\pm2.0\ \mu\text{m}$$

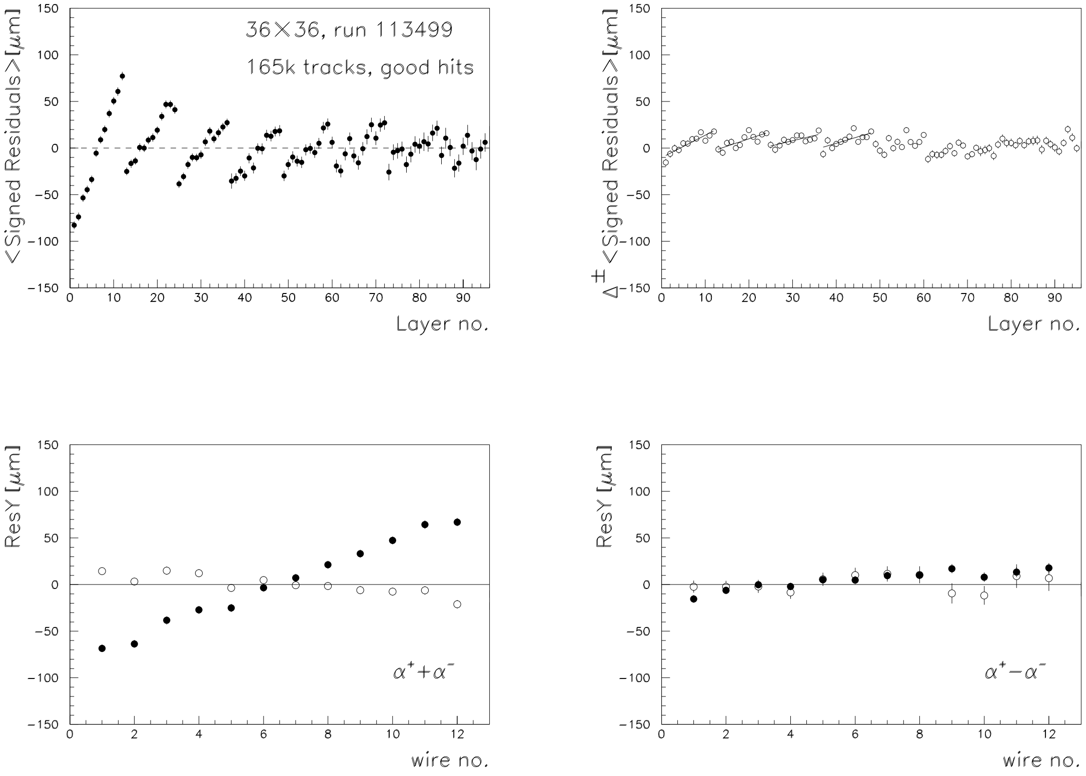

Figure 3.9: *Upper plots: the mean residuals versus layer number, seen in the data collected during June 2001. Left-plot shows the mean residuals for hits of positive and negative aspect-angle tracks combined (S-plot); Right-plot is the difference between the mean residuals of positive and negative aspect-angle tracks (A-plot). Lower plots: the improvement of the residuals versus wire-number after adjusting the cell tilt and wire-wire separation in the first super-layer (filled circles – before correction, empty circles – after).*

The corrections are strongly correlated, although the effect of the tilt is dominant. Figure 3.9 (lower plots) shows the improvement of the distribution versus wire-number, after correcting the cell tilt and inter-wire separation in the first super-layer. The distribution of the corrected residuals is now much flatter, although it appears to be slightly over-corrected, so that the plot has acquired a small slope in the opposite direction. Therefore SL1 seems to require a tilt adjustment and a small decrease in the wire separation. An apparent tilt adjustment can be caused by many global deformations, such as end-plate twist (inner versus outer SL's rotate by different amounts, tilting also the cells) or deflection. It is more difficult to explain a wire-to-wire separation correction of a few microns, since the wires are attached to a wire-plane card by a machine whose placement tolerances are of the order of 10 μm across the whole wire-plane. However, SL1 is a stereo super-layer, where the wires are strung between offset slots, therefore it is more difficult to fully interpret these results.

This exercise shows how it is possible to relate patterns in the residual distributions to alignment offsets, and use the relationship to look for specific problems, maybe with survey data or with other information coming from the track parameters. Although it is premature to use this as a well-established alignment procedure at this stage, it could be developed for a better understanding of the tracking behaviour in the future.

Chapter 4

Measurement Strategy and a Preliminary Estimate of the Sensitivity

Before analysing the CDF data, the sensitivity of the measurement of the lepton polar-angle coefficients has been tested with a fast Monte Carlo simulation. This chapter describes the measurement strategy chosen, and shows the results of the statistical error estimate. Two sections are dedicated to measuring α_2 and two are dedicated to a tentative measurement of α_1.

4.1 Overview

To make a measurement of the coefficients of the lepton polar-angle distribution in the W rest-frame, one would like to be able to plot the cosθ distribution and fit for the parameters α_1 and α_2:

$$\frac{\mathrm{d}N}{\mathrm{d}\cos\theta} \propto (1 - P_W Q \cdot \alpha_1 \cos\theta + \alpha_2 \cos^2\theta). \tag{4.1}$$

In Equation 4.1, P_W is the polarisation sign of the W-boson (±1 depending on the colliding quarks) and Q is the W-charge sign. However, since the neutrino coming from the W decay is undetected, and the kinematics of the decay are not completely reconstructed, it is not easy to perform a boost into the W rest-frame and determine cosθ. It turns out that there is sensitivity to $|\cos\theta|$, and therefore α_2, however accessing the sign of cosθ and hence α_1 is much more challenging.

4.2 Measurement strategy for α_2

The lepton angular distribution summed over both lepton charge signs is sensitive to α_2 and has the advantage of being largely independent of α_1:

$$\frac{\mathrm{d}N^+ + \mathrm{d}N^-}{\mathrm{d}\cos\theta} \propto 1 + \alpha_2 \cos^2\theta. \tag{4.2}$$

Equation 4.2 is a parabola in cosθ, although acceptance cuts modify the shape and limit the sensitivity to α_2. Figure 4.1 shows the charge-inclusive cosθ distribution, at Monte Carlo generator level, for values of $\alpha_2 = 0.0, 0.6, 0.8, 1.0$. Acceptance cuts have been applied.

There are at least two methods to measure α_2 using a charge-inclusive W sample. The first exploits the relationship between the transverse-mass and the $|\cos\theta|$ of

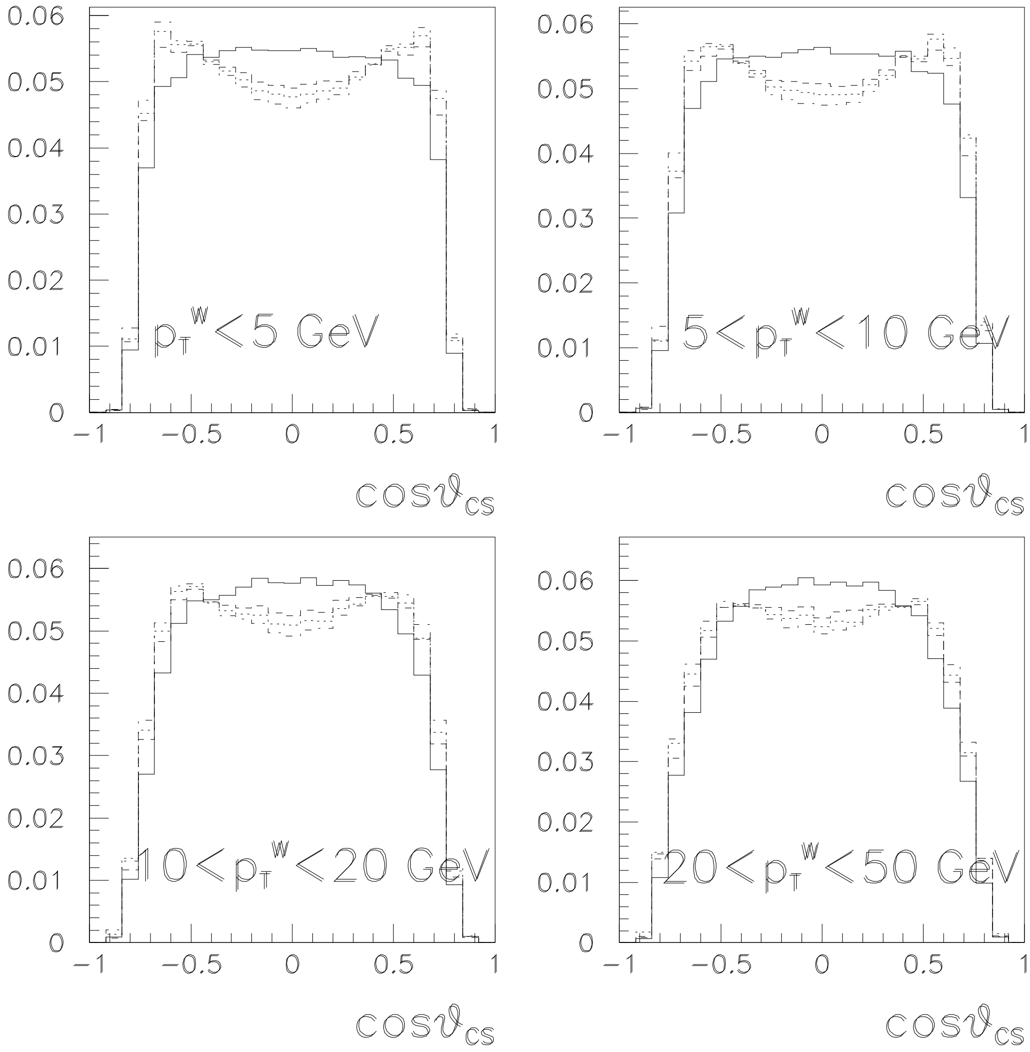

Figure 4.1: *Lepton polar-angle distribution from the Monte Carlo generator in the W rest-frame. Four ranges of the transverse-momentum of the W are shown here (indicated on the plots). For each plot, the value of* α_2 *has been assigned as: 0.0 (continuous line), 0.6 (dashed), 0.8 (dotted), 1.0 (dashed-dotted). Acceptance cuts have been applied to the sample.*

the decay lepton. The second method uses the boost to one particular W rest-frame. This is the Collins-Soper[1], where the cosθ can be reconstructed from laboratory-frame variables, except for a sign ambiguity. These techniques are explained below.

Measuring α_2 using the transverse-mass:

It was mentioned in Chapter 1, in relation to the W mass measurement, that the transverse-mass has a dependence on $\cos^2\theta$. This can be shown by expressing the transverse-mass explicitly, as a function of the lepton angles in the W rest-frame [57]:

$$M_T^W = m_{e\nu}\sqrt{\sqrt{a_0 + a_1\gamma^2 + a_2\gamma^4} + \sin^2\theta_{CS} - \gamma^2(1-\cos^2\phi_{CS}\sin^2\theta_{CS})}. \tag{4.3}$$

Equation 4.3 is written in the Collins-Soper (CS) rest-frame, $m_{e\nu}$ is the invariant-mass of the $e\nu$ system and γ, a_i coefficients are defined as:

$$\begin{aligned}
\gamma &= \frac{p_T^W}{m_{e\nu}} \qquad (4.4)\\
a_0 &= \sin^4\theta_{CS}\\
a_1 &= 2\sin^2\theta_{CS}(\sin^2\phi_{CS} - \cos^2\phi_{CS}\cos^2\theta_{CS})\\
a_2 &= (1-\cos^2\phi_{CS}\cos^2\theta_{CS})^2
\end{aligned}$$

Thus the transverse-mass distribution is a function of $\cos^2\theta$, but not of $\cos\theta$, therefore it is a handle to measure the coefficient α_2. Figure 4.2 shows the sensitivity of the transverse-mass line-shape to α_2 for $p_T^W < 20$ GeV. α_2 has been varied between 0 and 1. The independence of the transverse-mass to α_1 holds exactly only with perfect detector efficiency and acceptance. A small residual

---

[1] There is no unique rest-frame – since there is a free choice of the direction of the axes. In the Collins-Soper frame, the axes are chosen such that the $p\bar{p}$-pair lies in the xz-plane and the z-axis bisects the angle between the proton and negative antiproton momenta.

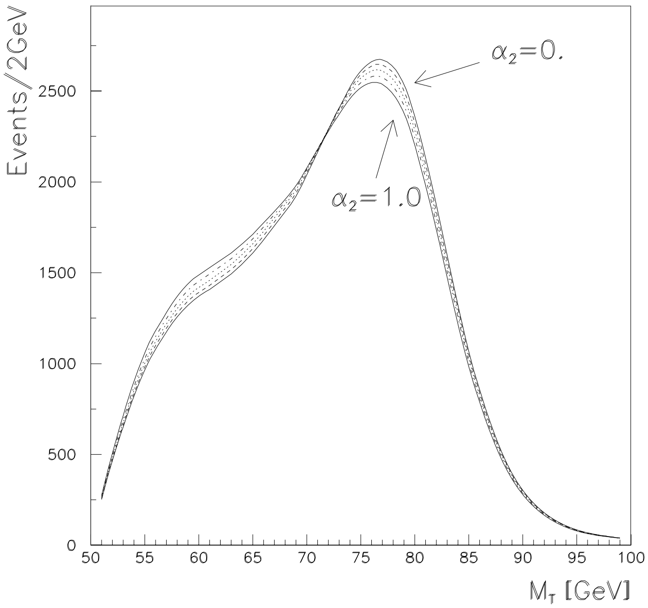

Figure 4.2: *The sensitivity of the transverse-mass to* α_2 *for* p_T^W *<20 GeV.* α_2 *has been varied between 0. and 1.0.*

dependence is observed in the Monte Carlo, and is discussed further in the context of the simulation of W events (Chapter 6), and the systematic errors of the measurement (Chapter 8).

It would be nice were it possible to solve Equation 4.3 for $\cos^2\theta$, and measure directly the distribution of $\cos\theta$. However, the invariant-mass of the $e\nu$ system ($m_{e\nu}$) in the event is not known. To first order it can be approximated with M_W, but as a consequence of the approximation and of the kinematic smearing, the quadratic Equation 4.3 often will not have a solution. Therefore to measure α_2 with the transverse-mass distribution method, the distribution of the W data is fitted with a set of Monte Carlo templates, generated at different α_2.

A variant of this method is to reconstruct the angular distribution from the transverse-mass with a Bayesian unfolding method, as was done in [36]. The M_T

distribution is unfolded with:

$$\frac{\Delta N}{\Delta_i |\cos\theta_{CS}|} = \sum_j f_{ij} \frac{\Delta N}{\Delta_j m_T}, \tag{4.5}$$

where the left-hand side is the desired distribution and the right-hand side is the measured transverse-mass histogram. The coefficients f_{ij} are determined using a high statistics Monte Carlo as:

$$f_{ij} = \frac{N^{MC}_{i,j}}{\sum_k N^{MC}_{i,k}}, \tag{4.6}$$

where summation is over bins k in $\cos\theta_{CS}$. The $N^{MC}_{i,j}$ are the number of Monte Carlo events in bin i, j obtained from a correlation plot of M_T and $|\cos\theta_{CS}|$. Since this is just a change of variable, the sensitivity to α_2 should be unchanged by the unfolding, therefore the fits to the transverse-mass will be used in this analysis.

Measuring α_2 using the Collins-Soper frame:
The Collins-Soper frame has the property that the lepton *transverse* components can be expressed in terms of the measured laboratory-frame variables. Moreover, the *longitudinal* component of the lepton is determined up to a sign. This is sufficient to reconstruct $|\cos\theta|$. However, the relationship between the lab-frame and the CS-frame requires the knowledge of the invariant-mass of the $e\nu$ system. It is the same difficulty observed earlier in the attempt to solve Equation 4.3, and leads to a loss of sensitivity to α_2. Therefore fitting the transverse-mass distribution has been preferred to a partial reconstruction of $\cos\theta_{CS}$.

4.3 An estimate of the sensitivity to α_2

A data-set of $W \to l\nu$ events, has been simulated with a fast Monte Carlo (MC), reproducing the same statistics as the data collected at CDF during Run Ib. The

Monte Carlo generator is used also for the more accurate simulations of W events in this analysis, described in Chapter 6. The detector response is modelled at first order by applying smearing functions to the generated kinematics. The track curvature is replaced by:

$$C = \frac{1}{p_T} + G(0,1) \cdot 0.94 \cdot 10^{-3}\ \mathrm{GeV}^{-1}, \tag{4.7}$$

where $G(0,1)$ is a random number extracted according to a Normal distribution (mean 0, rms 1). The transverse-momentum of the W-bosons is smeared with:

$$\vec{p}_s^{\,W} = [1 - A(p_T^W)] \cdot \vec{p}^{\,W} + B \cdot G(0,1) \cdot \hat{n}, \tag{4.8}$$

where A is a function of p_T^W and B is a constant term. The neutrino transverse components are calculated back from the W and the lepton kinematic.

The MC sample representing the data has unweighted distributions with Poisson errors. To obtain these distributions from a weighted Monte Carlo, the MC weight WT is compared to a uniform random number R, between 0 and the overall maximum weight assigned ($MaxWT$). Events are then kept or rejected according to:

$$R = \mathrm{random}[0, MaxWT] \qquad \begin{array}{l} WT > R \Rightarrow \text{ keep} \\ WT < R \Rightarrow \text{ reject} \end{array} \tag{4.9}$$

The sample has 46,395 accepted $W \to \mu\nu$ events. Only about 5% of the total number of events has a transverse-momentum greater than 20 GeV. In the lepton polar-angle distribution of the MC events, α_1 has been set to zero, α_2 has been assigned the Standard Model expectation, as a function of p_T^W.

The transverse-mass distribution of this sample was compared with a set of templates obtained with different values of α_2. A log-likelihood method was then applied to fit for the best value of α_2. The best value is labelled $\hat{\alpha}$. The data is divided in four ranges of the W transverse-momentum: 0−5 GeV, 5−10 GeV, 10−20 GeV, 20−50 GeV, and α_2 is measured separately in each p_T^W range.

To estimate the sensitivity, the complete procedure has been repeated with several independent samples simulating the data (a set of N "CDF experiments"). The estimate of α_2 from all the simulated "CDF experiments" gave a set of measurements: $\hat{\alpha}_i$ ($i = 1, .., N$). The average of the N fits (μ), compared to the value input in the MC generator, indicates the systematic bias of the technique. Moreover, the dispersion of the $\hat{\alpha}_i$ values gives a 1σ estimate for the statistical error of the measurement:

$$\sigma = \sqrt{\frac{\sum_i^N (\hat{\alpha}_i - \mu)^2}{N-1}}. \qquad (4.10)$$

Such estimates have errors themselves, which are used to decide when the number of simulated experiments (N) is sufficient to have good estimate of σ. The error on σ is given by [58]:

$$var[\sigma] = \frac{1}{4\sigma^2} var[\sigma^2] = \frac{\sigma^2}{2(N-1)}. \qquad (4.11)$$

In Equation 4.11 it has been assumed that the distributions are Gaussian, so that:

$$var[\sigma^2] = \frac{2\sigma^4}{N-1}. \qquad (4.12)$$

The results of this simulation are shown in Table 4.1.

Figure 4.3 shows the mean estimated values of α_2 at various p_T^W, compared to the Standard Model expectation. The position of the points along the x-axis has been corrected to account for the difference between the measured W-recoil and the true p_T^W as well as allowing for the distribution of the true p_T^W within the bin. The first part of this is because, due to cracks in the calorimeter, not all the energy is detected and the measurement of the recoil against the W tends to

W-recoil range	N	μ	$\Delta\mu$	σ	$\Delta\sigma$	μ-α_2(SM)
0−5 GeV	11	1.01	±0.03	0.097	±0.02	+0.02
5−10 GeV	11	0.93	±0.02	0.067	±0.01	−0.03
10−20 GeV	20	0.80	±0.04	0.17	±0.03	−0.04
20−50 GeV	29	0.42	±0.07	0.36	±0.05	−0.05

Table 4.1: *The simulation of the measurement of* α_2 *in four W-recoil ranges.* N *is the number of "CDF experiments" simulated,* μ *is the average of the best fits for* α_2 *and* σ *is the statistical error estimate. Their uncertainties are* $\Delta\mu$ *and* $\Delta\sigma$.

underestimate the true W transverse-momentum. Table 4.2 shows, for each W-recoil region, the corresponding average "true" p_T^W. The value has been obtained from the mean of the true p_T^W distribution corresponding to a certain W-recoil range. The measurement of α_2 in a recoil range is interpreted as a measurement at the average true p_T^W. This is justified in Appendix A, and the agreement between the Standard Model curve and the points is a cross-check that this approach is indeed correct.

Centre of the W-recoil bin [GeV]	Average "true" p_T^W [GeV]
2.5	4.7
7.5	7.9
15	17.8
35	40.0

Table 4.2: *The positioning of the data points correcting for the difference between the W-recoil and the true* p_T^W.

The plot in Figure 4.3 summarises therefore the expectations for the measurement

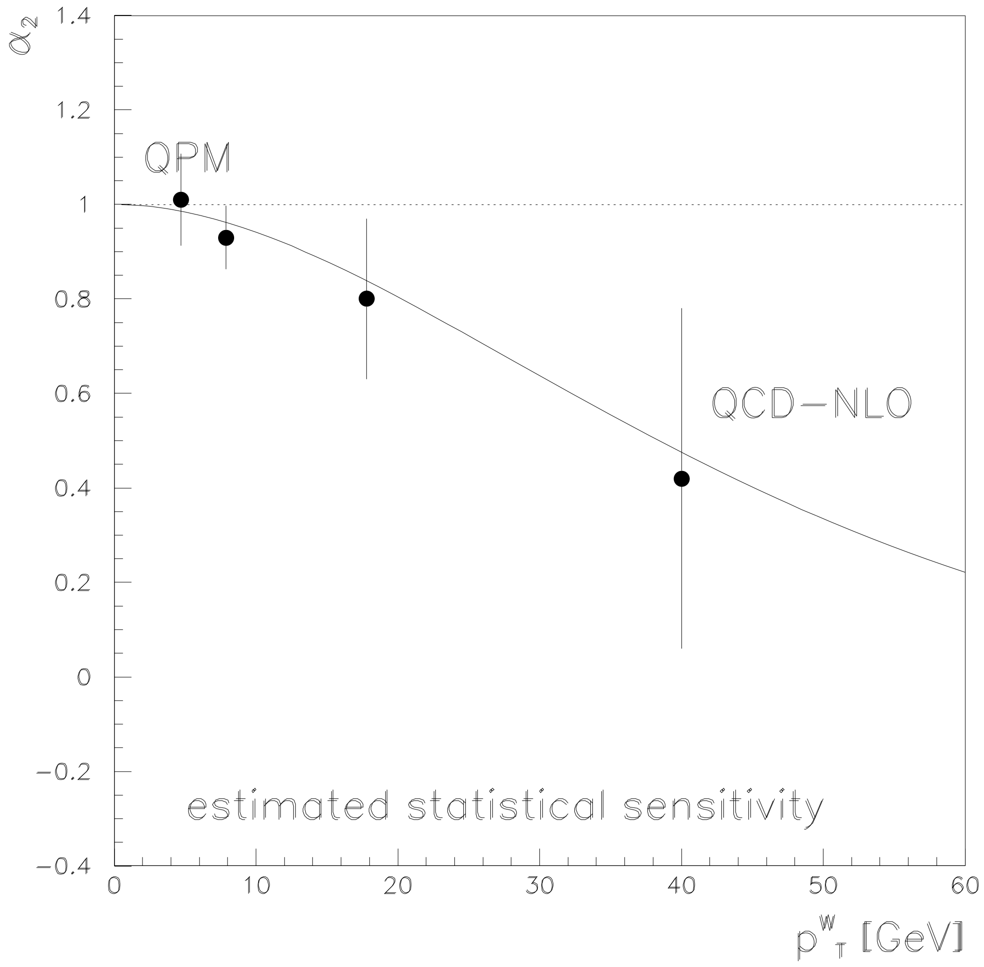

Figure 4.3: *Estimated statistical sensitivity to* α_2*, based on the measurement in four W-recoil ranges. The continuous line is the Standard Model expectation for* $\alpha_2(p_T^W)$*; the points are the average (*μ*) over many MC "experiments" of the fitted values of* α_2*; the error bars are the statistical error estimates (*σ*), not the error on the average.*

of α_2 using the CDF detector, with a sample of approximately 40,000 $W \to l\nu$ decays.

4.4 A tentative measurement of α_1

As a measurement strategy for α_2, the charge-inclusive distributions have been preferred, in order to reduce the α_1 dependence of the spectra and because they are more straightforward. On the other hand, to measure α_1, the signs ± 1 in front of α_1 in Equation 4.1 must not be ignored by combining the two distributions. Therefore, it is essential to measure the signs of both the lepton charge and cosθ.

Since CDF is a solenoidal detector, the charge of the lepton is easily measured from the curvature of the tracks. A complete measurement of cosθ, including its sign, is possible only with a boost into the W rest-frame. By identifying the missing transverse-energy in the detector with the neutrino p_T, the W mass constraint, applied to the lepton-neutrino system, gives two solutions for the unmeasured longitudinal component of the neutrino momentum. This ambiguity translates into an ambiguity of the W longitudinal boost, and hence the sign of cosθ. By examining the two solutions, it is possible to select the correct one with a probability greater than 50% (50% corresponds to no discrimination).

The neutrino ambiguity:

Information about the unmeasured neutrino longitudinal momentum p_L^ν can be obtained from the expression for the lepton-neutrino invariant-mass:

$$m_W{}^2 = E^{W2} - p^{W2}. \tag{4.13}$$

The invariant-mass is approximated by the W pole-mass, m_W, and E^W and p^W are expressed in terms of the measured quantities and p_L^ν:

$$\begin{aligned} E^W &= E^l + \sqrt{\not{E}_T{}^2 + p_L^{\nu\,2}} \\ p^{W2} &= p_T^{W2} + \left(p_L^l + p_L^\nu\right)^2 . \end{aligned} \tag{4.14}$$

After much algebra, the final quadratic equation for p_L^ν is:

$$(4E^{l2} - 4p_L^{l\,2})p_L^{\nu\,2} + (4p_L^l\gamma)p_L^\nu + (4E^{l2}\not{E}_T{}^2 - \gamma^2) = 0, \tag{4.15}$$

where $\gamma = E^{l2} + \not{E}_T{}^2 - p_T^{W2} - p_L^{l\,2} - m_W{}^2$, and L, T stand for longitudinal and transverse components respectively.

The fact that there are two solutions (ν_1 and ν_2) of the quadratic Equation 4.15 is known as "neutrino ambiguity". The solutions are labelled: $p_L^\nu(\nu_1), p_L^\nu(\nu_2)$. Only one of the solutions corresponds to the actual W decay. Each solution corresponds to a different W rest-frame. In the rest-frames, the lepton and the neutrino are back-to-back (see Figure 4.4), and they correspond to the same values of $|\cos\theta|$, but $\cos\theta$ has the opposite sign.

How to distinguish between the two neutrino solutions:
The variable x_W measures the boost of the W in the laboratory frame. It represents the longitudinal W-momentum as a fraction of the beam energy. The expression is:

$$x_W = p_L^W / E_{beam}, \tag{4.16}$$

and is signed with the direction of flight of the W-boson.

Each neutrino solution gives a different x_W, so the problem is translated into defining the solution with the most likely x_W. If any of the solutions gives $|x_W| > 1$, it can easily be identified as the unphysical one, since $|x_W|$ is bound to be less than 1 by definition. At lower beam energies than the Tevatron, this is a useful tool. About 40% of the cases in the UA1 experiment at CERN ($E_{beam} \simeq 300$

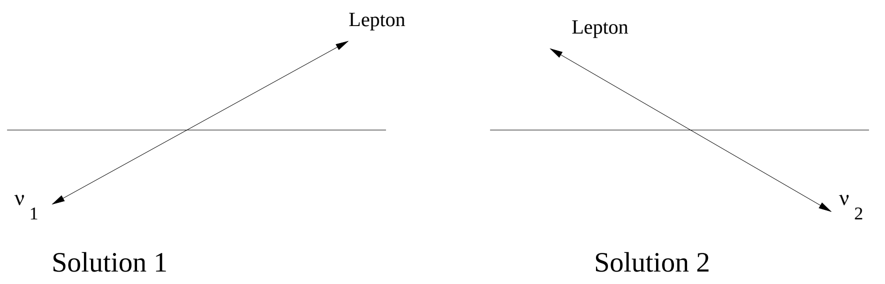

Figure 4.4: *Sketch of the W leptonic decay in the W rest-frames of the two neutrino solutions. Only one solution corresponds to the actual W decay, but seen from the laboratory frame, the two solutions correspond only to a different longitudinal boost of the W, which is not measured.*

GeV) were correctly identified in this way [59]. At CDF, this is much less effective and less than 1% of the cases can be resolved because one of the solutions has $|x_W| > 1$.

Where both solutions have $|x_W| < 1$, it is possible to distinguish by looking at their x_W values. The distribution of x_W for accepted MC W^- events is shown in Figure 4.5 (dashed line). Superimposed are the distributions of $x_W(\nu_1)$ and $x_W(\nu_2)$, from the two neutrino solutions. The distributions have a strong overlap, which makes the selection particularly difficult. For W^-, the ν_2 solution corresponds more closely with the true x_W, which simply means that W^-'s produce more leptons with $\cos\theta > 0$ (the V$-$A effect). If one were to pick ν_2 all the time, this would correspond to plotting the $|\cos\theta|$ distribution, which is not sensitive to α_1. In addition, it can be seen that the x_W histogram is asymmetric, as a consequence of the asymmetry in the quark pdf's responsible for the W-boson production.

One good choice is to select the solution with the slowest W (minimum p_{LW}. Equally suitable is the solution for p_L^W closest to the typical boost, having in mind that negative(positive) charged W-bosons are boosted preferentially backward(forward). For W^--bosons, the mean value of the x_W distribution is about -0.05. Figure 4.6 shows the relation between the "best neutrino" solution, chosen to be the one with x_W closest to $< x_W >= \pm 0.05$, and the "true" x_W from the Monte Carlo. Notice that the "best neutrino" distribution has much shorter

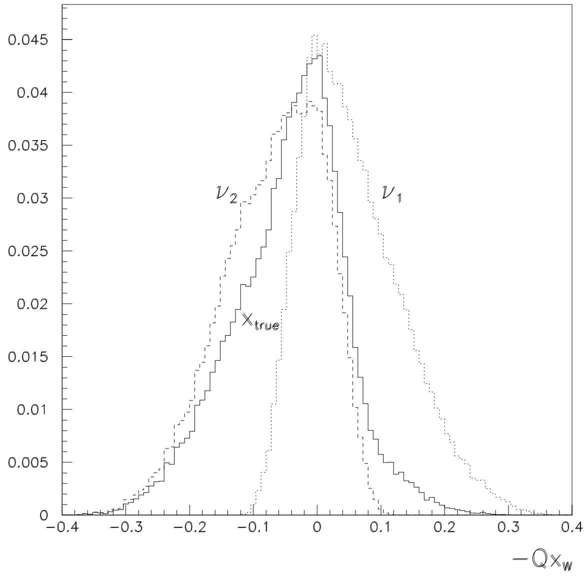

Figure 4.5: $-Qx_W$ *spectrum for accepted events, Q is the W charge. The continuous line is the true distribution; the dashed and dotted histograms represent the spectrum of* x_W *when the* ν_1 *and the* ν_2 *solutions are chosen respectively.*

tails as a result of requiring slow W-bosons.

Efficiency of the selection:

To evaluate the goodness of the procedure for selecting one of the two neutrino solutions, a selection efficiency must be defined. The efficiency should also quantify how effective the procedure is in separating events with $\cos\theta > 0$, from events with $\cos\theta < 0$.

The game of the black and the white balls:

Consider two boxes, a black box with 70 black balls and a white box with 30 white balls. The two boxes are emptied into one single box in the middle. The goal is to put the black balls back in their black box, and the white balls back in their white box. The player is blind. If all the 100 balls are put in the black box, 70 of them are in the right place, but 30 are not. However, the balls have not been separated. To check the colour separation it is natural to count the black balls in their box (they are 100% in this case), and the white balls in the white box (0%). The ideal case would be to have them both in the appropriate box (100% in the white box and 100% in the black box). If instead of putting all the balls in the black box, the player chooses them randomly, they will still tend to be in the ratio black-to-white 70:30 in both boxes − this is irrespective of the total number of balls in each box. An effective way of checking the separation is by looking at the ratio of black-to-white balls in each box.

The case of $\cos\theta > 0$ and $\cos\theta < 0$:

For negatively charged leptons, about 70% of the events have $\cos\theta < 0$. Checking how well they are separated from $\cos\theta > 0$ events is similar to making the ratio of the two colours. The quantity:

$$\epsilon = \frac{N_{corr}}{N_{tot}}, \tag{4.17}$$

is the fraction of the number of correctly identified neutrino solutions over the

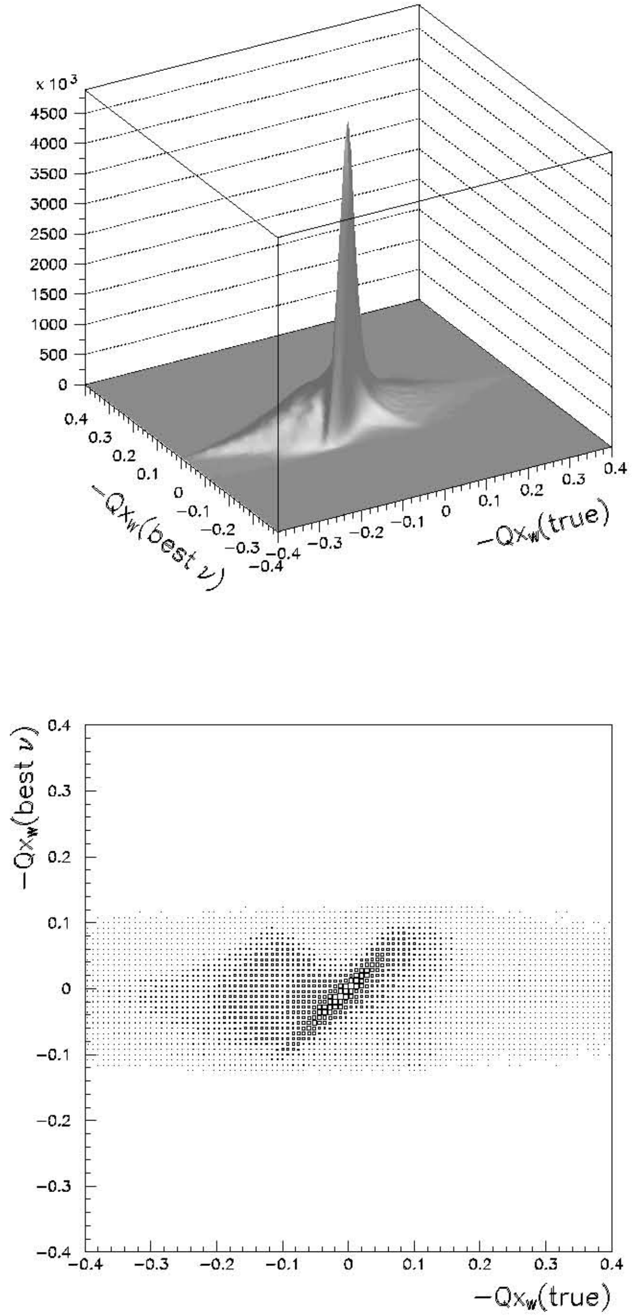

Figure 4.6: x_W *from the "best neutrino" choice versus the true* x_W *distribution. Since the selection prefers "slow" W-bosons, the tails of the true* x_W *distribution are lost.*

total number of cases. ϵ measures the overall efficiency but does not show how good the separation is. The following quantities are useful: ϵ_- is the fraction of events with *negative* $\cos\theta_{CS}$, whose sign is correctly identified:

$$\epsilon_- = \left(\frac{N_{corr}}{N_{tot}}\right)_{\cos\theta<0}. \tag{4.18}$$

ϵ_+ is the ratio of events with *positive* $\cos\theta_{CS}$ whose sign is correctly identified:

$$\epsilon_+ = \left(\frac{N_{corr}}{N_{tot}}\right)_{\cos\theta>0}. \tag{4.19}$$

ϵ_+ and ϵ_- are the equivalent to counting the white balls in the white box and the black balls in the black box. In the case of perfect separation: $\epsilon_+ = 1$ and $\epsilon_- = 1$.

A Monte Carlo sample has been generated and the neutrino selection procedure applied to every event. The selection consisted of choosing always the solution with the smallest $|x_W|$. The result of the selection is cross-checked with the true sign of $\cos\theta$. The results are: $\epsilon_- = 0.60$ and $\epsilon_+ = 0.48$. This means that if a/b is the ratio black-to-white balls, the procedure has given $0.6a/0.52b$ on one side and $0.4a/0.48b$ on the other side. This is slightly better than the random choice, for which every selection would still leave a ratio of a/b. However, it is a very small separation. In general, the ratios of correct to incorrect events on each side are:

$$\left(\frac{\epsilon_+}{1-\epsilon_-}\right)\frac{a}{b}; \qquad \left(\frac{\epsilon_-}{1-\epsilon_+}\right)\frac{b}{a}. \tag{4.20}$$

Therefore, to obtain separation it is required that the quantities in brackets in Equation 4.20 are greater than 1. This corresponds to $\epsilon_+ + \epsilon_- > 1$. Table 4.4 shows the values of $\epsilon_+ + \epsilon_-$ obtained in various cases. The first is the case mentioned above, when the smallest $|x_W|$ is preferred for the neutrino solution. The other values listed come from choosing the solution not with the smallest $|x_W|$, but with x_W closest to: $-Q \cdot n \cdot 0.01$. Q is the electric charge, n an integer

(1,..,5). This accounts for the W asymmetry. In all of these cases the separation power is very small.

n	ϵ	ϵ_+	ϵ_-	$\epsilon_+ + \epsilon_-$
0	0.53	0.60	0.48	1.08
1	0.55	0.55	0.53	1.08
2	0.57	0.51	0.57	1.08
3	n.a.	0.46	0.62	1.08
4	n.a.	0.41	0.66	1.07
5	0.63	0.36	0.70	1.06

Table 4.3: *Indicative efficiency values for the separation of* $\cos\theta > 0$ *and* $\cos\theta < 0$.

The ϵ's numbers could also be checked in different ranges of $\cos\theta$, but they are already indicative of the difficulty of the separation. The conclusive test in any case is the estimate of the statistical error in a measurement of α_1. This is summarised in the next section.

4.5 An estimate of the sensitivity to α_1

The transverse-mass distribution, together with the information on the sign of cosθ_{CS} can be used to measure α_1. The sign information serves to separate the two parts of the signed cosθ_{CS} spectrum. Two transverse-mass distributions are made, one for $Q\text{cos}\theta_{CS} > 0$ and one for $Q\text{cos}\theta_{CS} < 0$. The shape and normalisation of the two transverse-mass plots should differ due to the difference in the shape of the angular distribution for $Q\text{cos}\theta_{CS}$ greater or less than 0.

Alternatively $Q\text{cos}\theta_{CS}$ can be reconstructed as explained in the previous section.

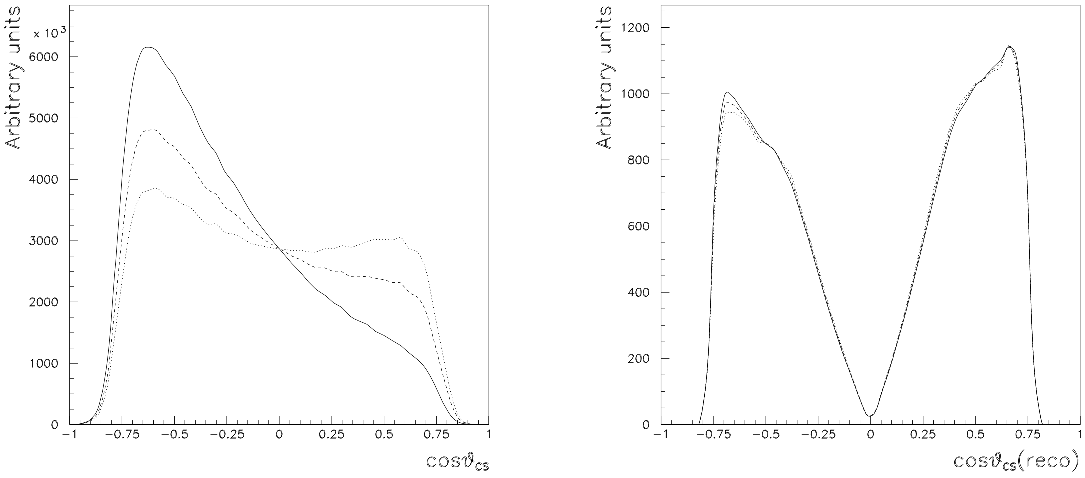

Figure 4.7: *Left:* $\cos\theta_{CS}$ *distribution from the simulation, acceptance cuts have been applied.* $\alpha_1 = 2.0$ *(continuous line), 1.0 (dashed line) and 0. (dotted-line). Right: reconstructed* $\cos\theta_{CS}$ *distribution from lab-frame variables. The dip at zero is due to the event loss when the quadratic equation for* $p_{T\nu}$ *has imaginary solutions.*

There is no harm here in loosing events with no solution to the W mass constraint equation, since it is identically the same events whose neutrino solution cannot be reconstructed. An example of the direct reconstruction of the cosθ_{CS} spectrum is shown in Figure 4.7. The weak sign identification translates into an almost complete loss of sensitivity to α_1.

In analogy with the procedure followed to estimate the statistical error for α_2, a $W \to l\nu$ sample of comparable size to the CDF Run Ib dataset ($\sim$ 40,000) has been used. A set of Monte Carlo templates was generated and fitted to the sample simulating CDF data. The results of the log-likelihood fits are listed in Table 4.4. The values of μ and σ are plotted in Figure 4.8 as the points and error bars respectively. The sensitivity is hardly sufficient to distinguish the QCD

W-recoil range	N	μ	$\Delta\mu$	σ	$\Delta\sigma$	μ-α_1(SM)
0−5 GeV	20	1.81	±0.10	0.46	±0.07	+0.06
5−10 GeV	20	1.48	±0.10	0.50	±0.08	−0.15
10−20 GeV	20	1.55	±0.13	0.61	±0.10	+0.15
20−50 GeV	29	0.99	±0.23	1.25	±0.17	−0.06

Table 4.4: *The simulation of the measurement of α_1 in four W-recoil ranges. N is the number of "CDF experiments" simulated, μ is the average of the best fits for α_1 and σ is the statistical error estimate. Their uncertainties are $\Delta\mu$ and $\Delta\sigma$.*

effects.

A further investigation has shown that most of the information about α_1 that is feeding into the plot of Figure 4.8 is coming from the shape of the transverse-mass distribution. That is via acceptance cuts and efficiencies, rather then from the sign-separation. As a consequence, the measurement is strongly dependent on the accurate detector simulation. This shows that the possibility of measuring α_1 at CDF, with a central lepton (pseudorapidity less than 1) sample, is very limited.

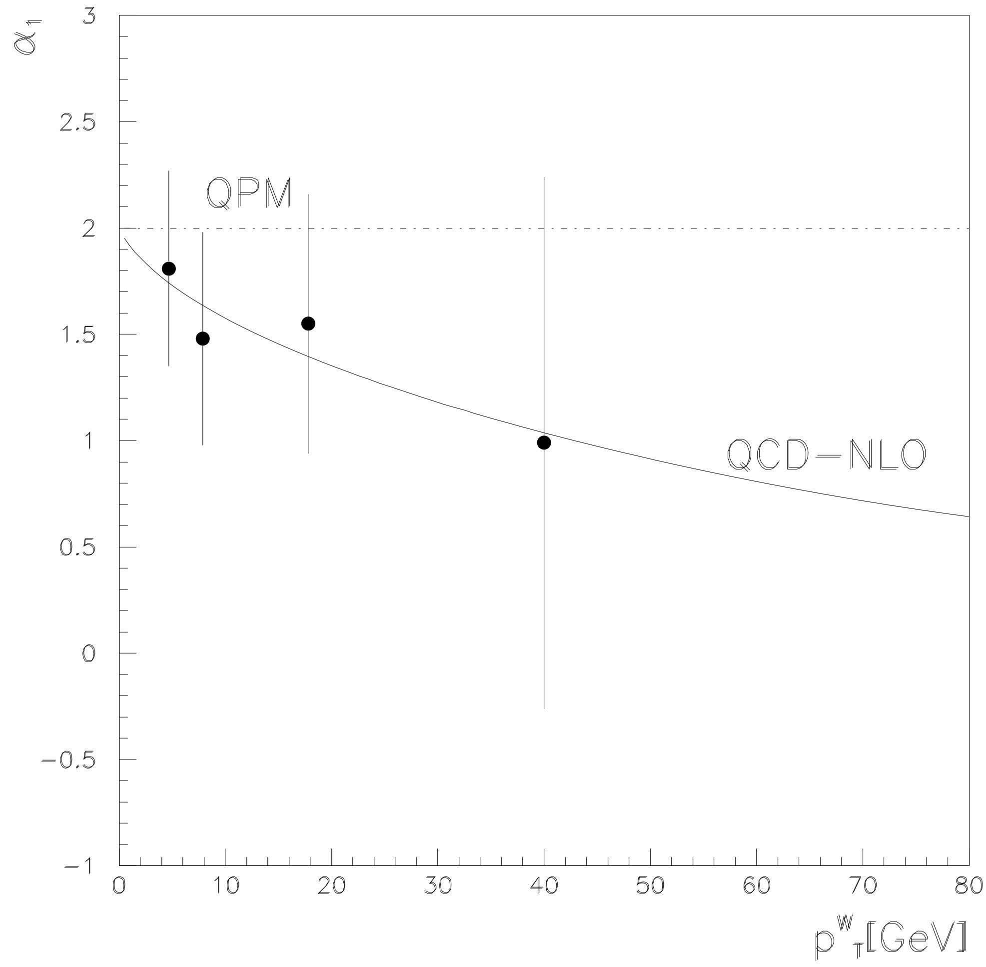

Figure 4.8: *Estimated statistical sensitivity to* α_1, *based on the measurement in four W-recoil ranges. The continuous line is the Standard Model expectation for* $\alpha_1(p_T^W)$*; the points are the averages* (μ) *over many MC "experiments" of the fitted values of* α_1*; the error bars are the statistical error estimates* (σ)*, not the error on the average.*

Chapter 5

Data Handling and Event Selection

The chapter describes the data set used in this analysis and the event selection. The first section defines the event variables, Section 2 presents the $W \to e\nu$ and $W \to \mu\nu$ event selection and Section 3 summarises the corrections applied to the data.

5.1 Event Variables

5.1.1 Particle momentum

The momentum of a charged particle is determined from its trajectory in the CTC. The CTC is operated in a nearly uniform (to within $\sim 1\%$) axial magnetic field. In a uniform field, charged particles follow a helical trajectory. This helix is parametrised by: curvature, C (inverse diameter of the circle in $r-\phi$); impact parameter, d_0 (distance of closest approach to $r=0$); ϕ_0 (azimuthal direction at the point of closest approach to $r=0$); z_0 (the z position at the point of closest approach to $r=0$); and $\cot\theta$, where θ is the polar-angle with respect to the proton direction. The momentum resolution is improved by a factor $\sim$2 by constraining tracks to originate from the interaction point ("beam-constraint"). The z location of the interaction point (IP) is determined using the VTX for each event, with a precision of 1 mm. The z distribution of the IP has an RMS of 25$-$30 cm, depending on the beam conditions. The $r-\phi$ location of the beam-axis is measured with the SVX$'$, as a function of z_0, to a precision of 10 μm. The beam-axis is tilted with respect to the CTC axis with a slope of typically about 400 μm/m.

Two effects are considered also when determining the helix parameters:

- the non-uniformities of the magnetic field are taken into account using the magnetic field map.
- as a consequence of the material between the IP and the CTC tracking volume, the helix parameters measured in the CTC are different than those at the IP. The track-fit accounts for dE/dx, and restores some of the energy loss due to external bremsstrahlung. The material distribution is measured using a sample of photon conversions, where the conversion rate is propor-

tional to the number of radiation lengths crossed.

5.1.2 Electron energy

The energy of an electron signal in the CEM is defined using a clustering algorithm. The electrons deposit 80−100% of their energy in a single tower of the CEM, and nearly all in a single wedge. Therefore a CEM electron (or photon) cluster consists of a seed tower (the tower with most of the energy) and two neighboring towers in η (called "shoulder" towers[1]). The seed tower is searched for through the 48 CEM wedges. In each wedge, towers with deposited energy greater than 3 GeV are sorted by energy. The tower with the highest energy forms a seed and the seed's shoulder towers are marked as ineligible to become seeds while the search for more electromagnetic clusters proceed. The electron energy is therefore the sum of the energies in the seed tower plus its shoulder towers. The reconstructed electron energies never include energy deposited in the neighbouring wedges, since by design, the CEM minimises azimuthal leakage of electron showers. The test-beam response map and the calibration procedure correct the small leakage.

5.1.3 Electron-direction vector

All CTC tracks are extrapolated to the calorimeter to check whether they impact any of the electron cluster's towers. The number of tracks that point to the same electron cluster is called N_{3D} and is stored for possible use as an electron ID (identification) variable. If there is at least one track pointing to the electron cluster, the highest-p_T track is called the "electron track". The electron

---

[1] If the seed tower is the inner or the outer tower of a wedge, then only one shoulder tower is included.

track's helix parameters (without any beam-line constraints) define the electron direction:

$$\vec{E} = \frac{E}{\sqrt{1+\cot^2\theta}}(\cos\phi_0, \sin\phi_0, \cot\theta). \tag{5.1}$$

5.1.4 Electron transverse-energy E_T and momentum p_T

The electron transverse-energy is defined as $E \cdot \sin\theta$, where E is the energy of the electromagnetic cluster and $\sin\theta$ is calculated from the $\cot\theta$ of the track. For muons, the transverse-energy is replaced by the transverse-momentum p_T, determined by the curvature of the track.

5.1.5 Recoil-energy vector $\vec{U}$

The recoil-energy vector $\vec{U}$ is defined as the vector sum of tower transverse-energies over all the calorimeter towers. These include both electromagnetic and hadronic calorimeters out to $|\eta| < 3.6$, except for the towers associated with the electromagnetic cluster that defines the primary electron:

$$\vec{U} = \sum_{i \text{ not } e^{\pm}} E_i \sin\theta_i \hat{n}_i. \tag{5.2}$$

$\hat{n}_i$ is a transverse unit vector pointing to the centre of each tower. In the sum over all the calorimeter towers, the towers with total energies below a threshold of (100,150,200,185,445,730) MeV in the (CEM,PEM,FEM,CHA/WHA,PHA,FHA) are excluded from the sum. For each tower i, sinθ_i is computed using the primary vertex closest to the electron track in z along the beam line, or using the electron track z_0 if there is no vertex within 5 cm of the electron track in z. The recoil-energy vector measures the response of the detector to the recoil against the W, in the $r - \phi$ plane. It is therefore a measurement of the W-boson transverse-momentum. The two projections $U_\perp$, $U_{||}$ of $\vec{U}$ are also used. $U_\perp$ is the projection of $\vec{U}$ perpendicular to the lepton track direction:

$$U_\perp = \frac{|\vec{U} \times \vec{E}_T|}{E_T}, \tag{5.3}$$

and $U_\|$ is the projection along the lepton track direction:

$$U_\| = \frac{\vec{U} \cdot \vec{E}_T}{E_T}. \tag{5.4}$$

The total transverse-energy $\sum E_T$ is the scalar sum of tower transverse-energies:

$$\sum E_T = \sum_{i \text{ not } e^\pm} E_i \sin\theta_i, \tag{5.5}$$

and it is a measure of the total transverse-energy in the event from all sources, excluding the primary-electron.

5.1.6 Missing transverse-energy

The missing transverse-energy is defined as the negative of the sum of the recoil-energy plus the lepton transverse-energy:

$$\vec{\not{E}}_T = -(\vec{U} + \vec{E}_{T\ \text{lepton}}). \tag{5.6}$$

The $\vec{\not{E}}_T$ is identified with the undetected neutrino in the event. CDF cannot measure longitudinal missing energy because many particles are lost at high rapidity, along the beam-line where there is no calorimetry.

5.2 Selection classes

Fiducial requirements:

Fiducial requirements are in place to ensure that the selected data come from regions of the detector with a good and well understood response. For example, since the CDF calorimetry is designed with a tower geometry projecting from the origin, a z-vertex fiducial cut at 60 cm (about 2σ) is set to limit the range of angles at which particles impact the calorimeter.

CDF has also a set of CEM electron fiducial criteria, to eliminate regions of poor response and codified in a software library procedure called FIDELE. The procedure rejects $|x_{CES}| > 21$ cm to avoid the azimuthal boundaries of the CEM, and rejects $|z_{CES}| < 9$ cm to avoid the 90° boundary of the CEM (x_{CES} and z_{CES} are the local position coordinates of the electron at the calorimeter wedge, extrapolated from the CTC track). It also rejects the outermost two towers in the "chimney" wedge[2], and rejects the outermost tower ($|\eta| \sim 1.0$) in other wedges.

Fiducial requirements are also imposed on the CTC. The extrapolated z position of a track at Super Layer 8 (i.e. at radius 130 cm) has to be less than 150 cm, so that the particle crosses all the super-layers. Also, for good stereo track reconstruction a track is required to have a least 12 stereo hits.

Trigger requirements:

W event candidates in the electron channel must pass the EWA Level-3 trigger and a CEM electron trigger. In the muon channel, events must pass CMX, CMNP or CMUP triggers.

Kinematic requirements:

Kinematic requirements help in selecting the physics process of interest and reducing some of the background. The transverse-energy of the lepton and the missing transverse-energy are required to be above 25 GeV, whereas the associated electron track must have a transverse-momentum of at least 15 GeV. The cut on missing transverse-energy rejects most of the multi-jet background. The

---

[2] The locations of two towers are used for the cryogenic penetration for the magnet. The wedge with the missing towers is called the "chimney" wedge.

kinematics required for this analysis are:

- low transverse-mass: where there is most of the sensitivity to α_2, corresponding to higher $\cos\theta$ values in the W rest-frame.
- high W-boson transverse-momentum: where QCD processes affect most the polarisation of W-bosons.

The challenge in handling the data in these regions come from higher backgrounds (both at low transverse-mass and high transverse-momentum) and a smaller sample of Z events, at high-p_T, to model the detector recoil-response.

Electron identification:

Several electron identification variables are used to separate W and Z electrons from the multi-jet background:

- the ratio E_{had}/E_{EM} of hadron calorimeter energy (summed over the towers behind the electromagnetic cluster) over the electromagnetic energy is a discriminant for electrons, since electromagnetic showers are mostly contained within the EM calorimeter, whereas hadrons typically interact later in depth.
- the position match between the extrapolated-track coordinates at the CES (x_{CES}, z_{CES}) and the shower x, z coordinates[3], measured with the CES. The CES cathode channels, centred on the electron shower, are clustered to determine the shower z position. In the same way, CES anode wires are used to determine the shower x position.

---

[3] A drawing of the local coordinate system of a calorimeter wedge is shown in Chapter 2, Figure 2.5.

- the shower profile compared to test-beam profiles: the distribution of pulse heights within the anode wires and cathode strips can be compared with test-beam profiles. Two quantities (χ^2_{strip} and χ^2_{wire}) measure the consistency between the observed shower and the test-beam electron shower.

- the track isolation: the variable N_{cone} is defined as the total transverse-momentum from tracks of (unconstrained) p_T >1 GeV, that lie in a cone $\Delta R < R_{cone}$ around the electron track and have z_0 within 5 cm of the electron z vertex. ΔR is: $\sqrt{(\Delta\eta)^2 + (\Delta\phi)^2}$. N_{cone} measures the isolation of the electron track candidate, with respect to other charged tracks surrounding it. N_{cone} is also referred to as ISO_R.

Muon identification:
Muons must traverse the central muon system (CMU, $|\eta| < 0.6$) or the central muon extension system (CMX, $|\eta| < 1$). Muon tracks are reconstructed using the drift-chamber time-to-distance relationship in the transverse (ϕ) direction, and charge division in the longitudinal (z) direction. The resolutions are 250 μm in the drift direction and 1.2 mm in z [50, 51]. Track segments consisting of hits in at least three layers are found separately in the $r - \phi$ and $r - z$ planes and combined into three-dimensional track segments ("stubs"). For the track isolation, N_{cone} can be used to enhance the identification of muons versus multi-jet background, but is not used in this analysis.

5.3 Event selection: $W \rightarrow e\nu$ and $Z \rightarrow e^+e^-$

The selection criteria for $W \rightarrow e\nu$ and $Z \rightarrow e^+e^-$ are chosen to isolate a sample of well measured electrons with low background. The Z sample is used to tune the recoil model, as well as to determine the p_T^W spectrum and the electron energy-scale and energy-resolution. It is also used to understand the multi-jet background by looking at events that pass all the selection criteria, but not the opposite-sign charge requirement (called the same-sign, or SS sample). Assuming that multi-jet events populate equally the same-sign and opposite-sign (OS) cases, the SS sample can be used as a background sample.

A W candidate event consists of a central electron (CEM) associated with missing E_T. The electromagnetic cluster is required to have transverse-energy higher than 25 GeV and the associated track to have $p_T > 15$ GeV. The track should also cross all eight super-layers of the CTC and have more than 12 stereo-hits. Candidate electrons are required to be in the fiducial detector region (FIDELE). This requirement removes EM showers which include un-instrumented regions of the detector. To avoid azimuthal cracks, the distance ($|x|$) from the centre of the wedge, measured by the CES, is restricted to be within ±18 cm. To avoid the crack between the east and west halves of the CEM calorimeter, the $|z|$ position is required to be greater than 12 cm. To remove Z events, a search is made for a partner electron in the central (CEM), plug (PEM) or forward (FEM) calorimeter. The partner electron should not have transverse-energy greater than 20 GeV, 15 GeV, 10 GeV in the CEM, PEM, FEM respectively and an invariant-mass, with the primary electron, greater than 60 GeV. Moreover, the event is rejected if the partner electron is pointing to any azimuthal crack or the 90° crack, as this may cause the cluster's energy to be mismeasured and consequently cause the invariant-mass rejection to fail.

For electron ID and the removal of the multi-jet background, the variables listed in the previous section are used: the deposited energy ($E_{had}/E_{em} < 0.1$), the track-match ($\Delta z < 5$ cm), the shower shape ($\chi^2_z < 10$) and the track isolation ($ISO_{0.25} < 1$ GeV). The track-match and the shower profile in the azimuthal (x) view are not considered because they are biased by bremsstrahlung [60]. Figure 5.1 shows the electron identification variables used in this analysis. The distributions of $ISO_{0.25}$, χ^2_z, E_{had}/E_{em} and Δz are plotted for the OS and SS Z candidate samples. The arrow shows the electron ID cut.

The Z sample is selected with the same W selection criteria, except the missing E_T is replaced with a partner high-p_T track, and the Z removal requirements are not applied. Moreover the sample of Z's used for the tuning of the simulation has two CEM electrons, both passing electron ID cuts. This choice removes almost all the multi-jet background. Figure 5.2 shows the $Z \rightarrow ee$ invariant mass: the plot on the left-hand side shows the distribution without electron identification. The plot on the right-hand side shows the distribution with electron identification applied to both electrons. The ratio of background to signal is estimated as 2 to 1392 events using the SS to OS ratio.

The effect of the electron ID cuts on W candidates is shown in Figure 5.3. If the electron is a misidentified jet, it will tend to be back-to-back (or collinear with) the second jet in the event. The track isolation cut excludes many di-jets events, as is clear from the reduction of the spikes at 0 and π. The lower plot in Figure 5.3 shows that the shape of the transverse-mass distribution is sensitive to the electron ID cuts.

Table 5.1 summarises the W event selection. The accepted sample consists of 41,717 W candidates.

5.4 Event selection: $W \rightarrow \mu\nu$ and $Z \rightarrow \mu^+\mu^-$

The signature for a $W \rightarrow \mu\nu$ is a high transverse-momentum muon and a high missing transverse-energy. For the Z sample, two high-p_T muons are required. The event vertex, reconstructed with the VTX, has to be within 60 cm in z from the origin of the detector coordinates. The fiducial requirements on the tracks are

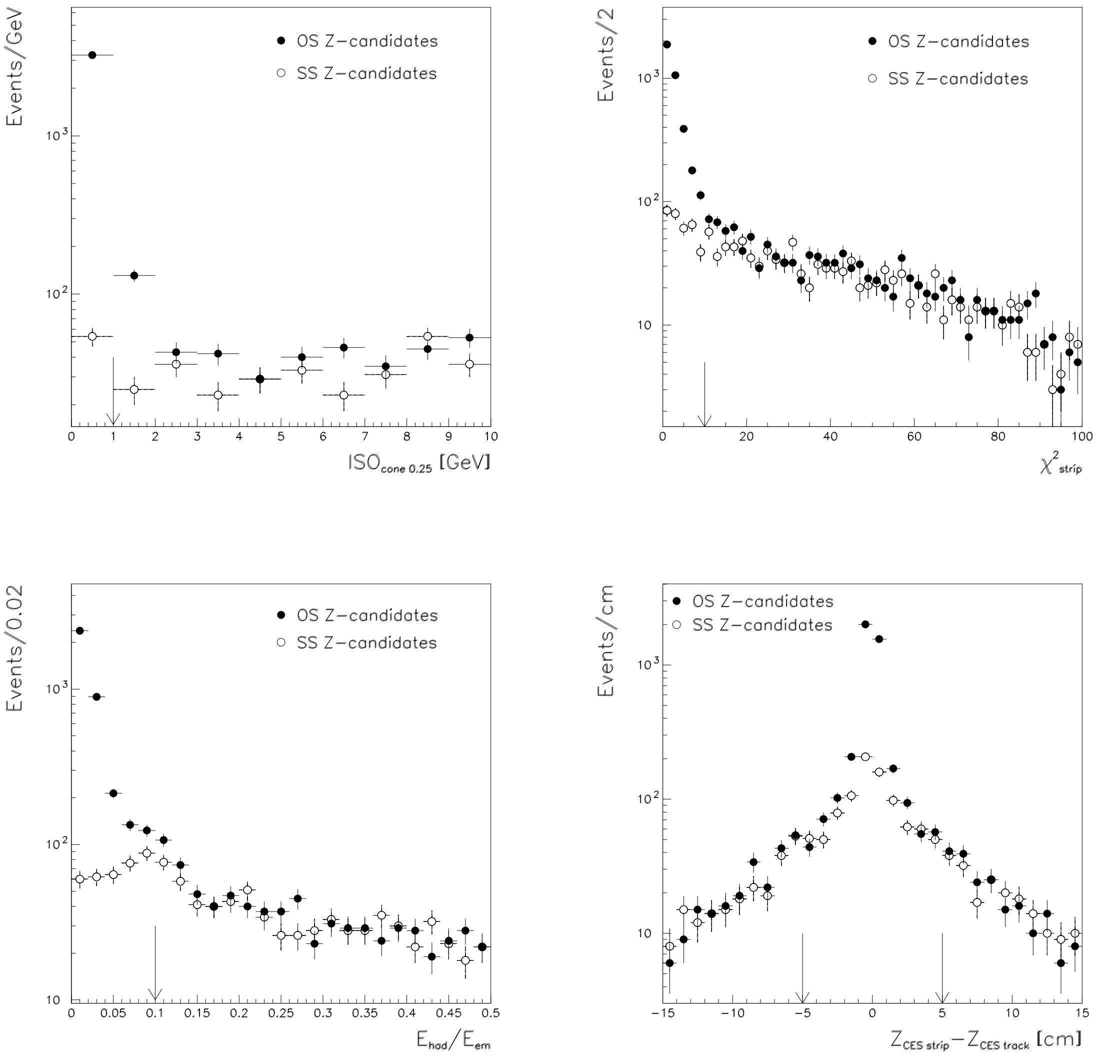

Figure 5.1: *Electron ID variables. From upper-left: cone isolation, shower profile in z view at CES, E_{had}/E_{em} and track match in z at the CES.*

Selection	Class	Status	#pass	%fail
Central electron W sample	-	-	105073	-
No known detector problems	-	ok	101969	2.9
Has luminosity measurement	-	ok	99553	2.4
Pass CEM trigger	trigger	ok	-	-
CDF fiducial FIDELE	fiducial	ok	89500	10.0
vertex in z	fiducial	< 60 cm	na	na
E_T	kinematic	> 25 GeV	83683	6.5
Electron track p_T	kinematic	> 15 GeV	78684	6.0
z of CTC track at SL8	fiducial	< 150 cm	77460	1.5
$\not{E}_T$	kinematic	> 25 GeV	66444	14.2
x location at CES	fiducial	< 18 cm	57279	13.8
z location at CES	fiducial	> 12 cm	56075	2.1
CTC no. of stereo hits on track	fiducial	> 12	52668	6.1
Z removal	background	ok	50472	4.2
Recoil energy	kinematic	< 100 GeV	50422	0.1
Track isolation 0.25 N_{cone}	electron ID	< 1 GeV	44433	11.9
E_{had}/E_{em}	electron ID	< 0.1	44277	0.3
Track-CES match in z view	electron ID	< 5 cm	43895	0.9
χ^2 shower profile in z view	electron ID	< 10	42307	3.6
Transverse-mass	kinematic	50−100 GeV	41717	1.4

Table 5.1: *The set of cuts applied to select the $W \rightarrow e\nu$ data. The column on the right-hand side shows the percentage of events failing each specific cut.*

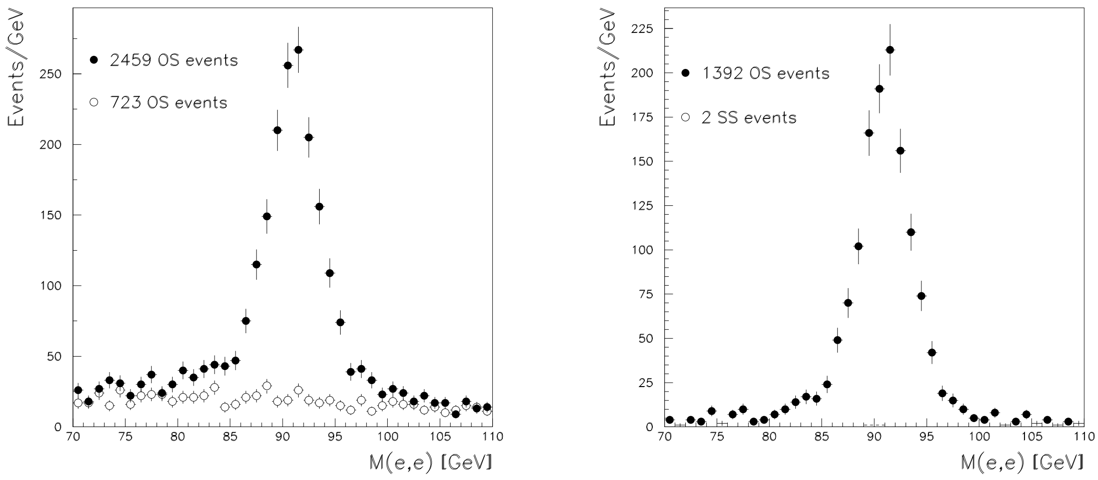

Figure 5.2: *Electron ID cuts on Z sample. No electron ID is applied in the left-hand plot, whereas electron ID is applied to both electrons for the right-hand plot.*

the same as for the electrons. In addition there is a cut on the impact parameter $|d_0| < 0.2$ cm. Moreover the muon "stub" has to match the CTC track within 2 cm (if CMU) or 5 cm (if CMP or CMX). The muon p_T and the missing E_T in the event are required to be higher than 25 GeV, and the deposited energy of the muon in the calorimeters is required to be less than 2 GeV (in the CEM) and 6 GeV (in the CHA). The Z removal (only applied to W candidates) rejects events where there is a second high-p_T (> 10 GeV) track in the CTC, of opposite sign to the μ candidate and back-to-back (within $10°$), that has an invariant-mass with the μ candidate greater than 50 GeV. The track isolation cut has not been applied as it is not particularly efficient.

The list of selection cuts is shown in Table 5.2. The accepted sample consists of 22,235 $W \rightarrow \mu\nu$ candidates.

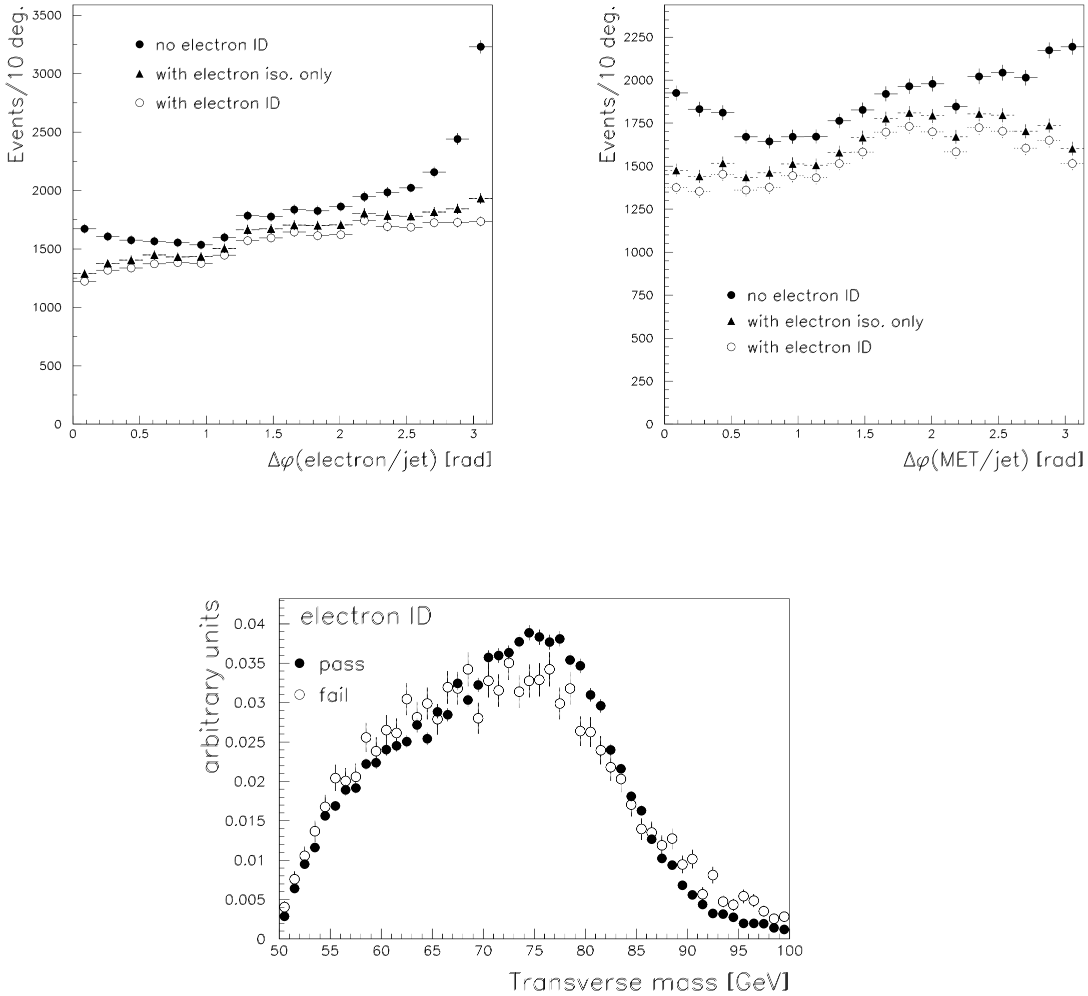

Figure 5.3: *Impact of electron ID on W candidates. Upper: distribution of the opening angle between the leading jet in the event (left) and the* $\vec{\not{E}}_T$ *direction (right). If the electron is a misidentified jet, it will mostly be back-to-back (or collinear with) a jet in the event. Lower: the shape of the transverse-mass distribution of the events that pass, and those that fail, electron ID.*

Selection	Class	Status	#pass	%fail
Muon W sample	-	-	67735	-
No known detector problems	-	ok	64884	4.2
Has luminosity measurement	-	ok	62467	3.7
Muon trigger (CMNP/CMUP/CMX)	trigger	ok	60607	2.9
vertex in z	fiducial	< 60 cm	na	na
z of CTC track at SL8	fiducial	< 150 cm	60210	0.6
Track impact parameter	fiducial	< 0.2 cm	41328	31.3
CTC no. of stereo hits on track	fiducial	> 12	51701	5.8
Energy in CEM and CHA	muon ID	< 2 and 6 GeV	35723	30.9
Anti-cosmics	background	ok	34484	3.5
muon p_T	kinematic	> 25 GeV	29600	14.2
$\not{E}_T$	kinematic	> 25 GeV	25858	12.6
Track match Δ_x (CMU,CMP,CMX)	muon ID	2 cm, 5 cm, 5cm	25575	1.1
Z removal	background	$M_{\mu\mu} < 50$ GeV	22723	11.1
Transverse-mass	kinematic	50$-$100 GeV	22260	2.0
Recoil energy	kinematic	< 70 GeV	22235	0.1
Track isolation 0.4 N_{cone}	*muon ID*	< 2 *GeV*	*21582*	*2.9*

Table 5.2: *The set of cuts applied to select the* $W \rightarrow \mu\nu$ *data. The column on the right-hand side shows the percentage of events failing a specific cut. The track isolation cut, in the last row, is not applied.*

5.5 Corrections applied to the data

Energy and momentum calibration at CDF are described in [21] and references therein. Systematic effects in the central calorimeter energy-scale tend to produce errors of the form $E \to E^{true}(1+\epsilon)$ (independent of charge); CTC internal misalignments tend to produce charge-dependent errors to the sagitta of the form: $1/p_T \to 1/p_T^{true} + q\epsilon'$. The CEM is used to align the CTC by looking at the difference of E/p for positive and negative electrons. On the other hand, the CTC can be used to calibrate the CEM by averaging E/p for positive and negative electrons. The E/p technique consists of adjusting the tower energy response (gain) until the mean E/p (using W-electrons and low-energy electrons) is flat as a function of time and ϕ. It should also agree with the Monte Carlo simulation as a function[4] of η. However, this analysis uses the energy-scale and the resolution determined with the Z mass [21], and checked with the Υ and J/ψ masses. In this way the calibration is not affected by the accurate understanding of the tracking and of the bremsstrahlung process. The price paid is that the Z sample is relatively small compared to the W sample, so the systematic uncertainty can be higher than using the E/p method.

After the energy calibration and the wire-position alignment, the corrections applied to the data are the following. A small residual dependence of the J/ψ mass on cotθ is corrected in the data with:

$$\cot\theta \to 1.0004 \cdot \cot\theta. \tag{5.7}$$

An azimuthally(ϕ)-modulated charge difference in $< E/p >$ is removed with:

---

[4] The material traversed by electrons increases with $|\eta|$, resulting in increased bremmstrahlung loss, and causing the average E/p to increase with $|\eta|$.

$$\frac{q}{p_T^{BC}} \rightarrow \frac{q}{p_T^{BC}} - 0.00031 \cdot \sin(\phi_0 - 3.0), \tag{5.8}$$

where p_T^{BC} is the beam-constraint lepton momentum and q is the electric charge. The magnetic field misalignment is removed with the correction:

$$\frac{1}{p_T^{BC}} \rightarrow \frac{1}{p_T^{BC}} \cdot (1 - 0.0017\ \cot\theta \cdot \sin(\phi_0 - 1.9)). \tag{5.9}$$

An energy non-linearity correction is also included to account for the shift of the energy-scale at the average E_T of the Z electrons, versus the scale at the average E_T of W electrons (about 4.5 GeV lower). This correction is described in Chapter 6.

Chapter 6

The Simulation of W Production and Decay and the Detector Response

A fast Monte Carlo generator with a parametrised detector response has been used to simulate W events. The lepton angular distribution, the W transverse-momentum and the calorimeters' response to the W recoil have been specifically tuned for this analysis. This chapter describes the simulation of W events and presents comparisons with the data.

6.1 Outline of the Monte Carlo

A fast Monte Carlo generator and a parametrisation of the detector response have been used to simulate W events at CDF. The event generator is based on first-order Drell-Yan decay from Berends and Kleiss [61] for the process $W \rightarrow lepton + neutrino + photons$ [62, 63, 64]. The W events are generated according to a relativistic Breit-Wigner distribution from a tree-level diagram of quark-antiquark annihilation (therefore p_T^W=0). The distribution of momenta of the quarks is based on the set MRS-R2 [81] of parton distribution functions (PDF's). The generated W-boson is then Lorentz-boosted, in the centre-of-mass frame of the quark-antiquark pair, with a transverse-momentum p_T^W. The p_T^W spectrum is derived from $Z \rightarrow ee$ and $Z \rightarrow \mu\mu$ data, using the theoretical prediction of the ratio of Z to W p_T spectra, as a function of the rapidity of the vector boson. The way the W p_T spectrum is observed is by the reconstruction of the particles recoiling against the W. Three crucial parts of the simulation have been specifically tuned for this analysis:

- the lepton angular distribution
- the W-boson transverse-momentum
- the detector response to the recoil against the W

The sketch shown in Figure 6.1 is a diagram of the simulation software. Moreover, the calorimeters' resolution and energy-scale and the tracking resolution are tuned to reproduce Z data.

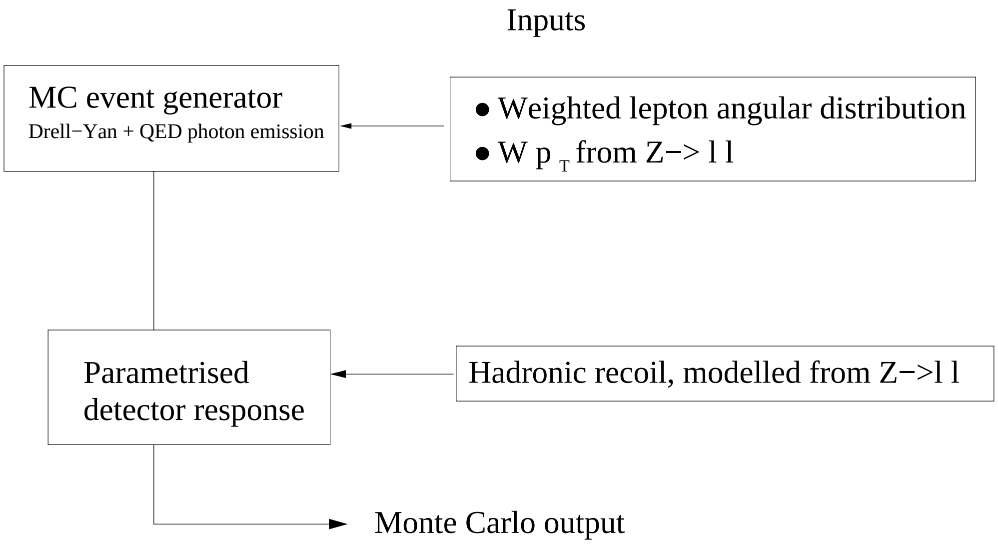

Figure 6.1: *Sketch of the components of the Monte Carlo simulation used in this analysis.*

6.2 The lepton angular distribution from W decays

The standard version of the Monte Carlo produces leptons from W decays distributed with the purely V−A angular spectrum:

$$\frac{\mathrm{d}\sigma}{\mathrm{d}\cos\theta} \propto (1 - P_W \cdot Q \cdot \cos\theta)^2, \tag{6.1}$$

where P_W is the W-polarisation sign, Q is the lepton charge and θ is the lepton polar-angle in the parton frame. The angular distribution of Equation 6.1 gets slightly altered, due to final state photon emission (FSR). However, for small distortions of the spectrum, the lepton angular distribution is approximately expressed by:

$$\frac{\mathrm{d}\sigma}{\mathrm{d}\cos\theta} \propto (1 - P_W \cdot Q\cos\theta)^2 \cdot f_{FSR}(\theta). \tag{6.2}$$

To implement QCD corrections to the angular distribution, the events are weighted first with $1/(1 - P_W \cdot Q \cdot \cos\theta)^2$ and then multiplied by the appropriate weighting factor w_{QCD}. Figure 6.2 shows the weighting procedure of the angular distribution step-by-step. The upper-left plot shows the initial pure V−A lepton angular distribution. The sea-quark contribution is evident at $|\cos\theta|$ close to 1, where the valence-quark contribution is null. The un-weighted distribution is flat, as seen in Figure 6.2 (upper-right). The un-weighting function, inverse of Equation 6.1, has a pole at $\cos\theta = \pm 1$, which requires imposing a cut at $\cos\theta$ close to 1. However, acceptance cuts limit the detected sample to much lower $|\cos\theta|$, around 0.8 (Figure 6.2 (lower plots)).

Weight factor for QCD:

The weight factor that includes QCD corrections (w_{QCD}), is usually expressed as a function of the lepton angles (θ_{CS}, ϕ_{CS}) in the Collins-Soper W-boson rest-frame. Because it is an event-weighting procedure, it does not correspond to including QCD processes into the Monte Carlo. The large-p_T events still have to be introduced by hand, by imposing a transverse-momentum distribution. The w_{QCD} factor is:

$$\begin{aligned} w_{QCD}(\theta_{CS}) &= 1 + \cos^2\theta_{CS} + \frac{1}{2}A_0(1 - 3\cos^2\theta_{CS}) \\ &\pm P_W \cdot Q \cdot A_4\cos\theta_{CS} + \frac{1}{2}A_2\sin^2\theta_{CS} \cdot \cos 2\phi \\ &+ A_3\sin\theta_{CS}\cos\phi_{CS}. \end{aligned} \tag{6.3}$$

The parameters α_1 and α_2 are related to A_0 and A_4 by:

$$A_0 = 2\left(\frac{1-\alpha_2}{\alpha_2 + 3}\right) \qquad A_4 = \alpha_1(1 + A_0/2).$$

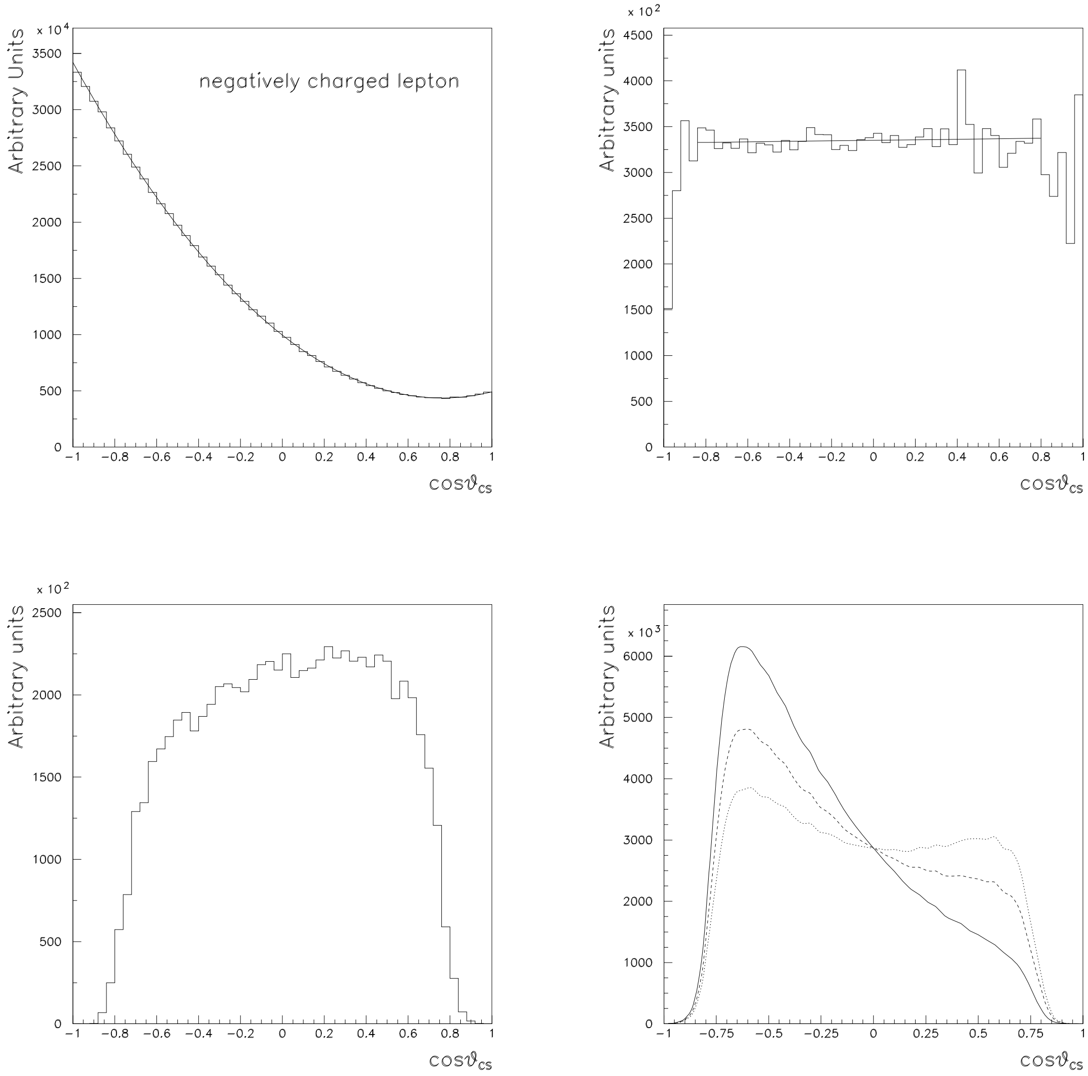

Figure 6.2: *For negative leptons. Upper-left: angular distribution in the W rest-frame. The distribution is V−A including a sea-quark component. Upper-right: Homogeneous polar-angle distribution for* $\cos\theta_{CS}$ *after weighting with* $1/(1-P_W \cdot Q \cdot \cos\theta)^2$. *Lower-left: When acceptance cuts are applied,* $|\cos\theta|$ *is limited at about 0.8 and a homogeneous distribution in* θ *becomes asymmetric as a result of the W charge asymmetry and acceptance cuts. Lower-right: After imposing QCD weight. Continuous line is* $\alpha_1 = 2$, *dashed line is* $\alpha_1 = 1$ *and dotted line is* $\alpha_1 = 0$.

Equation 6.3 corresponds to the QCD angular distribution given in the first chapter, except for the terms with $A_{1,5,6,7}$, which are missing here. They are set to zero, corresponding to the Standard Model expectation over the accessible p_T^W range. A_2 and A_3 are also set to their SM value, and are non-zero functions of p_T^W. They are kept in the distribution even though they should cancel when integrating over ϕ_{CS}. A_2 and A_3 are also considered in the evaluation of the systematic error.

Figure 6.2 (lower-right) shows the QCD-modified lepton angular distribution with different values of α_1.

Treating α_1 and α_2 in the fits:

The ± sign in front of α_1 in Equation 6.3 can lead to negative weights for w_{QCD} if α_2 and α_1 are varied independently. In the QPM approximation, the lowest bound for the weight is zero, which means a vanishing cross-section at $\theta_{CS} = \pm\pi$. It also means that the values of α_2 and α_1 are related to each other so that:

$$(1 + \alpha_2 \cos^2 \theta_{CS} \pm \alpha_1 \cos \theta_{CS}) \geq 0. \tag{6.4}$$

Figure 1.7 (lower-left) in the first chapter showed the relationship between α_1 and α_2 and the allowed parameter space. When varying α_2, the value of α_1 cannot be left to the QPM value of 2, as the expression in Equation 6.4 becomes negative. Moreover, α_1 cannot be set to zero when measuring inclusive charge distributions, because the integration over the accepted phase space introduces a small residual α_1 dependence. By setting $\alpha_1 = 2\sqrt{\alpha_2}$, the expression 6.4 is positive whichever the value of α_2. This prevents assigning negative weights in the region around the QPM point, in the α_1 vs. α_2 parameter space. $\alpha_1 = 2\sqrt{\alpha_2}$ is a good approximation to the SM for $p_T^W \leq 40$ GeV [36]. For $p_T^W > 40$ GeV, α_1 is set to the full SM prediction. The impact of α_1 on α_2 is discussed also in the estimate of the systematic error in Chapter 8.

6.3 Tuning the detector response simulation

6.3.1 Electron energy-scale in the simulation

The electron energy-scale is the overall calibration of the calorimeter response. The energy-scale in the data is set by using the peak of the observed Z mass distribution. This is checked by fitting the distribution of invariant-mass, from the two "tight" central-central electrons Z sample, to a set of MC templates in which the mass of the Z-boson has been varied between 90.9 and 91.4 GeV in 0.025 GeV steps. The "tight" central-central Z is the sample with both electrons in the CEM passing electron ID selection cuts. There are 1392 events in the sample. The central-central Z sample is chosen because CEM electrons only are used in the W sample. Also two "tight" electrons is a convenient choice because of the low background contamination, since there are no events in the same-sign sample. A binned-likelihood technique is used to fit the distribution of invariant-mass. Events are divided in 1 GeV bins, between 70 and 110 GeV. The fit is shown in Figure 6.3 and the result of the fit is a scale-factor:

$$S_E(Z) = \frac{M_Z^{PDG}}{M_Z^{CDF}} = 1.0002 \pm 0.0009. \tag{6.5}$$

Therefore the data and the MC are already sufficiently well tuned to reproduce the world-average [2].

6.3.2 Electron resolution

The energy-resolution of the CEM is parametrised by the formula:

$$\frac{\sigma_E}{E} = \frac{13.5\%}{\sqrt{E_T}} \oplus \kappa \tag{6.6}$$

The first term is a stochastic contribution, determined by test-beam; the κ term accounts for residual gain variations not corrected by the calibration procedure;

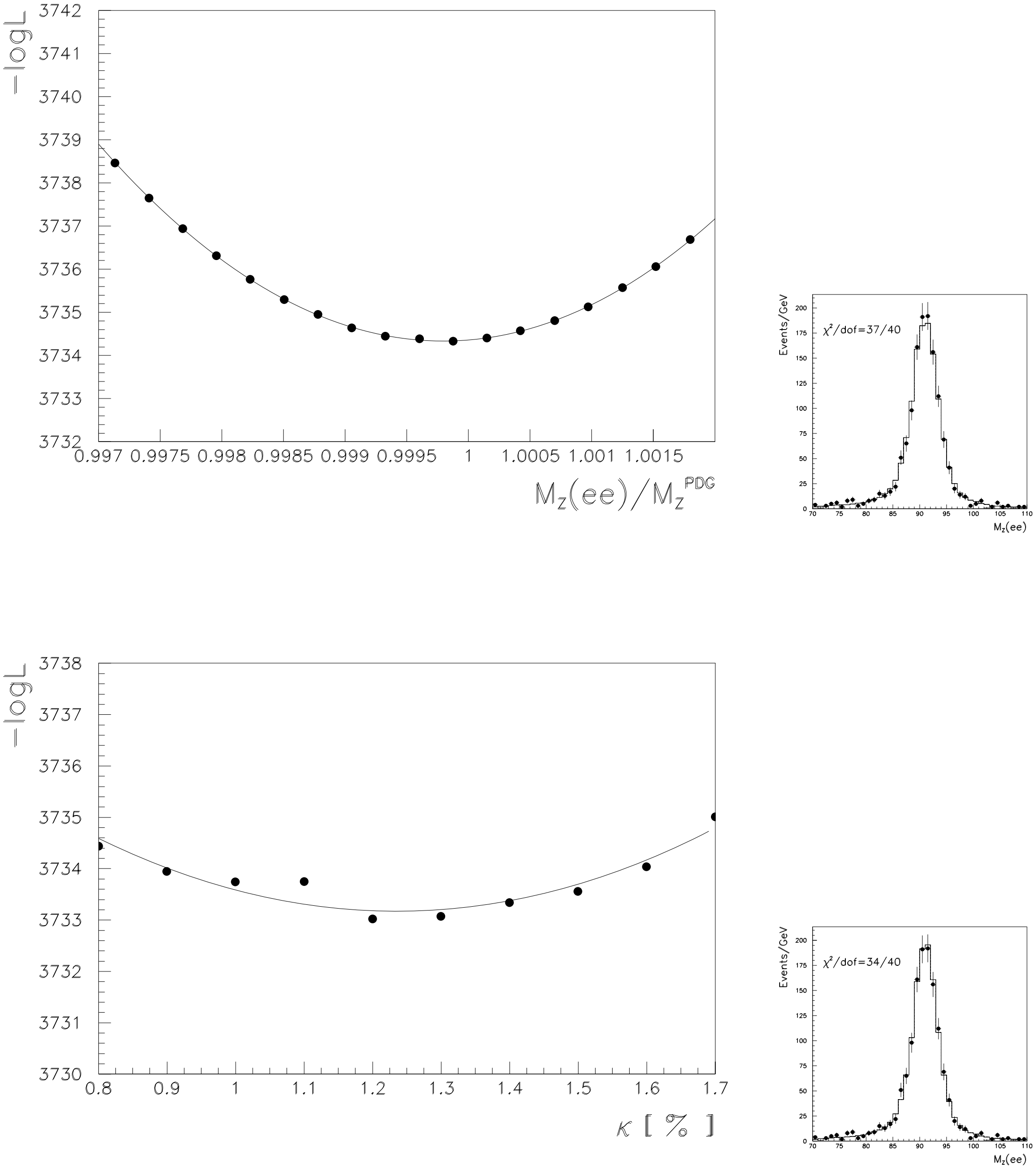

Figure 6.3: *Tuning of the CEM energy-scale and resolution in the Monte Carlo by fitting $M_Z(ee)$. Upper: energy-scale. Lower: resolution constant term κ. The plots on the side are the best-fit distributions.*

the $\oplus$ indicates sum in quadrature. The Monte Carlo has been tuned with the best value of κ to reproduce the $Z \to ee$ mass-peak. The electron resolution term κ and the electron energy-scale can be fitted separately since they are largely uncorrelated [68]. The sample used is the two CEM electrons "tight" Z sample, and the best fit (shown in Figure 6.3) is:

$$\kappa = (1.23 \pm 0.26)\%. \tag{6.7}$$

This value is about 1 σ lower than in [68]. This is due to the electron ID cuts, in particular to the electron isolation method used. Using N_{3D} (see Chapter 5) instead, the best fit for the resolution parameter κ would be 1.49, in agreement with [68], which uses N_{3D} cuts. The energy-scale is also moderately dependent on the electron isolation method, as it was observed already in [65]. The measured scale with N_{3D} would be 1.0006, again in better agreement with [68]. However, the statistical error on the energy-scale is ± 0.0009 and the resolution parameter is only 1σ off, so the correlation with the electron-isolation method is not considered to be too relevant and this effect is considered in the systematic error estimate.

6.3.3 Energy non-linearity correction

The energy-scale set with the $Z \to ee$ sample is valid only if there is linearity between the energy-scale at the Z pole and the one at typical W energies. The average E_T for Z electrons is about 4.5 GeV higher than the E_T for W decay. The non-linearity over a small range of energies can be expressed with a slope as:

$$S_E(W) = S_E(Z) \cdot \left[1 + \xi \Delta E_T\right], \tag{6.8}$$

where $S_E(Z)$ is the measured scale at the Z pole, ξ is the non-linearity factor and ΔE_T is the difference in the average E_T between Z and W electrons. To estimate ξ, the following procedure is applied: the E/p distributions from the data, between 0.9 and 1.1, are compared with the Monte Carlo in separate regions of E_T. The difference between the mean of the data plot and that of the simulation plot is calculated for each E_T range. Such differences are then plotted versus E_T. The E_T dependence in the plot is related to a non-linearity in the energy-scale. Figure 6.4 shows the E/p peaks using W electrons with E_T in 5 GeV-wide ranges, between 25 and 60 GeV. Figure 6.4, lower-right, shows the differences using Z and W electrons. The slope of the linear fit to the differences of the mean $< E/p >$ is $(2.0 \pm 0.4) \cdot 10^{-4}$ GeV^{-1}. This slope measures: $\mathrm{d} < E/p > /\mathrm{d}E_T$. There is a linear relationship between the mean of the E/p distribution around the peak, evaluated in the interval $0.9 - 1.1$, and the energy-scale. The relationship is determined when setting the energy-scale with the E/p method [65], and is such that[1]:

$$\frac{\mathrm{d} < E/p >}{\mathrm{d}E_T} = -0.73 \frac{\mathrm{d}S_E}{\mathrm{d}E_T}. \tag{6.9}$$

The sign indicates that the reduction of the scale is required to compensate an increase in the observed energy. Using Equation 6.9, the slope in $< E/p >$ can be transformed into a slope in S_E, and the result for the non-linearity factor ξ is:

$$\xi = \frac{1}{S_E(Z)} \frac{\mathrm{d}S_E}{\mathrm{d}E_T} = \frac{1}{-0.73 \cdot S_E(Z)} \frac{\mathrm{d} < E/p >}{\mathrm{d}E_T} = -0.00027 \pm 0.00005(\mathrm{stat})\ \mathrm{GeV}^{-1}. \tag{6.10}$$

The error comes from the fit only. Therefore the electron E_T in the data has to be corrected as:

$$E_T \rightarrow E_T \times (1 - 0.00027 \cdot (E_T - 42.73)). \tag{6.11}$$

After the correction, no residual slope remained in the difference of the mean $< E/p >$ between data and Monte Carlo.

---

[1] The coefficient is less than 1 because the correspondence is made with the mean evaluated in a interval rather than the peak position.

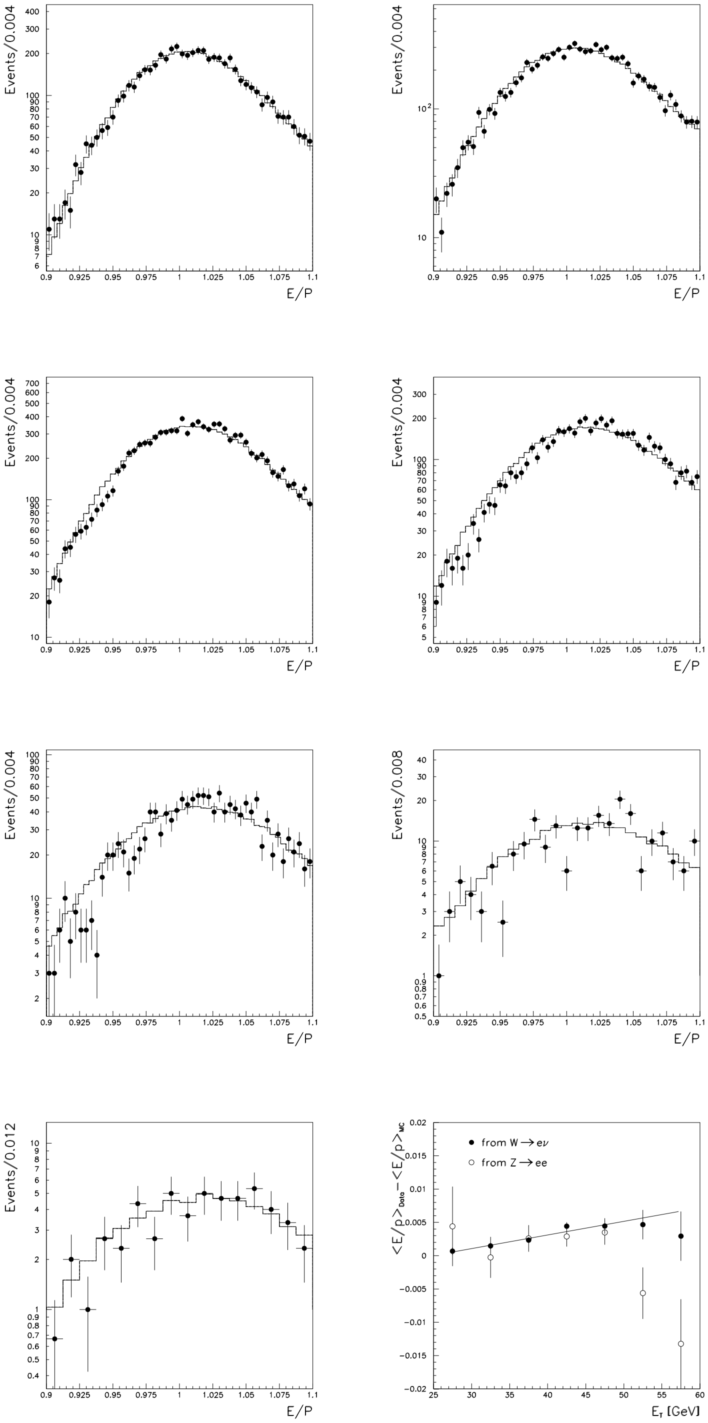

Figure 6.4: *E/p distributions between 0.9 and 1.1 from $W \to e\nu$. Each plot is a 5 GeV-wide E_T region, between 25 and 60 GeV. The filled circles are the data, the histogram is the Monte Carlo. Lower-right: the fit for the non-linearity term using the W data (filled circles). The same procedure is repeated with Z data and the result is shown by the open circles*

6.3.4 Tracking resolution and momentum-scale

A sample of $Z \to \mu\mu$ events is used to determine the momentum-scale, by normalising the reconstructed $Z \to \mu\mu$ mass to the world-average mass [2], and to measure the momentum resolution in the high-p_T region. The $Z \to \mu\mu$ Monte Carlo events are generated at various values of the Z mass, in analogy with what done for the electron energy-scale. The determined momentum-scale factor is:

$$\frac{M_Z^{PDG}}{M_Z^{CDF}} = 1.0008 \pm 0.0011, \tag{6.12}$$

and the momentum resolution:

$$\sigma(1/p_T) = (0.097 \pm 0.005) \times 10^{-2}\ \text{GeV}^{-1}. \tag{6.13}$$

6.4 Z transverse-momentum spectrum

The transverse-momentum of W-bosons is not a measurable quantity because the final state is not reconstructed completely. Instead, the W p_T spectrum is modelled by measuring the transverse-momentum of Z's and using theoretical arguments to derive p_T^W. The rapidity dependence of the p_T distribution is also taken into account by weighting according to the rapidity of the boson. The Z sample used is the two central electrons sample, (the CEM-CEM "tight" sample). The $Z \to \mu\mu$ data sample is also used.

The Z p_T distribution is generated in the Monte Carlo using the following *ad-hoc* four-parameter functional form:

$$f(p_T) = \frac{x^{P_4}}{\Gamma(P_4+1)} \left[(1-P_1)P_2^{P_4+1}e^{-P_2 x} + P_1 P_3^{P_4+1}e^{-P_3 x}\right]; \quad x = p_T/50.0\ \text{GeV}. \tag{6.14}$$

To determine the parameters $P_{1,..,4}$, the observed p_T^Z spectrum is fitted first with the functional form of Equation 6.14. Figure 6.5 shows the fits to the Z-boson transverse-momentum distribution from $Z \to \mu\mu$ and $Z \to ee$.

The functional dependence $f(p_T)$ measured in this way is a function of the *reconstructed* Z-boson transverse-momentum. To turn it into a distribution function of the *generated* p_T^Z spectrum, the fit is corrected using the ratio from the simulation of the p_T^Z generated to the p_T^Z reconstructed. This is possible since the difference between the generated spectrum and the observed p_T^Z distribution is very small. Technically a histogram is generated from the best fit to the Z events and it is then weighted bin by bin with the ratio MC(gen)/MC(recon) of the p_T^Z distribution. The outcome is fitted again to give the final set of parameters, listed in Table 6.1. The distribution from the muon channel is chosen to be used in the simulations of W events, and the results from the e and μ channels are compared to evaluate the systematic error.

	e channel	μ channel
P_1 :	0.83±0.02	0.77±0.04
P_2 :	2.92±0.33	2.99±0.33
P_3 :	10.93±0.79	9.23±0.79
P_4 :	0.75±0.07	0.50±0.06

Table 6.1: *The parameters of the p_T^Z distribution obtained from $Z \to ee$ and $Z \to \mu\mu$ data.*

The plots in Figure 6.6 show a comparison of the $Z \to \mu\mu$ data with the simulation of the p_T^Z distribution. Linear and logarithmic scales are shown to visualise the peak and the tail of the distribution. The fitted parameters lead to a good description of the data. Figure 6.7 show a comparison of the $Z \to ee$ data with the simulation. The input p_T^Z is taken from $Z \to \mu\mu$ and there is a good agreement between data and MC.

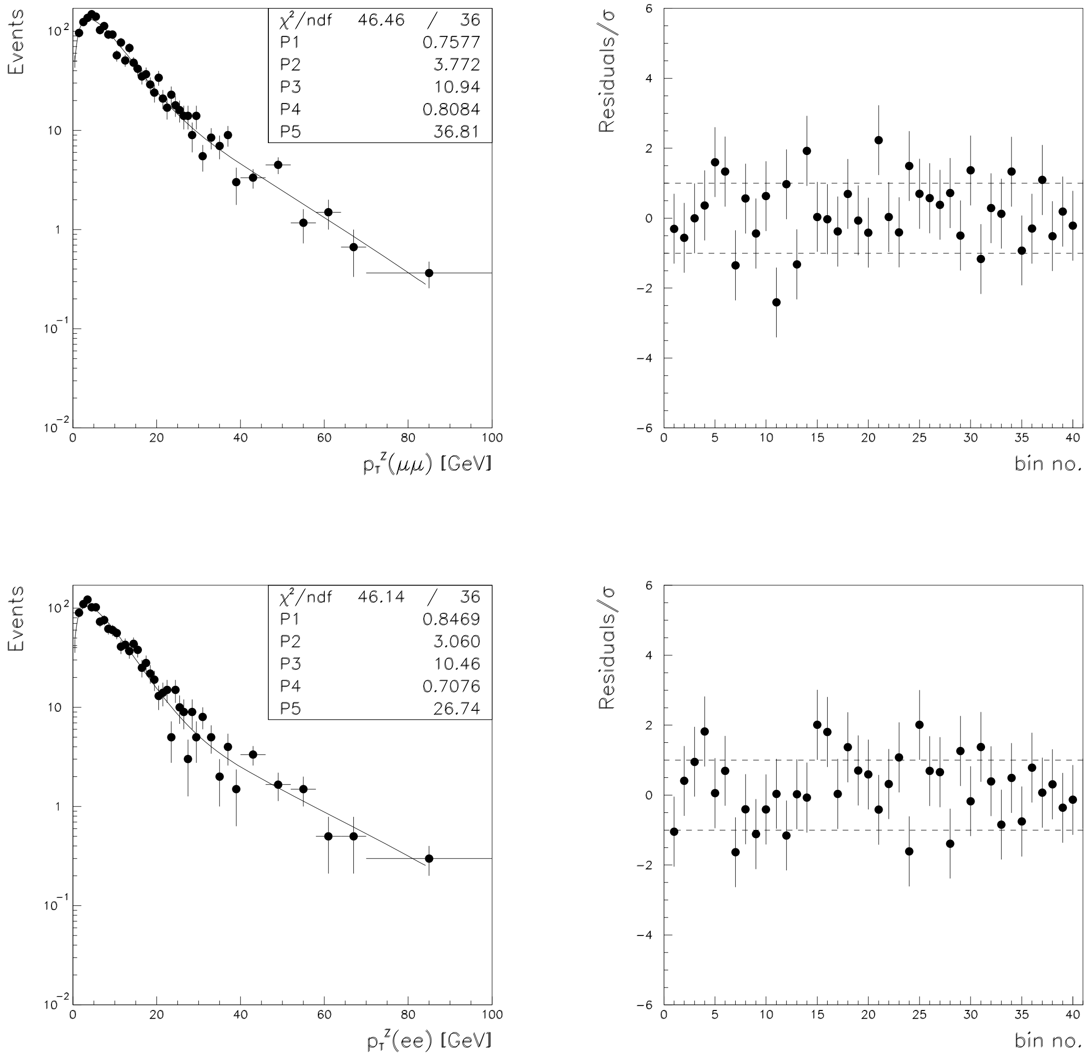

Figure 6.5: *Upper plots: Best fit to the transverse-momentum distribution of Z→ μμ. Lower plots: Best fit to the transverse-momentum distribution of Z→ ee. The plots on the right-hand side show the distribution of the residuals normalised by the error in each bin.*

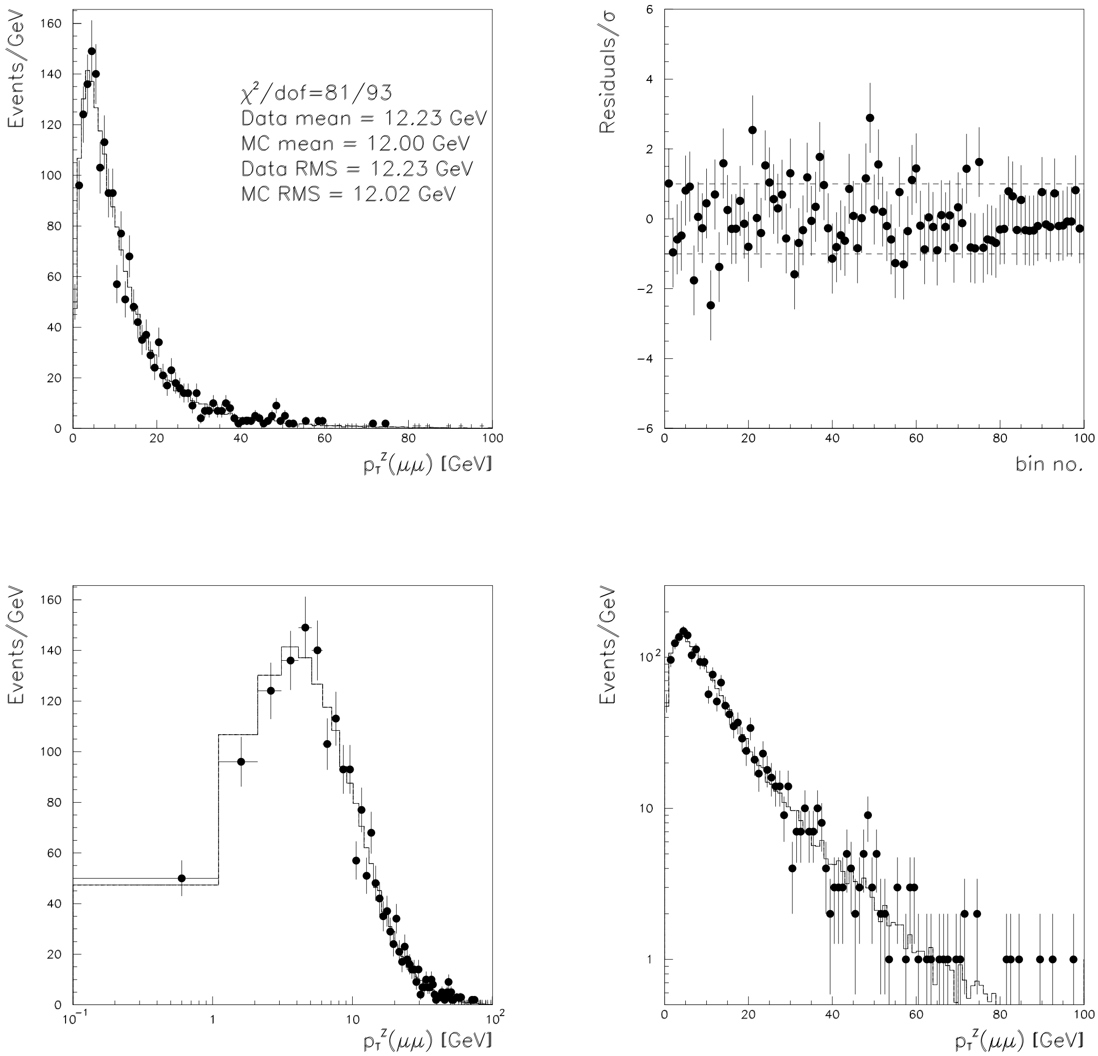

Figure 6.6: *p_T^Z distribution from $Z \to \mu\mu$ data compared with the simulation. Upper plots show the distribution and the residuals; lower plots show the same distribution in logarithmic scales to view the peak and the tail.*

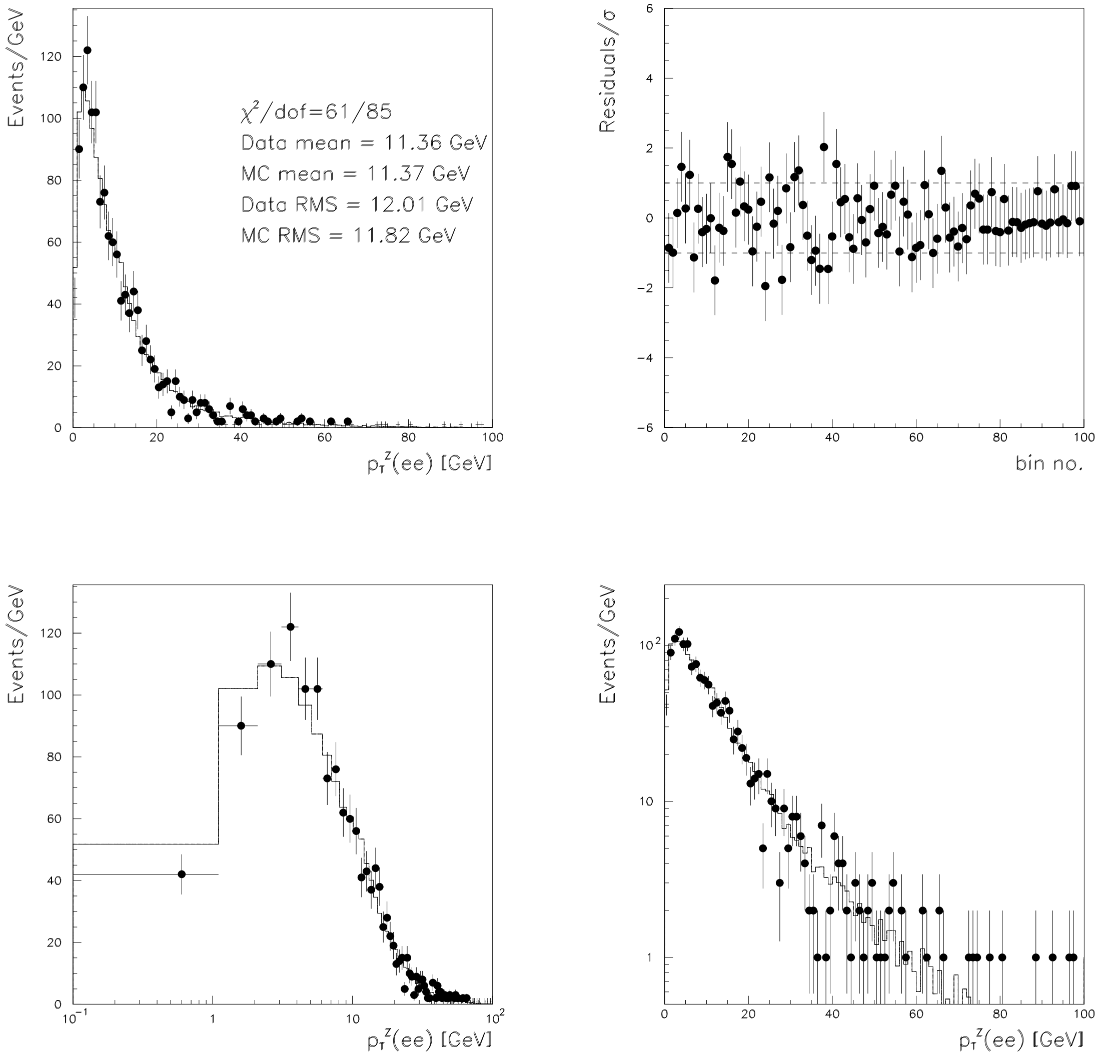

Figure 6.7: *p_T^Z distribution from $Z \to ee$ data compared with the simulation. Upper plots show the distribution and the residuals; lower plots show the same distribution in logarithmic scales to view the peak and the tail.*

6.5 The Z recoil model

A measure of the W boost in the transverse plane comes from the measurement of the calorimeter response to jets and particles recoiling against the W. The modelling of such response to a given W-boson transverse-momentum is called the "recoil model" [66, 67] and it is implemented in the Monte Carlo simulation of the event. The recoil model is derived using the recoil against Z-bosons, whose kinematics are completely determined by the two leptons. The assumption is made that the recoil against $Z \to l^+l^-$ can be extended to model W events, since the W and Z share a common production mechanism and are close in mass.

The model:

The outline of the recoil model is the following: a vector $\mathbf{u}$ is defined as the calorimeter recoil vector and the distributions of its components are fitted with a model based on the response and resolution. The recoil is decomposed into two vectors: one (u_1) along the direction of $\mathbf{p}_T^Z$ and the other (u_2) perpendicular to $\mathbf{p}_T^Z$. It is expected in general that for a given $\mathbf{p}_T^Z$, u_1 is a function (the response function) of p_T^Z, with a certain smearing (assumed Gaussian). The component u_2, being perpendicular to $\mathbf{p}_T^Z$, averages to zero, with a smearing that is also assumed to be Gaussian. u_1 and u_2 are therefore parametrised as:

$$\left(\begin{array}{c} u_1 \\ u_2 \end{array} \right) = \left(\begin{array}{c} f(p_T^Z) \\ 0 \end{array} \right) + \left(\begin{array}{c} G_1(\sigma_1) \\ G_2(\sigma_2) \end{array} \right). \tag{6.15}$$

The modulus of $\mathbf{u}$ vector is $u = |\mathbf{u}| = \sqrt{u_1^2 + u_2^2}$. The validity of the Gaussian hypothesis is shown for u_2 in Figure 6.8. It is similarly proved to hold for u_1. The distribution of u_2 is plotted in four sample regions of p_T^Z (0−2 GeV, 8−10 GeV, 18−20 GeV, 35−45 GeV). The distributions are well described by Gaussians.

Response functions:

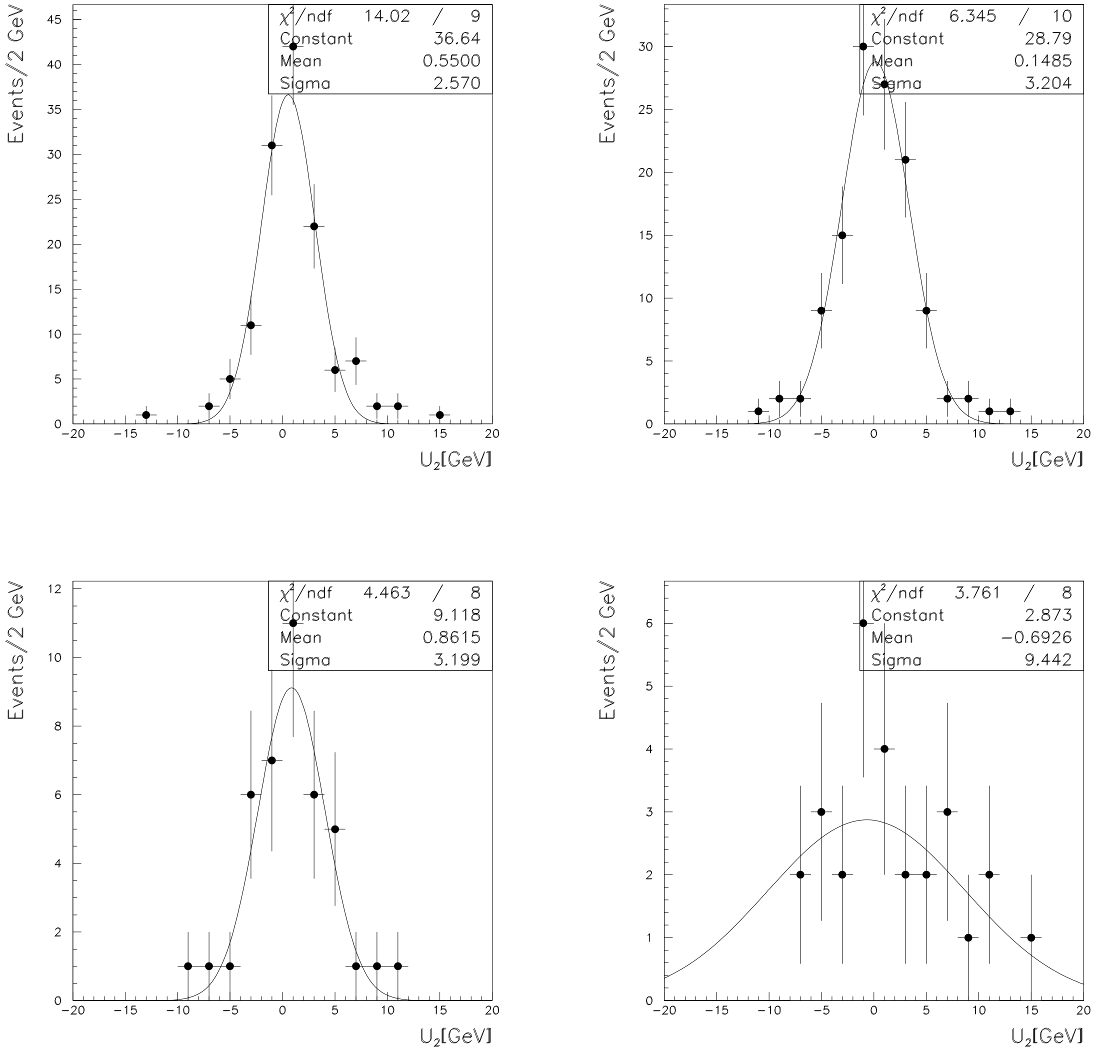

Figure 6.8: *Example of the* u_2 *distributions to check the validity of the Gaussian hypothesis for the resolution. The distribution of* u_2 *is plotted in four ranges of* p_T^Z *(from upper-left moving right: 0–2 GeV, 8–10 GeV, 18–20 GeV, 35–45 GeV).*

The response function $f(p_T^Z)$ is well described by a second order polynomial:

$$f(p_T^{Z(recon)}) = a_0 + a_1 \cdot p_T^{Z(recon)} + a_2 \cdot (p_T^{Z(recon)})^2. \tag{6.16}$$

The fit is done separately for $Z \to ee$ and $Z \to \mu\mu$ and the two functions agree well. The response function 6.16 is corrected for the relationship between the "generated" p_T^Z and the reconstructed p_T^Z. The relationship is with good approximation a quadratic:

$$p_T^{Z(recon)} = c_0 + c_1 p_T^{Z(gen)} + c_2 (p_T^{Z(gen)})^2, \tag{6.17}$$

and c_0, c_1, c_2 are determined from the Monte Carlo and listed in Table 6.2 (throughout $p_T^{Z(recon)}$ is measured in GeV). This is due to resolution effects and taking the modulus of the sum of the two leptons' momentum vectors.

coeff.	e-channel	μ-channel
c_1 :	0.326	0.732
c_2 :	0.974	0.948
c_3 :	0.338E-03	0.825E-03

Table 6.2: *Coefficients for the relation between the "reconstructed" Z-boson transverse-momentum, from lepton reconstruction, and the true (generated) value.*

The response function for u_2 is a constant and it is consistent with zero within the statistical error. The response function for u_2 is thus set to zero in the simulation.

The $\sum E_T$ model:

The $\sum E_T$ model is needed to correctly parametrise the resolutions σ_1 and σ_2. The total energy ($\sum E_T$) per event, seen in the calorimeters, is determined by a contribution from the underlying event and a contribution from the jet activity. In the definition of $\sum E_T$ (see Chapter 5) the energy from the primary electron

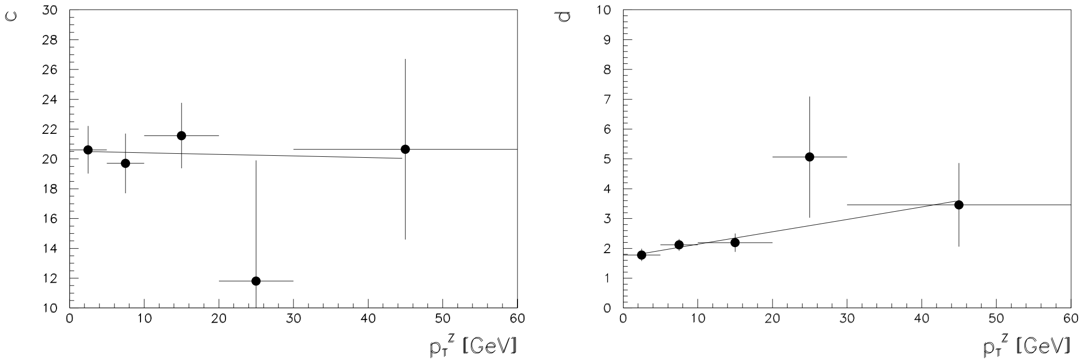

Figure 6.9: *Fits for the coefficients of the* $\sum E_T$ *model.*

is removed. For a given p_T^Z, the $\sum E_T$ distribution is well described by a Gamma function:

$$f_{p_T^Z}(x) = \frac{x^d e^{-x}}{\Gamma(d+1)}, \tag{6.18}$$

where $x = \sum E_T / c$ and c, d are linear functions of p_T^Z. The functions c and d have been fitted to data (see Figure 6.9). The best-fit values are $d = 1.72 + 0.04 \cdot p_T$ and $c = 20.52 - 0.01 \cdot p_T$.

Resolutions:

The resolutions σ_1 and σ_2 depend also on the underlying event and the jet activity. The underlying event can be approximated by minimum bias events, in which $u = 0$, and is measured with a resolution σ_{mbs}. The widths are parametrised in the form:

$$\begin{pmatrix} \sigma_1 \\ \sigma_2 \end{pmatrix} = \sigma_{mbs}(\sum E_T) \cdot \begin{pmatrix} a_1 + a_2 \cdot p_T^Z + a_3 \cdot (p_T^Z)^2 \\ b_1 + b_2 \cdot p_T^Z + b_3 \cdot (p_T^Z)^2 \end{pmatrix}. \tag{6.19}$$

Using minimum bias data, the resolution component σ_{mbs} has been proved to follow a power law [69]:

$$\sigma_{mbs}(\sum E_T) = 0.324 \cdot (\sum E_T)^{0.577}, \tag{6.20}$$

where σ_{mbs} and $\sum E_T$ are calculated in GeV. Therefore, given a p_T^Z, $\sum E_T$ is generated in the simulation according to the distribution in Equation 6.18 σ_{mbs} is calculated according to Equation 6.20.

The explicit p_T^Z dependence is derived from Z data, using both electrons and muons. The u_1 resolution appeared to be slightly different between muons and electrons, so it is listed here separately. The parameters are then corrected for the dependence of $p_T^Z(recon)$ versus $p_T^Z(true)$, as before, and the final parameters are (from fit to electrons):

$$a_1 = 1.04 \pm 0.04 \quad a_2 = (-0.44 \pm 0.23) \cdot 10^{-2} \quad a_3 = (0.12 \pm 0.06) \cdot 10^{-3},$$

and for the muons:

$$a_1 = 0.99 \pm 0.04 \quad a_2 = (0.93 \pm 0.23) \cdot 10^{-2} \quad a_3 = (0.16 \pm 0.06) \cdot 10^{-3}.$$

For the resolution of the u_2 component, the electron and muon channel measurement are averaged since they do not give a significantly different response. The parameters are:

$$b_1 = 1.055 \pm 0.040 \quad b_2 = (-0.22 \pm 0.26) \cdot 10^{-2} \quad b_3 = 0.0.$$

Check of the recoil model with Z events:

The recoil model is checked by comparing the data with a simulation of Z events that uses the parameters derived from the fits. Figure 6.10 shows the dependencies of the recoil vectors versus p_T^Z. $< u_1 >$ should in principle be equal and opposite to p_T^Z, but due to inefficiency in the reconstruction it is not. However, measuring u_1 provides a measure of p_T^Z (or ultimately p_T^W) using these curves. The resolution $\sigma(u_1)$ worsens at higher p_T^Z, due to increased jet-like activity in the event. As expected, u_2 is on average zero. The agreements are good in all the plots and the normalised χ^2's are close to 1. Figures 6.11 and 6.12 show the recoil vector's components (u, u_1, u_2) and $\sum E_T$ for $Z \to ee$. Figures 6.13 and 6.14 show the same distributions for $Z \to \mu\mu$. All the distributions from data are described well by the Monte Carlo.

6.6 The W transverse-momentum distribution

To turn the Z p_T distribution into a W p_T distribution, the simulation applies two weighting functions. The first allows for the fact that the p_T^Z distribution (Equation 6.14) is derived with a fit performed to data averaged over all rapidity values (mean $|y|$=0.3). However, W events need to be generated differential in both p_T and y. This weighting function is taken from a theoretical calculation of $\frac{\mathrm{d}\sigma}{\mathrm{d}p_T}(y = 0.3)/\frac{\mathrm{d}^2\sigma}{\mathrm{d}y\mathrm{d}p_T}(y)$ [21]. The second weighting function turns the p_T^Z distribution, differential in p_T and y, into a distribution for the transverse-momentum of the W-boson. This is obtained from the theoretical calculation of $\left.\frac{\mathrm{d}^2\sigma}{\mathrm{d}y\mathrm{d}p_T}\right|_W / \left.\frac{\mathrm{d}^2\sigma}{\mathrm{d}y\mathrm{d}p_T}\right|_Z$ [76, 77, 78, 79]. Resummed calculations are used for correcting the difference between the W and the Z p_T distributions. The ratio is between 0.9 and 1.0 over the p_T range of interest. Since this is a ratio, the uncertainty is expected to be small because of cancellation of systematics. Indeed, by varying PDF's, α_s or the type of calculation, the resulting uncertainty in W p_T is small in comparison to the uncertainty arising from the statistics of the Z sample used to define the distribution [72, 73, 74, 75].

The comparison of the W-recoil vectors with the simulation is shown in Figures 6.15 (electron channel) and 6.16 (muon channel). In addition to the recoil $\mathbf{u}$, the

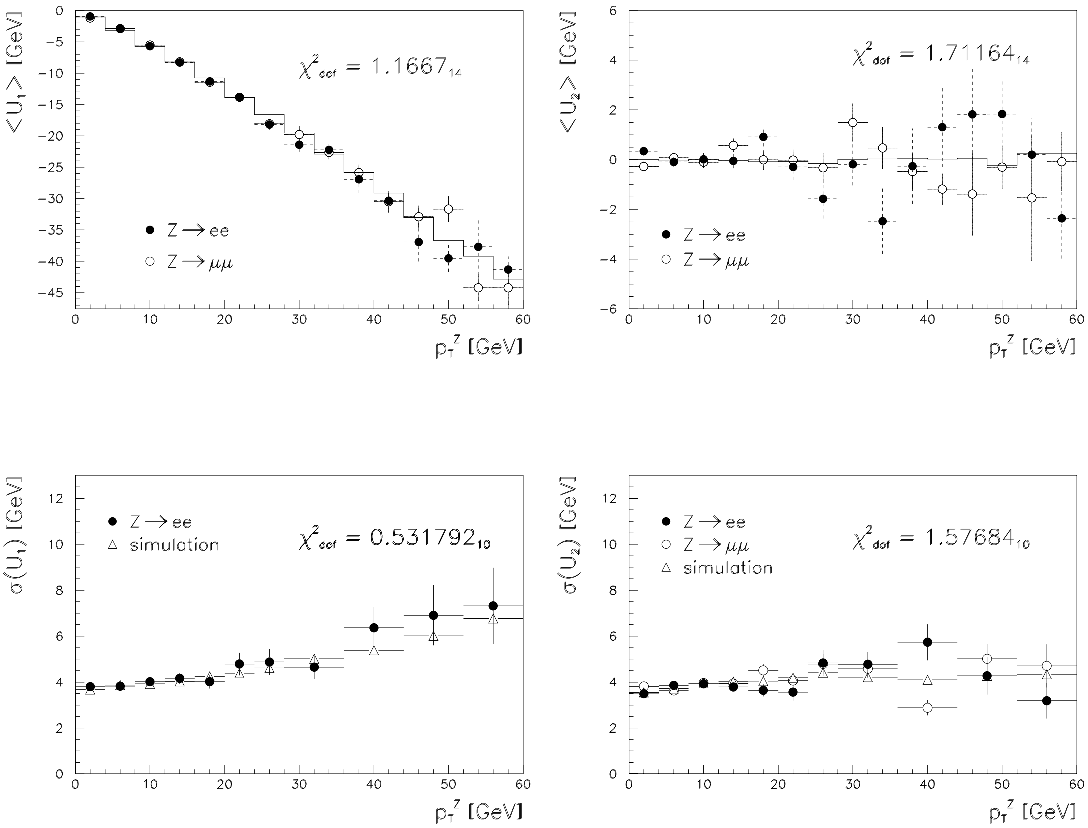

Figure 6.10: *Upper: comparison of the data with the simulation for the recoil response components* u_1 *and* u_2 *versus* p_T^Z. *Lower: the resolutions* $\sigma(u_1)$ *and* $\sigma(u_2)$ *versus* p_T^Z. *The* χ^2 *is shown normalised per degree of freedom.*

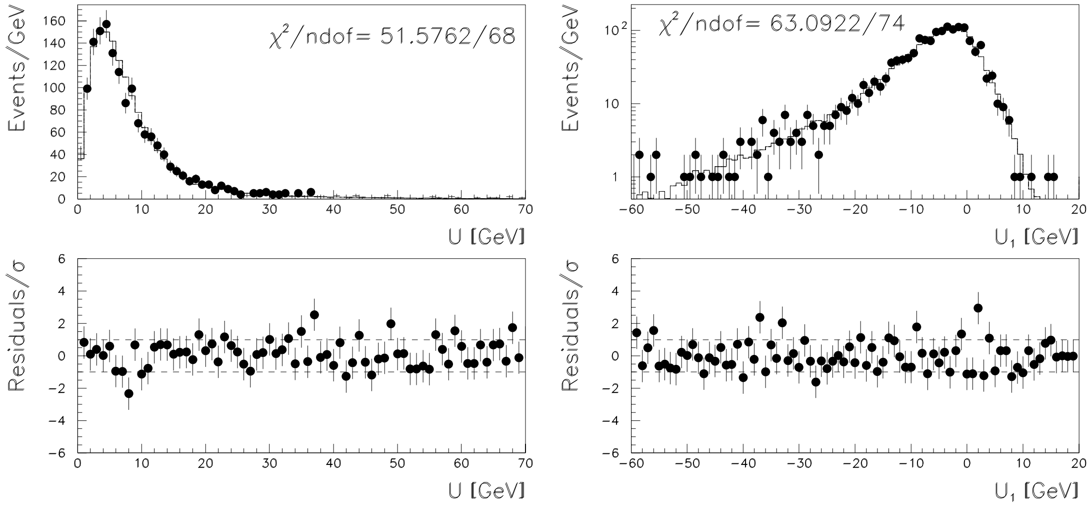

Figure 6.11: *$Z \to ee$: comparison of the data with the simulation for the recoil u and its component u_1.*

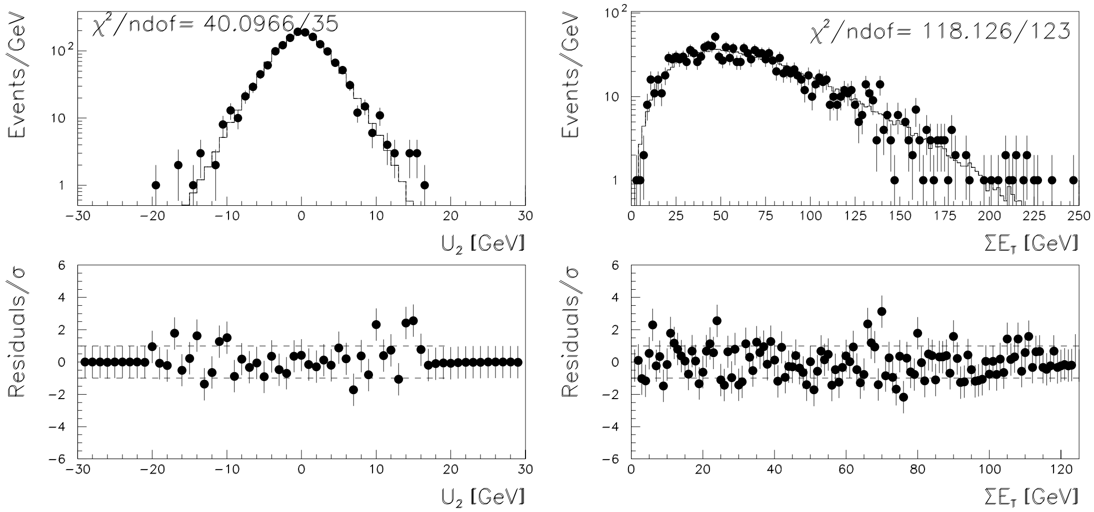

Figure 6.12: *$Z \to ee$: comparison of the data with the simulation for the recoil component u_2 and for $\sum E_T$.*

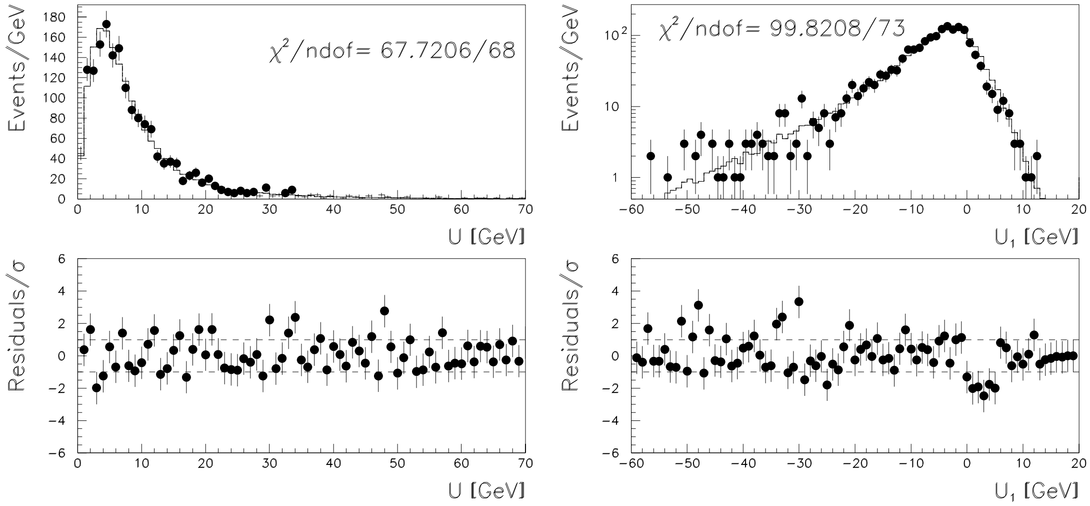

Figure 6.13: $Z \to \mu\mu$: *comparison of the data with the simulation for the recoil* u *and its component* u_1.

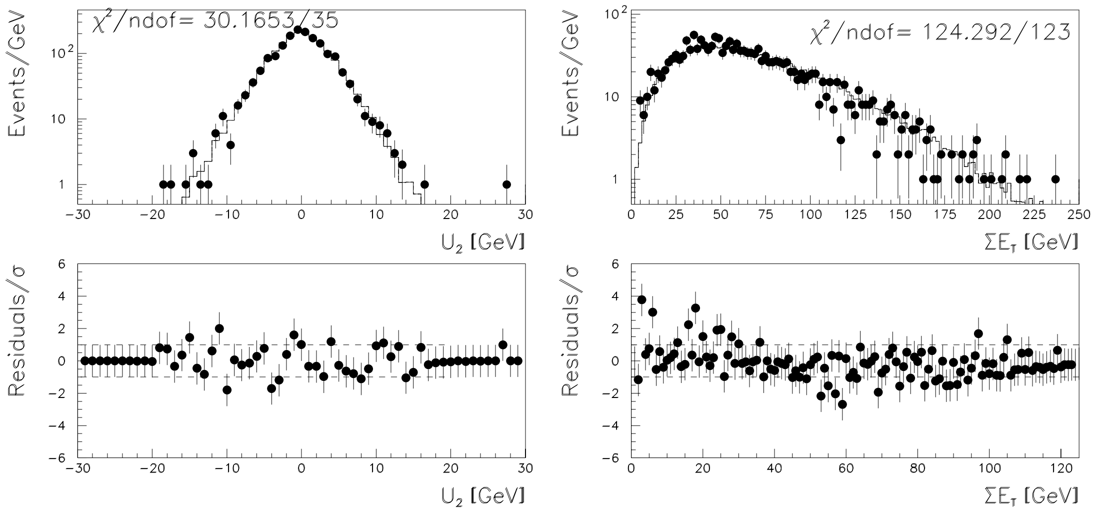

Figure 6.14: $Z \to \mu\mu$: *comparison of the data with the simulation for the recoil component* u_2 *and for* $\sum E_T$.

components u_{par} and u_{perp} (respectively parallel and perpendicular to the lepton direction) are also shown. For W's the projection of u is made along the lepton direction because the W direction is not measured. The agreements are generally good.

6.7 Checking the simulation

Several plots have been presented in the previous sections to show the agreement between simulation and data. The validation of the Monte Carlo is completed here by checking the lepton distributions of pseudorapidity, ϕ angle (in the laboratory-frame) and transverse-momentum.

Electron channel:

Figure 6.17 shows the lepton distributions for the $W \rightarrow e\nu$ channel, upper-left plots shows the η distribution from the data (points) and Monte Carlo (histogram). The mean values, RMS and a χ^2 value are shown on the plot. The upper-right plot shows the ϕ distribution. The peculiar shape of the ϕ distribution is due to the boundaries of the calorimeter towers. The lower-left and right plots show the electron energy distribution and the electron transverse-energy respectively. The τ background, which is the dominant source, has been added to the Monte Carlo. The simulation describes well the data in all the distributions.

Muon channel:

Figure 6.18 shows the muon distributions, in analogy with the electron channel. The upper-left plot is the pseudorapidity distribution; right is the ϕ distribution and lower-left is the muon p_T distribution. Backgrounds from $W \rightarrow \tau\nu$ and $Z \rightarrow \mu\mu$ have been added to the Monte Carlo. The simulation is in good agreement with the data in all distributions.

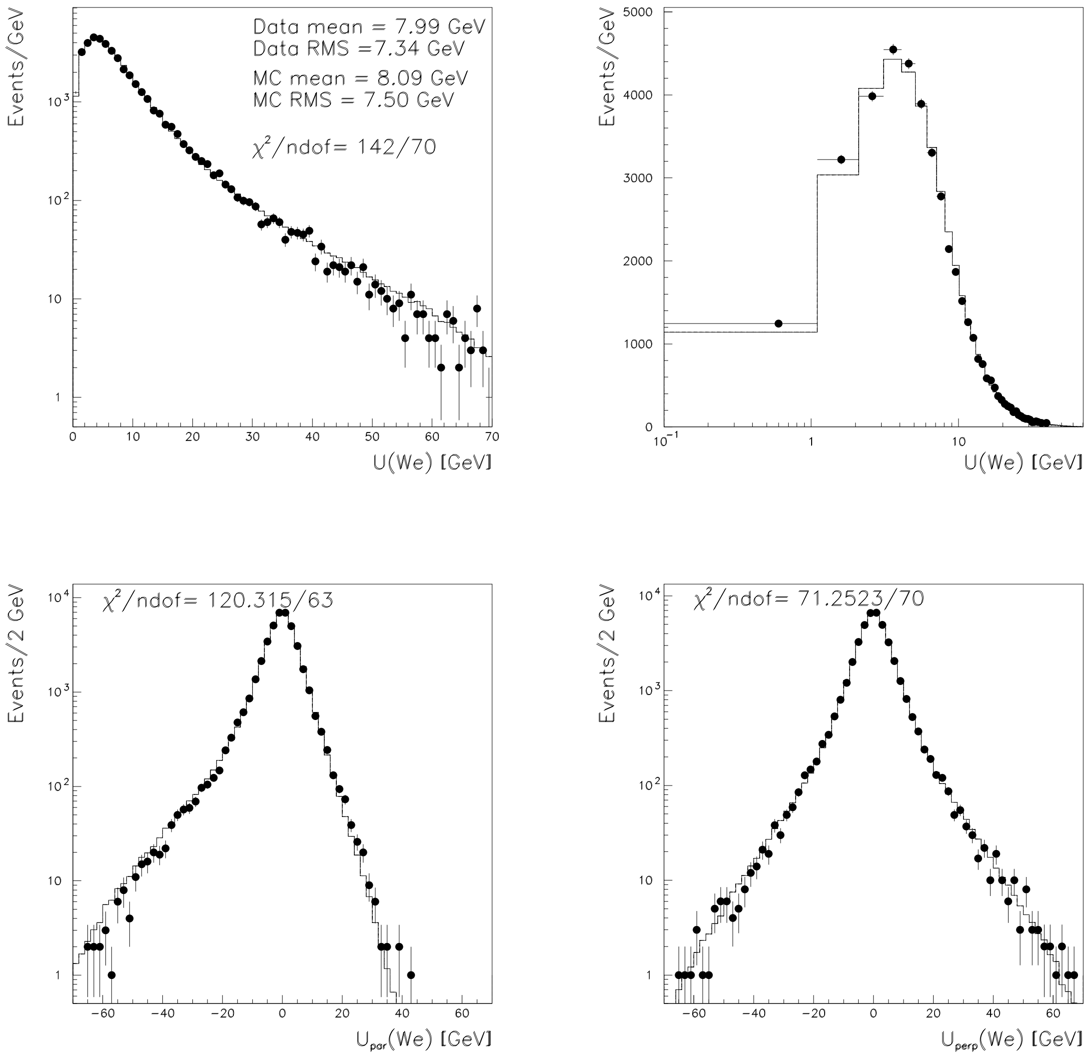

Figure 6.15: $W \to e\nu$. *Upper: the simulation (histogram) of the recoil against the W-boson compared with the data (points). Lower: the components of* $\mathbf{u}$ *parallel and perpendicular to the lepton direction in the data and in the simulation.*

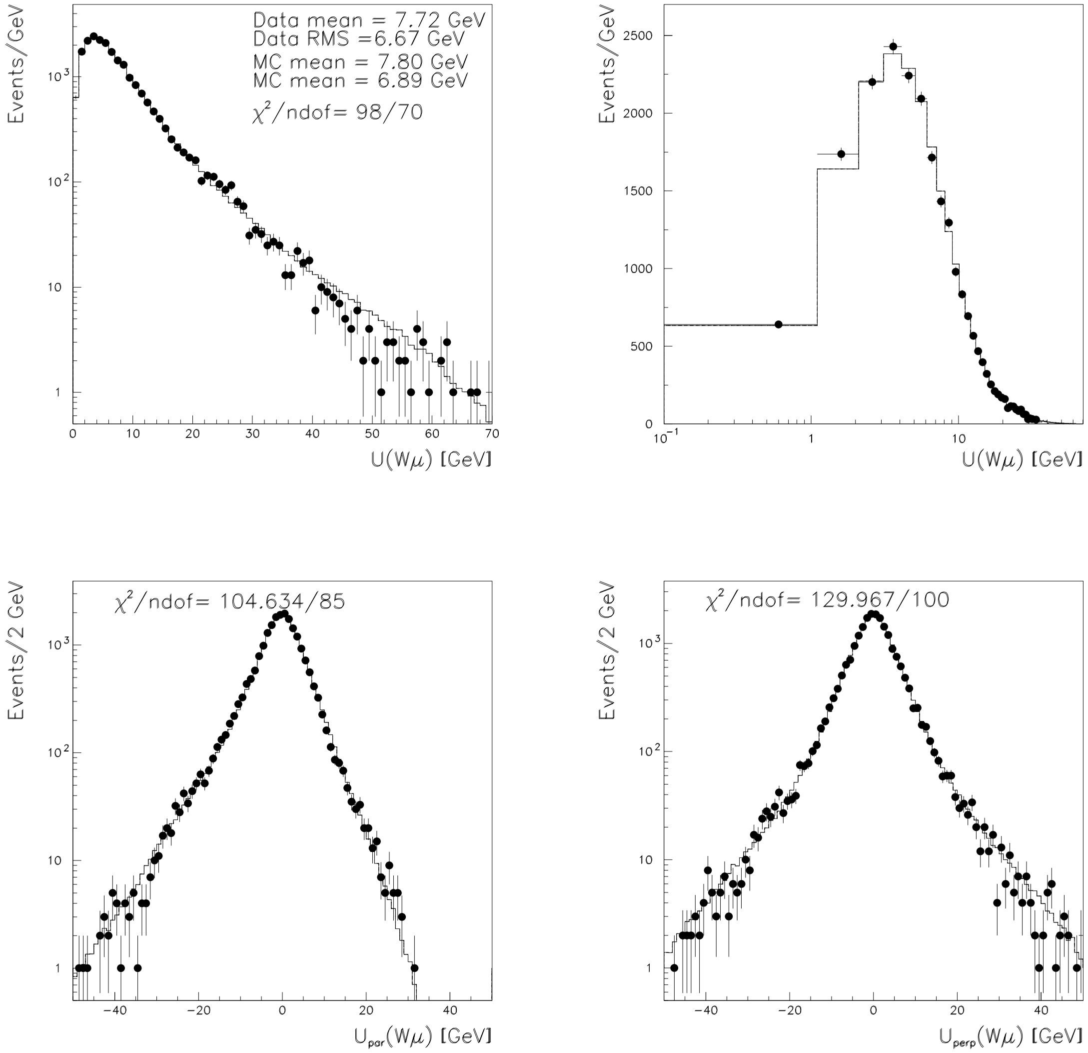

Figure 6.16: $W \rightarrow \mu\nu$. *Upper: the simulation (histogram) of the recoil against the W-boson compared with the data (points). Lower: the components of* $\mathbf{u}$ *parallel and perpendicular to the lepton direction in the data and in the simulation.*

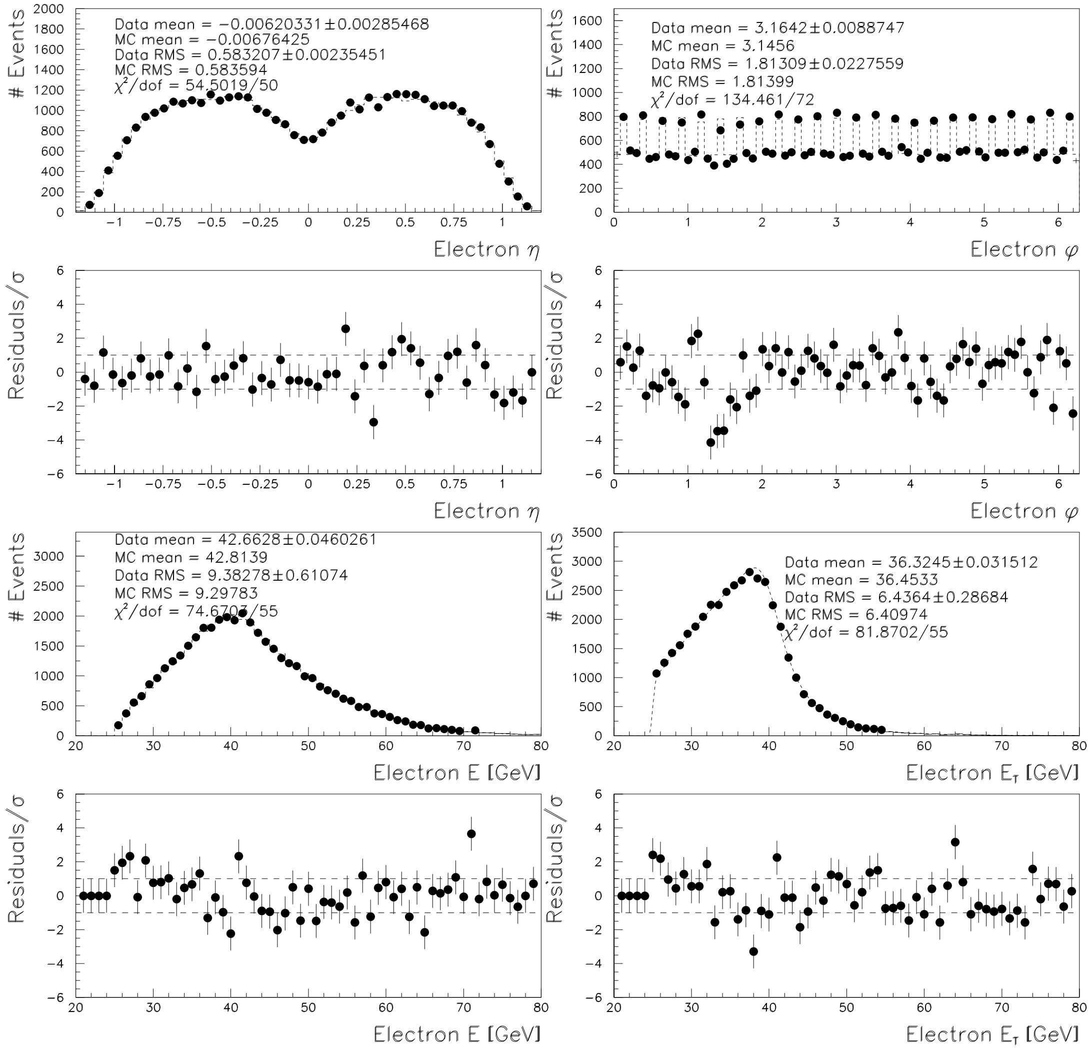

Figure 6.17: *Data and Monte Carlo comparisons for the electron kinematic variables. From upper-left: the pseudorapidity, the ϕ angle, the electron energy and electron transverse-energy. The plots show the data (points) compared to Monte Carlo (histograms). The τ background, which is the dominant background, has been added to the Monte Carlo. Under each distribution, is shown the residuals plot, normalised to the σ in each bin.*

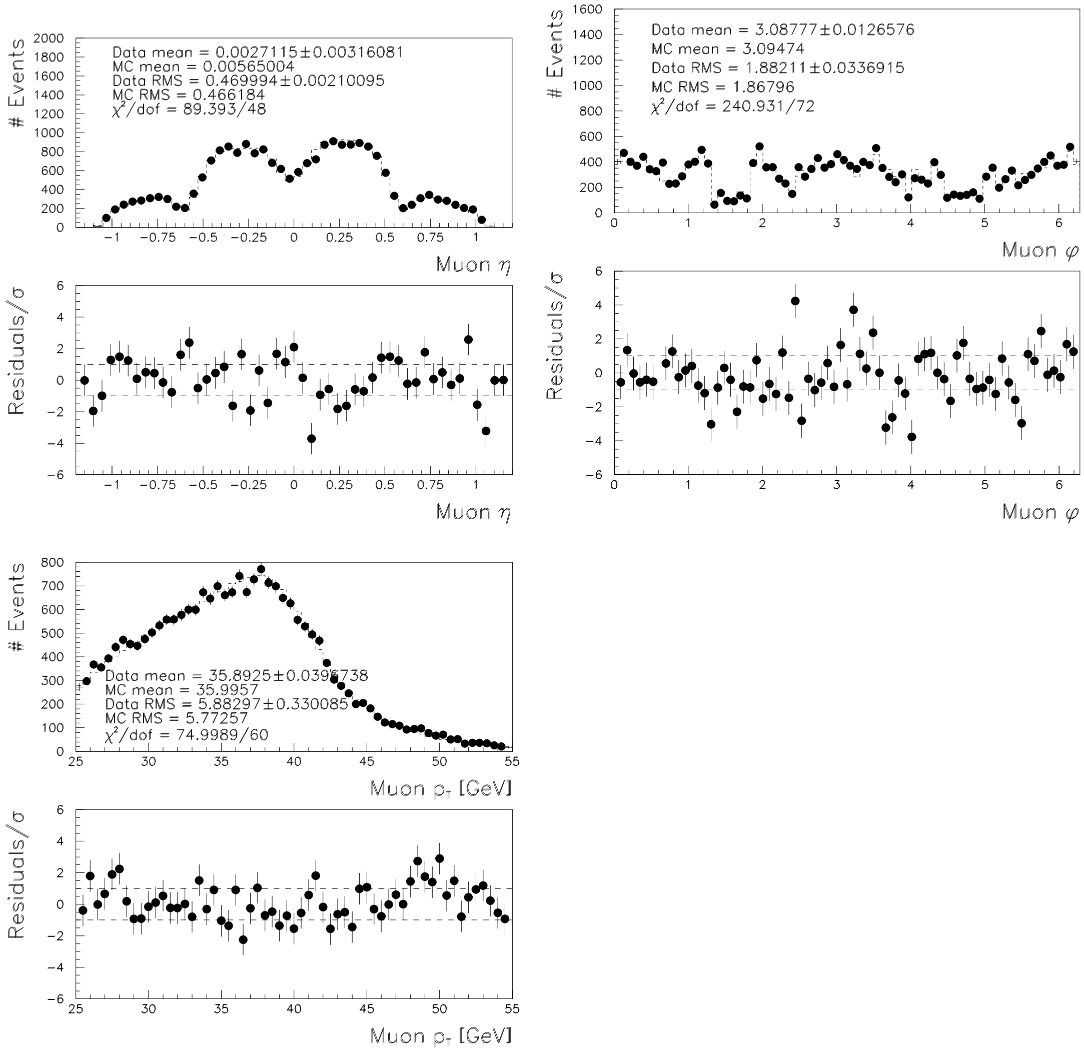

Figure 6.18: *Data and Monte Carlo comparisons for muon kinematic variables. From upper-left: the pseudorapidity, the ϕ angle and muon transverse-momentum. The plots show the data (points) compared to Monte Carlo (histograms). Backgrounds from $W \to \tau\nu$ and $Z \to \mu\mu$ have been added to the Monte Carlo. Under each distribution, is shown the residuals plot, normalised to the σ in each bin.*

Summary:

It is shown that the reconstructed $W \to l\nu$ data can be well described by the simulation after it has been tuned. The tuning is done primarily with reference to the $Z \to ll$ events.

Chapter 7

Backgrounds

There are three main sources of background to the $W \rightarrow l\nu$ data sample of this analysis (where l stands either for an electron or a muon):

- W$\rightarrow$ $\tau\nu$ events, with the τ subsequently decaying into a muon or electron and a neutrino.
- Z$\rightarrow$ l^+l^- events, where one of the leptons is not detected.
- QCD di-jets events, where a jet is wrongly identified as a lepton and the total energy in the event is incorrectly measured to give a missing-E_T signal.

This chapter presents an estimate of these backgrounds. The muon and electron channels are considered and discussed separately in each section.

7.1 W$\rightarrow \tau\nu$ background

The W$\rightarrow \tau\nu$ background is virtually indistinguishable from the W$\rightarrow e\nu$ or W$\rightarrow \mu\nu$. This is because the neutrino from the W-boson, and the two neutrinos from the τ decay, are detected as missing transverse-energy in the detector just like a single neutrino would appear. The TOYGEN generator, used for the simulation of W events in this analysis, is capable of simulating $W \rightarrow \tau\nu$, the τ lepton is then decayed into $\mu\nu\nu$ or $e\nu\nu$. The background level is found to be on the order of 2% of the total W sample. The detailed amounts are listed in Tables 7.2 and 7.3 for the electron and muon channel respectively, in the last section of this chapter. The shape of the transverse-mass distribution is also taken from the Monte Carlo simulation of $W \rightarrow \tau\nu$ events, separately for each of the W-boson recoil ranges.

7.2 Z$\rightarrow l^+l^-$ background

Z events enter the W sample when one of the leptons is not detected ("lost-Z") and there is a missing transverse-energy in the event.

Electron channel: As part of the W candidate selection procedure one of the electrons is always required to be central. However, the second electron track may be going through the fiducial tracking region, the low-efficiency tracking region or completely outside the tracking coverage. There are therefore three cases to be considered:

- The second electron passes through the fiducial tracking volume: the CTC tracking efficiency is considered 100% in this region, therefore the electron is always detected. The track from the CTC is used to form the invariant-mass with the primary electron track and events with invariant-mass between 60 and 120 GeV are rejected. Most of the events rejected in this way have the second electron pointing to a calorimeter crack, which causes the electron energy to be incorrectly measured and fake the missing transverse-energy signature. However, if the second electron has emitted a photon, the invariant-mass with the primary electron track may fall outside the Z invariant-mass exclusion range, although the electron should still be pointing to a calorimeter crack in order to fake a missing energy signal. Therefore in addition to the invariant-mass rejection, the event is rejected if the second electron track, extrapolated to the CES[1] chamber, has $|x_{CES}| > 18$ cm or $|z_{CES}| < 12$ cm. This combination excludes the boundaries between the calorimeter towers and the 90° crack. There is no additional background from Z events considered in this case.

- The second electron points to the region $1 < |\eta| < 1.2$: the rejection procedure works as before, with the only difference that the tracking efficiency in this region decreases to approximately 95% [71]. Therefore if the second electron track is missed by the CTC tracking and points to the 30° calorimeter crack, the event would not be rejected. However, only 8 identified $W \rightarrow e\nu$ candidates have a second electron detected by the CTC going to the 30° crack, so the number of events not rejected because of tracking inefficiencies is espected to be less than 1. The remaining cases are due to the calorimeter inefficiency in good calorimeter response regions and are estimated with the Monte Carlo.

- The second electron has $|\eta| > 1.2$: there are no cracks in this region, so the number of lost-Z events can be simulated with the Monte Carlo using the calorimeter efficiency map. At higher $|\eta|$ the background is also estimated with the Monte Carlo.

---

[1] x_{CES} and z_{CES} are measured in the CES local coordinate frame (see Figure 2.5).

The total background level from lost-Z events is very small, less than 1%, and is listed in Tables 7.2 and 7.3.

Muon channel: The event selection applied in this analysis removes events with opposite-sign muon tracks (found in the CTC) that combine into an invariant-mass greater than 50 GeV. A study reported in [70] has shown that the number of $Z \rightarrow \mu^+\mu^-$ events not removed by the Z selection criteria is consistent with 0. This is when both muons pass through the fiducial tracking volume ($|\eta| < 1$), where the tracking efficiency is very close to 1.

However, a significant number of Z events may enter the W sample when one of the muons goes outside the fiducial tracking volume. About 20% of Z$\rightarrow \mu^+\mu^-$ events have one of the muons outside $|\eta| < 1$, either in the low-efficiency region ($|\eta| \sim 1.1$) or at high η. The estimate of the background in these cases is based on the simulation. The tracking efficiency at $|\eta| \approx 1$ used in the simulation is measured from the $W \rightarrow e\nu$ sample [71], with the plug calorimeter electrons. The background level found is of the order of 4% and it is listed in Tables 7.2 and 7.3. The shape of the transverse-mass distribution of lost-Z events is also derived with the Monte Carlo.

7.3 QCD background

Electron channel: Di-jets events can pass the W selection cuts if one of the jets looks like an electron and one of them is incorrectly measured and gives a high missing-E_T signal. This is referred to as QCD background. Di-jet QCD events are predominantly back to back, therefore QCD background events will look like a jet back to back with either the missing-E_T direction or the electron track. On the other hand, if a jet is present in the event but the electron and the neutrino are coming from a W, the angle with the jet will approximately be

Selection cut		Efficiency	Purity
$\mathrm{ISO}_{0.25} > 1$ GeV	(ISO)	96%	na
$\chi^2_z > 10$	(χ^2)	77%	na
CES z match 5 cm	(CES)	38%	na
$E_{had}/E_{em} > 0.1$	(Had)	73%	na
Combined cuts			
χ^2+ISO		76%	≃100%
χ^2+Had		55%	≃98.5%
ISO+Had		65%	≃100%
Had+χ^2+CES		20%	≃100%
Had+χ^2+ISO		53%	≃98.7%

Table 7.1: *The efficiency and purity in rejecting real electrons to select a sample of QCD background, as determined using a $Z \rightarrow ee$ sample. The combination of two cuts selects an almost pure QCD sample.*

uniformly distributed between 0 and π. The properties of the QCD background can be studied by applying selection cuts that reject real W events. The Z sample is used here to choose the electron rejection cuts that are more efficient. The efficiency of selecting background is measured by checking the impact of each selection cut on a sample of 1115 events that pass the selection criteria of Z candidates except the opposite lepton charge requirement (referred here as "same-sign" events). The purity of the rejection cuts is checked by comparing the number of opposite-sign events left in the sample, versus the number of same-sign events (QCD background is assumed to be symmetric in charge). The results are shown in Table 7.1.

The track isolation plus the χ^2_z anti-selection is the most efficient combination in keeping background while rejecting almost 100% of real W electrons. 1767 events are selected from the W$\rightarrow e\nu$ sample. The distribution of the angle between a jet in the event and the candidate electron ($\Delta\phi(jet-el)$) is shown in Figure 7.1 (upper-left). For comparison, the figure also shows the same distribution from a sample of same-sign events (pure QCD background) selected within the Z$\rightarrow ee$ sample (Figure 7.1 (upper-right)). The distributions show the expected peaks at 0°, 180° and 360° (these are referred to here as "QCD-like", whereas the almost homogeneous $\Delta\phi$ distribution as "W-like").

The lower plots in Figure 7.1 show a fit to the QCD-like and to the W-like distributions. For the left-hand plot, the fitting function is the sum of two exponentials that describe the rise at 0° and 180°, superimposed on a linear function to account for uncorrelated jets:

$$\Delta\phi(jet-el)_{QCD} = e^{p_1+p_2x} + e^{p_3+p_4x} + p_5 + p_6x. \tag{7.1}$$

The template for the W-like distribution is a quadratic function, shown in Figure 7.1 (lower-right).

The background is estimated by applying the isolation cut as: $E <$ ISO$_{0.25} < E + 1$ GeV, for $E = 1,..,9$ and counting the excess of events in each case[2]. The events in excess are counted using the distribution of the angle between electron and jets. The plot is fitted with the sum of the QCD-like plus the W-like templates, leaving the amount of QCD background as a free parameter of the fit. Each fit gives a point in the plot shown in Figure 7.2 (left). The extrapolation to the signal region (ISO$_{0.25} <$ 1 GeV) gives 142 events. Since the distributions of the angles between electron candidates and jets included all the jets in the event, the number of QCD events has been already scaled by the average number of jets per event. This is equal to 3.9 (Figure 7.2, plot on the right-hand side),

---

[2] ISO$_R$ measures the isolation of the lepton candidate. It is defined as the sum of the track scalar-p_T within a cone of size $\Delta R = \sqrt{(\Delta\phi)^2 + (\Delta\eta)^2}$ around and excluding the primary lepton candidate. It is discussed in Section 5.2.

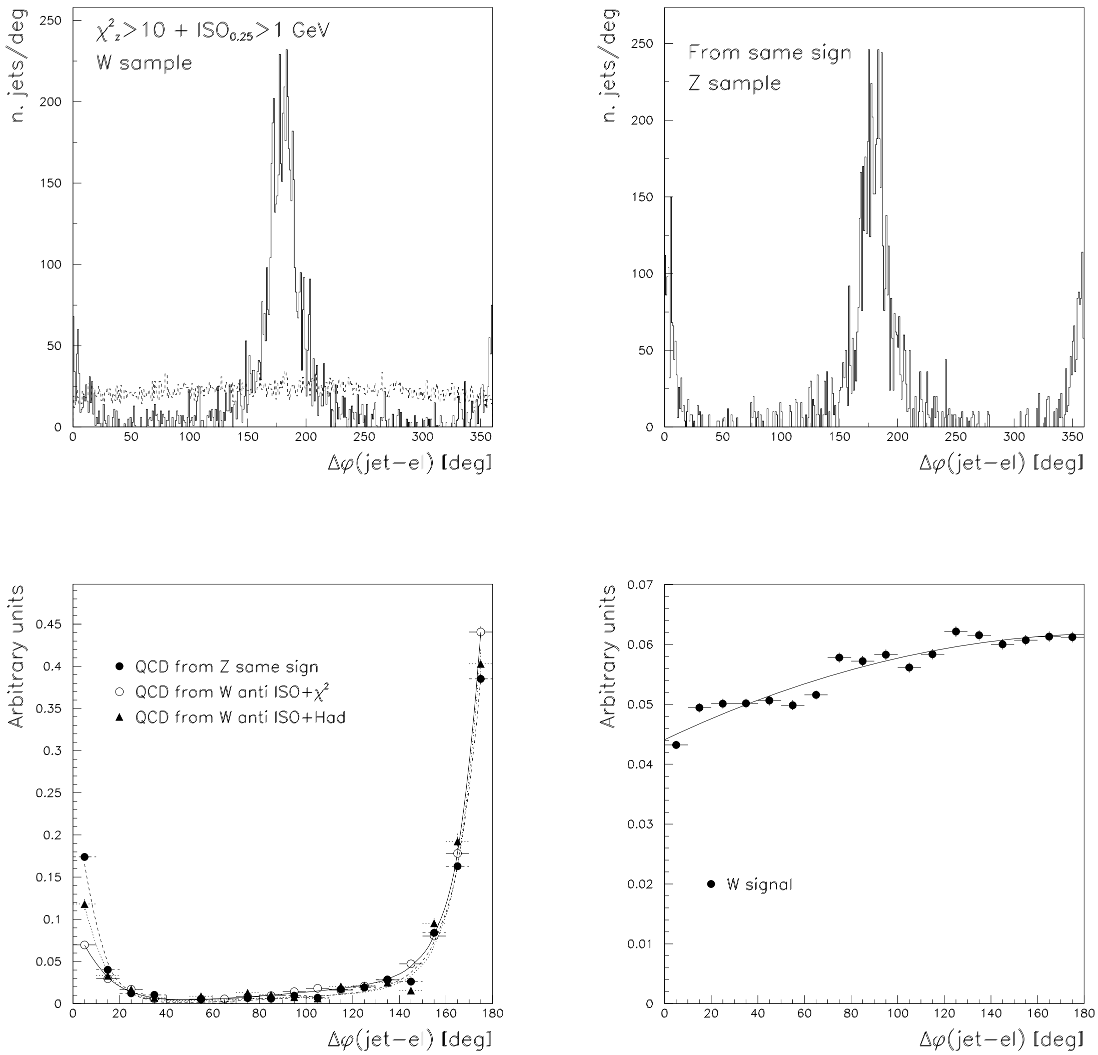

Figure 7.1: *Upper: angle between electron-candidate and jets as it appears in the W sample (continuous line is anti-isolated, dashed line is isolated, both normalised to the same area), and from a background of same-sign combination in the Z sample (right). Lower: fits to the QCD-like distribution (left) and to the W-like distribution (right).*

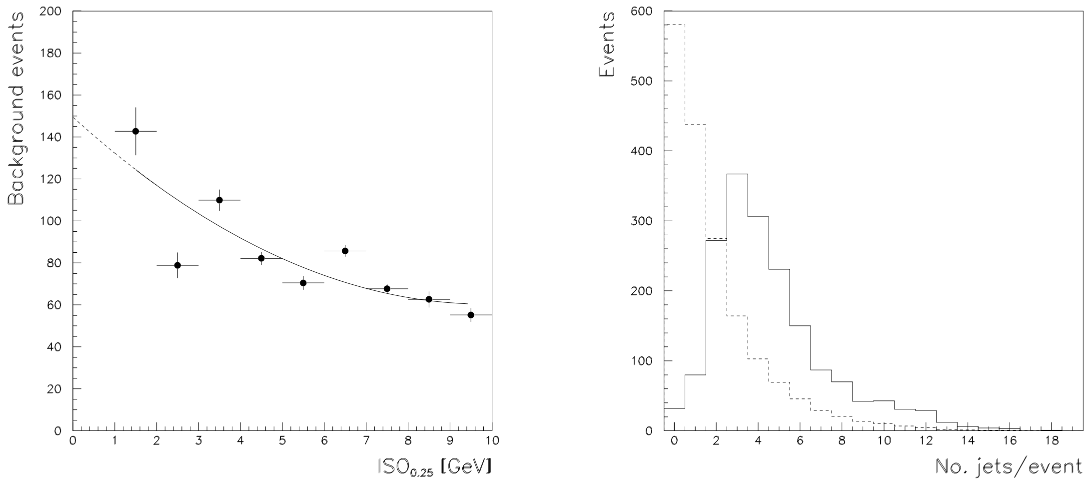

Figure 7.2: *Left: The QCD background versus isolation cut in the W sample. The background estimate is the extrapolation in the signal region (ISO*$_{0.25}$ *< 1 GeV). Right: The number of jets in the event within the electron-ID sample (W candidates, dashed line) and anti-ID sample (background, continuous line).*

measured from the W sample with anti-electron ID cuts. Notice, from Figure 7.1, that although the number of jets appears to be around four, they all have $\Delta\phi$ either close to 0 or π with respect to the primary track. This depends on the definition of a jet, so that a di-jet event here may appear as a multi-jet. The minimum energy of a jet is 5 GeV. To cross-check the estimated number of QCD events, obtained using the angle between lepton and all jets, the same extrapolation procedure has been repeated including the leading jet only. The extrapolation to the signal region gave 162 events. Therefore the average: 151 events is taken as QCD background within the $W \rightarrow e\nu$ sample considered in this analysis. The estimated uncertainty is ±10.

The shape of the transverse-mass distribution of the QCD background is taken from a sample of highly non-isolated electron tracks and is shown in Figure 7.3

(left). This assumes that the shape of the distribution of an isolated background sample is the same as the one of a non-isolated sample. The distribution was fitted with a Gaussian and an exponential function. The function and the parameters of the fit are:

$$f_{QCD}(m_T) = \begin{cases} a \cdot e^{\frac{-(m_T-b)^2}{2c^2}} & (m_T < \text{ 80 GeV}) \\ e^{p+q\cdot m_T} & (m_T \geq \text{ 80 GeV}) \end{cases},$$

with a=249.3, b=70.9, c=15.1, p=8.90, q=−0.044.

The recoil distribution of the QCD background events is also derived from the anti-isolated sample and shown in Figure 7.3 (right).

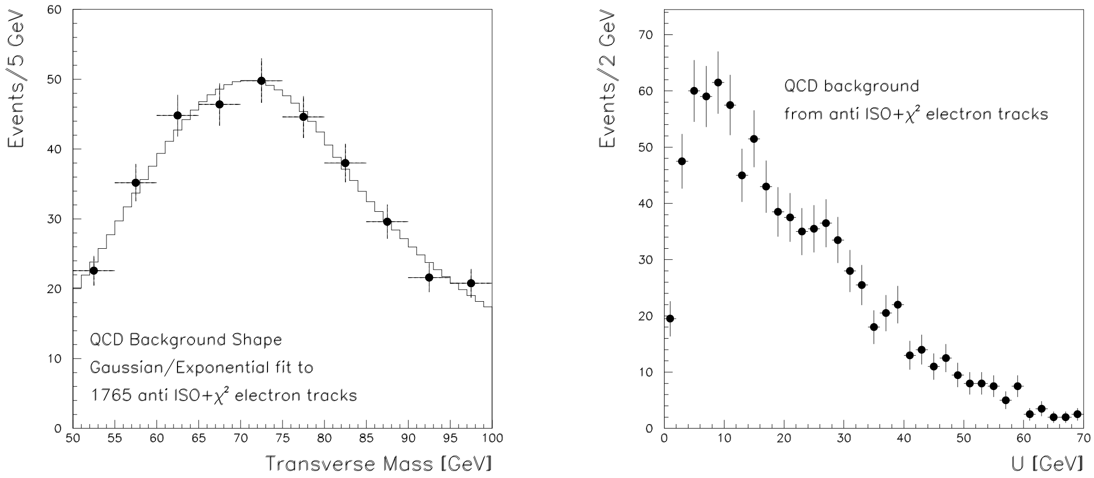

Figure 7.3: *Left: transverse-mass distribution of the QCD background from a sample of highly non-isolated electron tracks. The histogram is obtained from a fit with a Gaussian/exponential function. Right: the recoil distribution of the QCD background.*

Muon channel: QCD events can mimic W→ $\mu\nu$ mainly in two ways. The first is when a heavy flavour quark in one of the jets decays into particles that include a high-p_T muon (e.g. $b \to c\mu\nu$). In order for the muon and neutrino to have enough p_T to pass the W selection cuts, the b-quark needs to have a high transverse-momentum, which leads to small opening angles. Therefore this type of events will have the muon and the neutrino closely parallel to one of the jets. The second type of QCD background process occurs when a constituent hadron is misidentified as a muon. The energy of one of the jets should also be wrongly measured, sufficient to give the appearance of a high missing-E_T signal. In this case, the neutrino and the muon will be reconstructed either nearly parallel to one jet or back-to-back and parallel to the two jets. Moreover, in both the processes considered, the muon will have at least a few tracks near to it. As was done for the electron channel, a measure of the extent of the muon isolation is the ISO$_R$ variable. Typical cone sizes are 0.4 and 0.25.

The method to estimate the background is the same as used for the electron channel, counting the excess of jets back-to-back with the muon or the neutrino for different isolation cuts. However, the isolation cut is not applied to the muon channel, as it is not a particularly efficient cut in this case. Requiring $ISO_{0.4} < 2$ GeV would reject 93 QCD events and about 500 real W events, while retaining 164 QCD background events. Therefore the isolation cut is only used here to estimate the QCD background, but then not applied to the $W \to \mu\nu$ sample. The QCD background is estimated to be 251±60 events.

The shape of the transverse-mass and the recoil distributions is derived from a sample of highly non-isolated muons.

	p_T^W [GeV]				
Type:	(0-10)	(10-20)	(20-35)	(35-100)	All
$W \to \tau\nu$	2.11	1.74	1.46	1.71	2.01
$Z \to e(e)$	0.00	0.02	0.12	0.39	0.01
QCD jets	0.13±0.01	0.49±0.03	1.87±0.13	4.17±0.29	0.34±0.02
Total	2.24±0.01	2.25±0.03	3.37±0.13	6.27±0.29	2.36±0.02

Table 7.2: *Summary of the backgrounds to $W \to e\nu$ (as percentages of the W candidate sample) in different p_T^W ranges. The errors are negligible for $W \to \tau\nu$ and $Z \to e(e)$.*

	p_T^W [GeV]				
Type:	(0-7.5)	(7.5-15)	(15-30)	(30-70)	All
$W \to \tau\nu$	2.24	1.94	1.63	2.37	2.11
$Z \to \mu(\mu)$	4.25	4.00	3.67	2.95	4.11
QCD jets	0.40±0.10	1.90±0.50	2.90±0.70	2.90±0.70	1.10±0.30
Total	6.89±0.10	7.84±0.5	8.20±0.70	8.22±0.70	7.32±0.12

Table 7.3: *Summary of the backgrounds to $W \to \mu\nu$ (as percentages of the W candidate sample) in different p_T^W ranges. The errors are negligible for $W \to \tau\nu$ and $Z \to \mu(\mu)$.*

7.4 Summary of backgrounds

$W \rightarrow \tau\nu$, lost-Z events and QCD jets are the main sources of background to the $W \rightarrow e\nu$ and $W \rightarrow \mu\nu$ data samples considered in this analysis. The possibility of background from $t\bar{t}$ events, at high-p_T^W, has also been considered but it is estimated to be negligible [80]. The background levels, as percentages of the W candidate sample, are shown in Table 7.2 for the electron channel and Table 7.3 for the muon channel. The estimate is shown in different p_T^W ranges. The shape of the transverse-mass given by each background source is plotted in Figure 7.4 (electron channel) and Figure 7.5 (muon channel) in the four p_T^W regions.

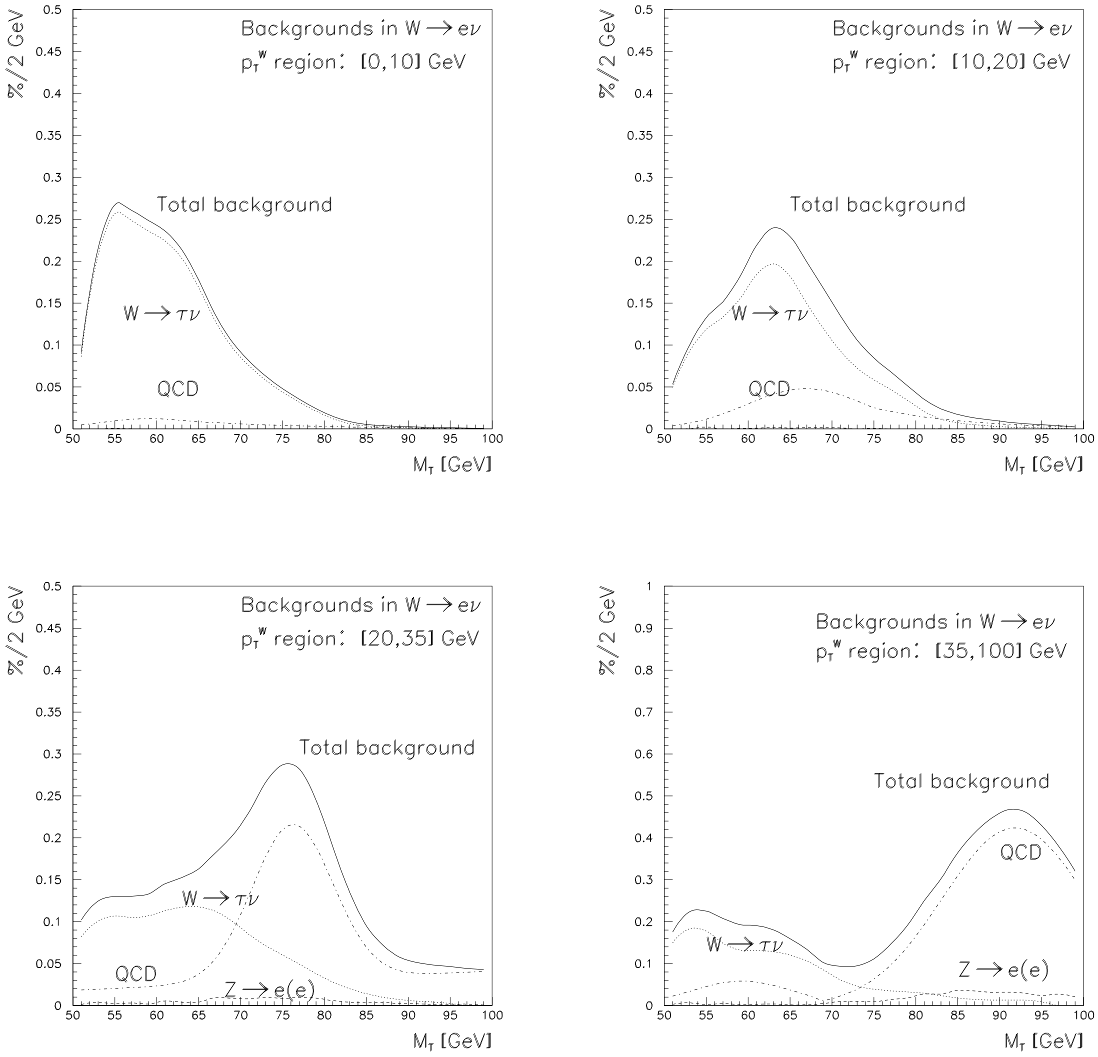

Figure 7.4: *Electron channel: the transverse-mass distribution from the background sources in four* p_T^W *ranges. The plots are in percentage of the W data in the specific* p_T^W *region.*

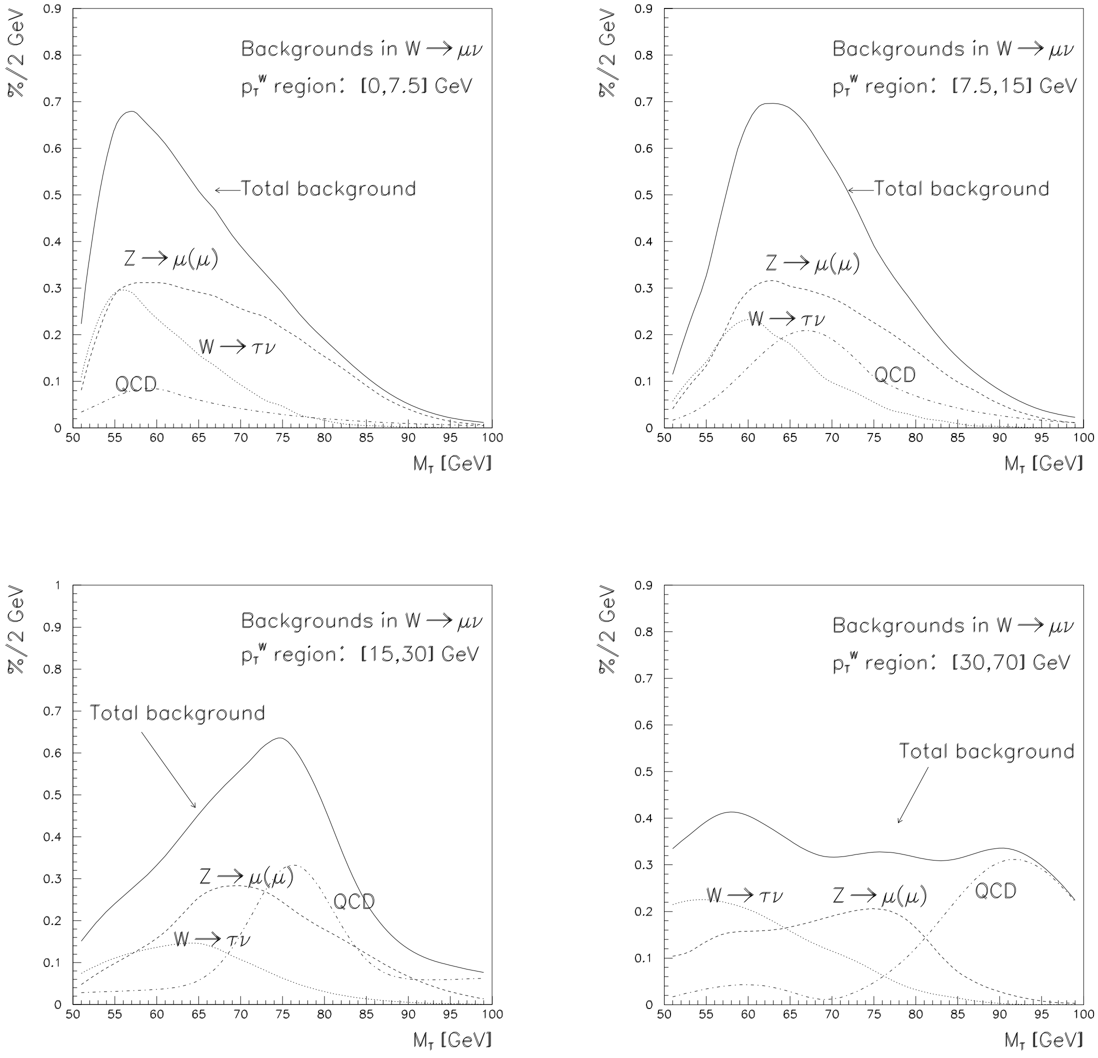

Figure 7.5: *Muon channel: the transverse-mass distribution from the background sources in four p_T^W ranges. The plots are in percentage of the W data in the specific p_T^W region.*

Chapter 8

The Measurement of the Coefficients of the Polar-Angle Distribution

This chapter presents the results of the measurement of α_2, obtained from the analysis of the electron and muon decay channels. After briefly summarising the measurement strategy, the first section contains the fits for α_2 and the evaluation of the systematic error. The second section shows a tentative set of fits for α_1. However, the sensitivity is too poor for a statistically significant measurement of α_1.

8.1 The measurement of α_2

8.1.1 The measurement method

The measurement exploits the relationship between the W-boson transverse-mass distribution and the lepton polar-angle distribution. A set of Monte Carlo generated templates of the M_T distribution is compared to the plot derived from the data. The details of the measurement strategy were presented in Chapter 4, together with an estimate of the statistical sensitivity.

The Monte Carlo templates are generated using a weighted leptonic angular distribution, each template with a different value of α_2. At low p_T^W (< 35 GeV), α_1 is set to $2\sqrt{\alpha_2}$, which is an approximation of the SM expectation for $p_T^W \to 0$. At high p_T^W (> 35 GeV), α_1 is set to the full SM theoretical prediction, which is function of p_T^W. The dependence[1] of the measured α_2 on the input α_1 is cross-checked in the context of the evaluation of systematic error with a simultaneous two-parameter fit. The template-distributions derived from the Monte Carlo are then normalised to the number of data entries, and their shape is compared to the histogram from the data. A log-likelihood method is used to find the best estimate of α_2.

To measure α_2 as a function of the W transverse-momentum, the data sample is divided in four regions of the W-recoil. Because of the difference between the W-recoil measurement and the true transverse-momentum, the set of events that fall within a recoil bin have a corresponding p_T^W distribution. The measured value of α_2 in each recoil-bin is effectively the measurement of α_2 over the corresponding true p_T^W spectrum. This is with good approximation a measurement of α_2 at the mean ($\bar{p}_T^W$) of the distribution of the true transverse-momentum. This observation

---

[1] Although the transverse-mass distribution is independent on α_1 at first order, a residual dependence enters the distribution because of the limited detector acceptance.

is expanded and justified in Appendix A, and it has been checked with the Monte Carlo in Chapter 4. The W-recoil binning for $W \rightarrow e\nu$ and $W \rightarrow \mu\nu$ channels is different due to the different size of the samples.

8.1.2 The log-likelihood fits

When each template-distribution is compared to the data, a likelihood number is computed according to:

$$\log L = \sum_{i=1}^{Nbin} n_i^{data} \log\left(\frac{n_i^{MC}}{n_{tot}^{MC}}\right), \tag{8.1}$$

where the sum runs over the number of bins of the M_T histogram; n_i^{data} and n_i^{MC} represent the number of entries in each bin, in the data and in the template-histogram respectively. n_{tot}^{MC} is the total number of events in the histograms, which are normalised to the data. The maximum of the likelihood function locates the best estimate for the value for α_2. Figure 8.1 shows the likelihood functions in four different recoil-regions for the electron channel (left-hand side plots) and for the muon channel (right-hand side plots). The likelihood functions have been shifted vertically so that the maximum is always at zero. The 1σ statistical error on each fit is evaluated at the points on the likelihood curve which are 1/2 unit below the maximum. Figures 8.2 and 8.3 show the the transverse-mass distribution of the data compared with the simulation, where α_2 has been set to the best-estimate values. The simulation reproduces very well the data, with normalised χ^2 values close to 1.

Table 8.1 summarises the measurement of α_2 from $W \rightarrow e\nu$. Table 8.2 summarises the results from $W \rightarrow \mu\nu$. Figure 8.4 shows the results of the measurement on a plot of α_2 versus p_T^W. The line represents the Standard Model prediction reported in [38].

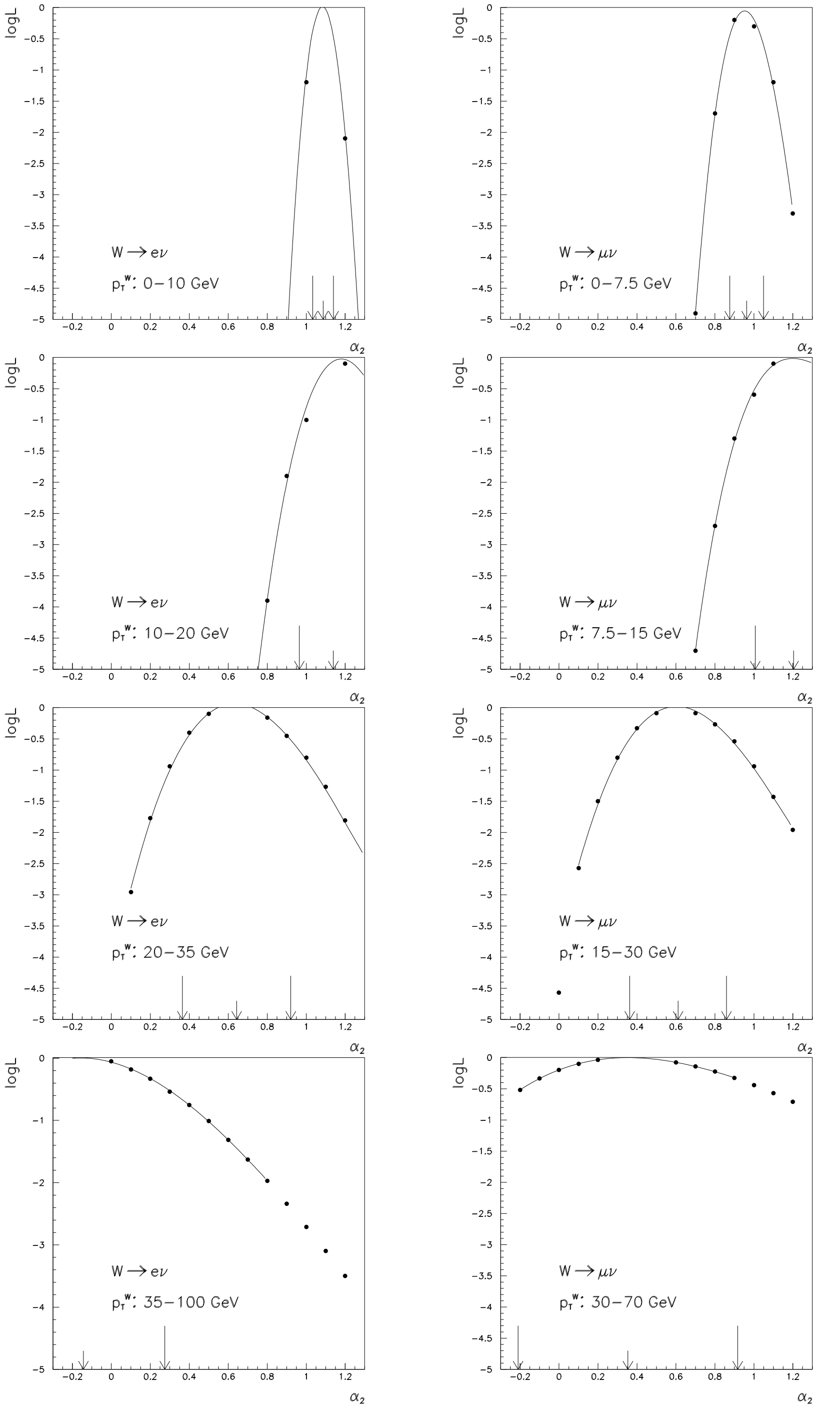

Figure 8.1: *The log-likelihood functions of the fits for* α_2*, in four W-boson recoil-regions for the electron (left-hand side plots) and muon (right-hand side plots) channels. The arrows locate the maximum of the log-likelihood function and the points at which the value drops 1/2 units from the maximum.*

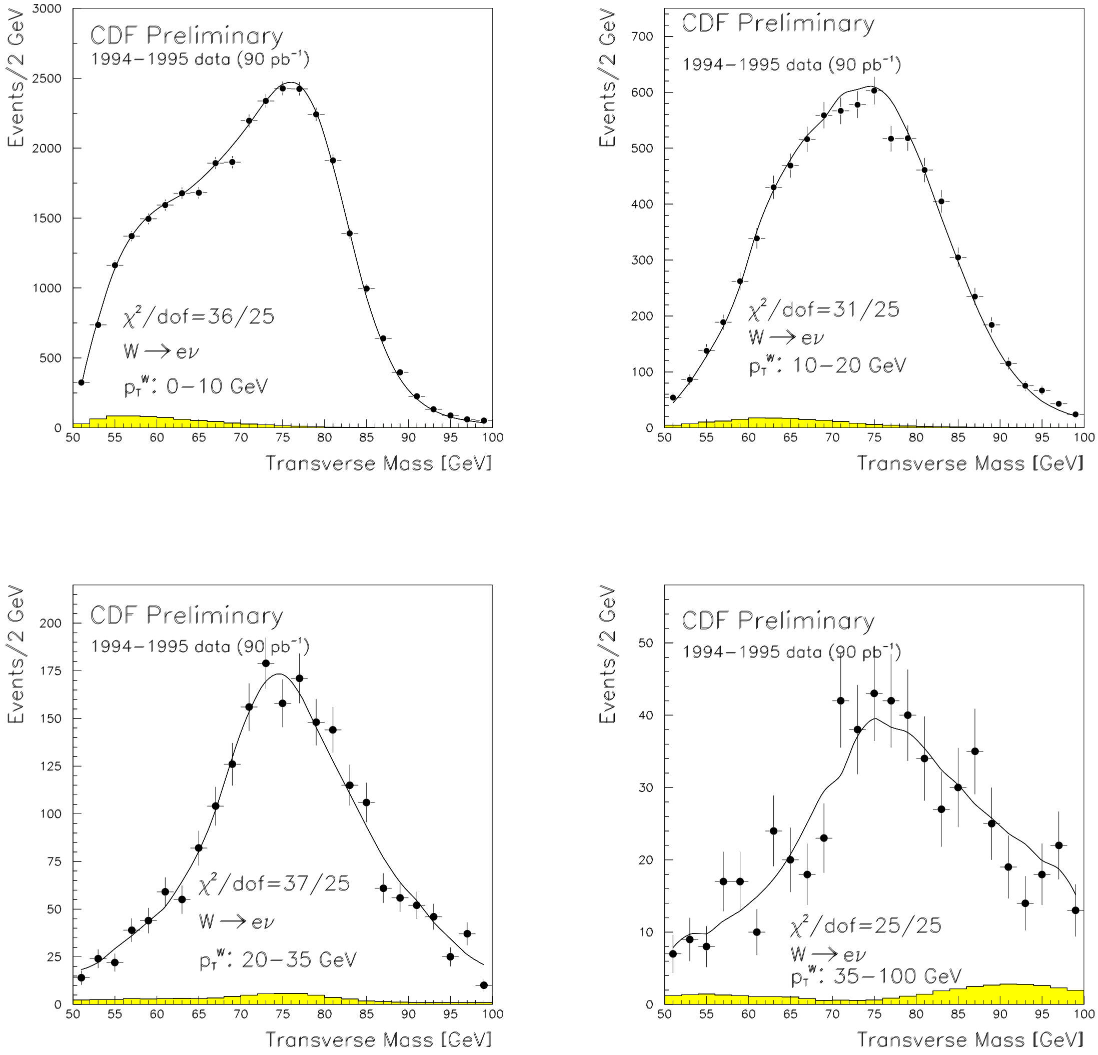

Figure 8.2: *The comparison of the transverse-mass distribution from the* $W \rightarrow e\nu$ *data (filled circles) with the simulation (continuous line) in four recoil-regions. The shaded histogram is the estimated background and is added to the simulation. In the Monte Carlo,* α_2 *has been assigned the best-fit value for each recoil-range.*

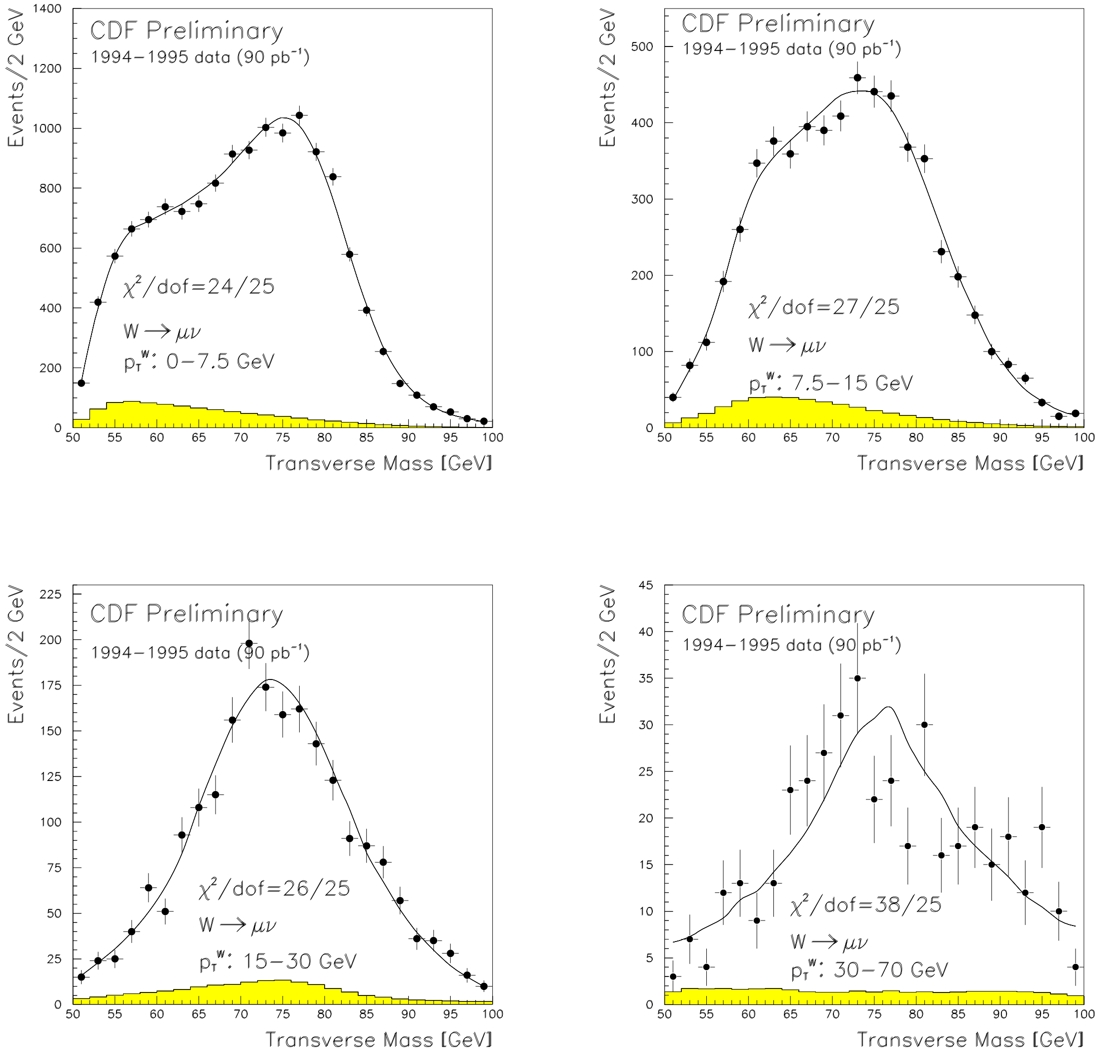

Figure 8.3: *The comparison of the transverse-mass distribution from the* $W \rightarrow \mu\nu$ *data (filled circles) with the simulation (continuous line) in four recoil-regions. The shaded histogram is the estimated background and is added to the simulation. In the Monte Carlo,* α_2 *has been assigned the best-fit value for each recoil-range.*

The four measurement-points from the electron channel can be combined with the measurement from the muon channel to compute a χ^2 with respect to the Standard Model expectation. The result is: χ^2=10.6 with 8 degrees of freedom. The agreement is good. The measurement at p_T^W around 15 GeV is slightly high for both the muon and electron channel. This could be due to small short comings of the event and detector simulation. The recoil-range between 10 and 20 GeV is the most difficult to model as it corresponds to the peak of a sharply falling distribution (the p_T^W spectrum). The analysis of the systematic error is discussed in the next section.

The measurements of α_2 with the electron and muon channels are combined in Figure 8.5. The position in p_T^W is determined by a weighted mean of each pair of electron and muon measurements. The points are then scaled using a liner fit of α_2 to the data and averaged according to the size of the errors. The triangles are from [36] and are plotted here for comparison.

8.1.3 Systematic uncertainties

Systematic uncertainties for this analysis derive mainly from the simulation of the W events, the detector response and the estimate of the backgrounds. Some of these, although classified as systematic, may be statistical in nature. This is the case, for instance, for the detector recoil-response and the W transverse-momentum spectrum. In fact, they are derived from the $Z \to ee$ and $Z \to \mu\mu$ data samples and suffer from low statistics at high transverse-momentum. In the following, each source of systematic error is discussed and an estimate is determined for the total error. Tables 8.1 and 8.2 summarise the various contributions and the total systematic error.

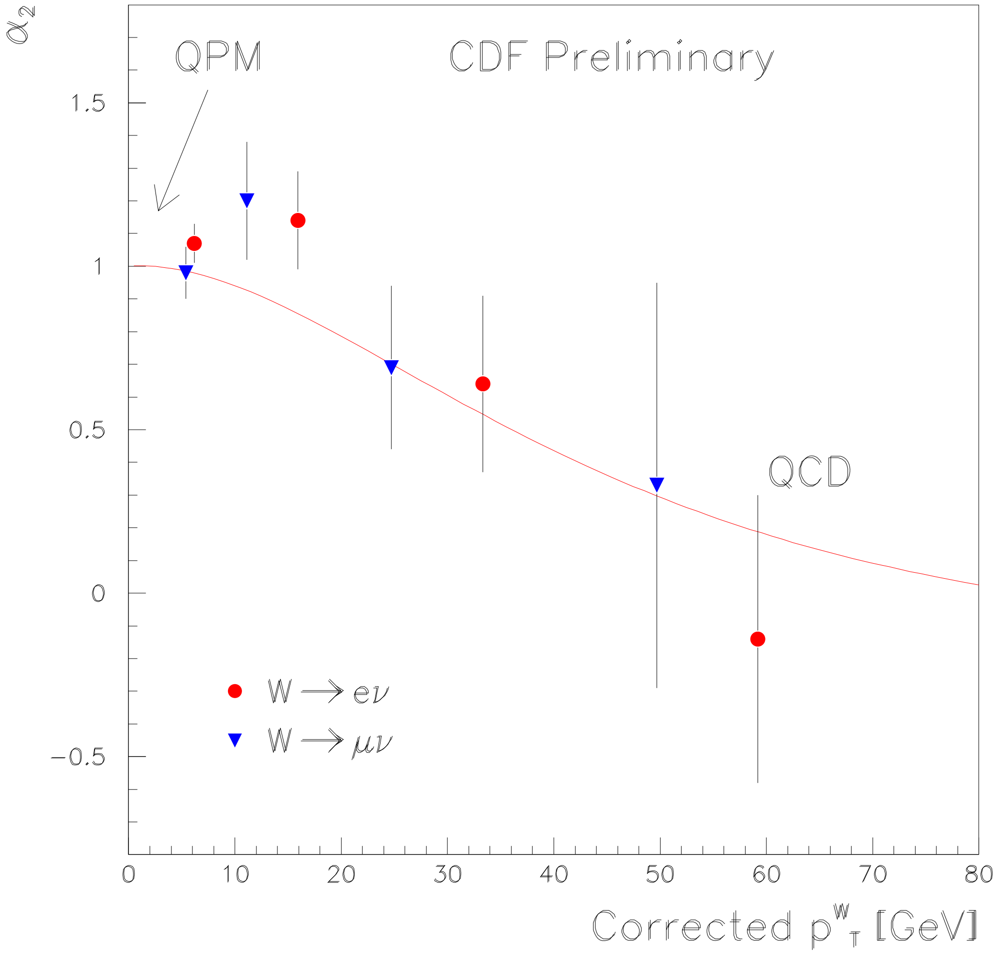

Figure 8.4: *The measurement of α_2 with the muon (filled circles) and the electron (triangles) channels. The error-bars are statistics only.*

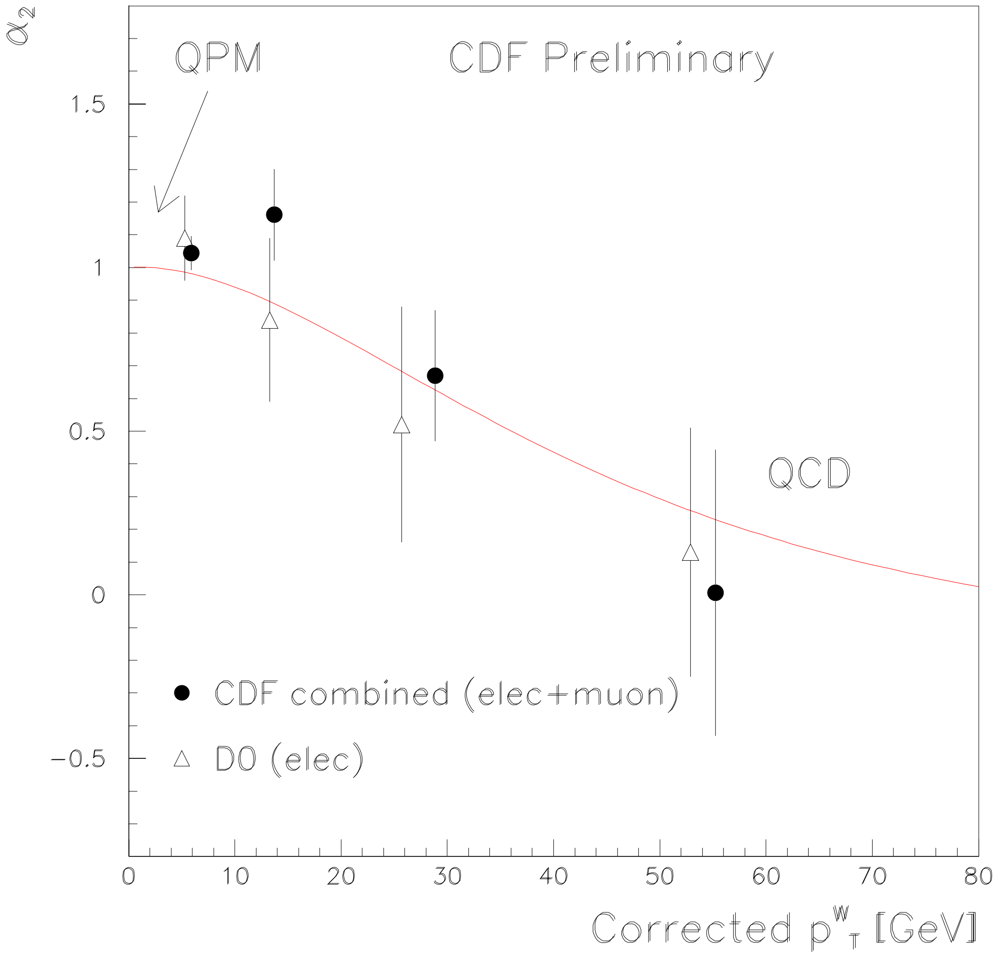

Figure 8.5: *The measurement of α_2 combining the electron and the muon channels (filled circles). The error-bars show the combination of the statistic and systematic errors. The D0 measurement (open triangles) is from [36] and includes systematic errors.*

Recoil-range [GeV]	0−10	10−20	20−35	35−100
α_2 measured	**1.07**	**1.14**	**0.64**	**−0.14**
Statistical error	±0.05	±0.15	±0.27	±0.44
α_2 predicted	0.98	0.84	0.55	0.25
Mean $\bar{p}_T^W$ [GeV]	6.2	15.9	33.3	59.2
$N_{\rm evt}$	31363	7739	2033	595
Systematic errors:				
PDF's	±0.01	±0.01	±0.01	±0.01
W mass	±0.02	±0.04	±0.03	±0.10
Input p_T^Z	±0.02	±0.04	±0.05	±0.09
Recoil model	±0.01	±0.05	±0.04	±0.20
QCD background	±0.01	±0.01	±0.01	±0.01
Combined systematic	±0.03	±0.08	±0.07	±0.24

Table 8.1: *The measurement of α_2 with the $W \to e\nu$ data. The mean $\bar{p}_T^W$ corresponding to each recoil-range is the mean of the distribution of the "true" W transverse-momentum in the Monte Carlo.*

Parton Density Functions:

The parton distribution functions (PDF's) are used in the Monte Carlo simulation to determine the quark content in the proton, and hence the rapidity dependence of the generated W-bosons. The set of PDF's used to simulate the events in this analysis is MRS-R2 [81], used also in [21]. These PDF's describe well the low-η W-charge asymmetry data. Several other sets of PDF's, like MRMS-D's, don't describe well the CDF data. To evaluate the impact of the choice of PDF's on the measurement of α_2, two Monte Carlo samples has been generated with MRMS-D^- and MRMS-D0. α_2 has been then derived from the new set of templates. The observed shifts are ±0.01 in all recoil-regions, which is considered as the

Recoil-range [GeV]	0−7.5	7.5−15	15−30	30−70
α_2 measured	**0.98**	**1.20**	**0.69**	**0.33**
Statistical error	±0.08	±0.18	±0.25	±0.63
α_2 predicted	0.99	0.92	0.70	0.32
Mean $\bar{p}_T^W$ [GeV]	5.4	11.1	24.7	49.7
$\mathrm{N}_{\mathrm{evt}}$	13813	5910	2088	424
Systematic errors:				
PDF's	±0.01	±0.01	±0.01	±0.01
W mass	±0.02	±0.04	±0.03	±0.10
Input p_T^Z	±0.02	±0.04	±0.05	±0.09
Recoil model	±0.01	±0.05	±0.04	±0.20
QCD background	±0.01	±0.02	±0.03	±0.05
Combined systematic	±0.03	±0.08	±0.08	±0.25

Table 8.2: *The measurement of α_2 with the $W \to \mu\nu$ data. The mean $\bar{p}_T^W$ corresponding to each recoil-range is the mean of the distribution of the "true" W transverse-momentum in the Monte Carlo.*

systematic error.

The W mass:

The transverse-mass distribution is sensitive to the value of the W mass that is used in the Monte Carlo. The dependence comes from the fact that the transverse-mass spectrum has a Jacobian peak at about the value of the W mass. The value of the W mass in the Monte Carlo is set to the LEP average [82]. The uncertainty on M_W determines an uncertainty on α_2 of 0.02−0.03.

p_T^W spectrum:

The W transverse-momentum spectrum is derived from the Z sample by measuring p_T^Z, and using the relatively well known ratio p_T^W/p_T^Z from the theory. The p_T^Z distribution is measured from both the $Z \to ee$ and $Z \to \mu\mu$ data, and the latter is used in this analysis. Figure 8.6 shows the corrected p_T^Z spectrum derived from $Z \to ee$ and $Z \to \mu\mu$ data. Because of the limited statistics of the Z samples, the uncertainty in determining p_T^Z is not negligible. An estimate of the systematics on α_2 is given by using the distribution of p_T^Z from $Z \to ee$ instead. The measured α_2 is shifted between 0.01 at the first bin and 0.09 at the last one.

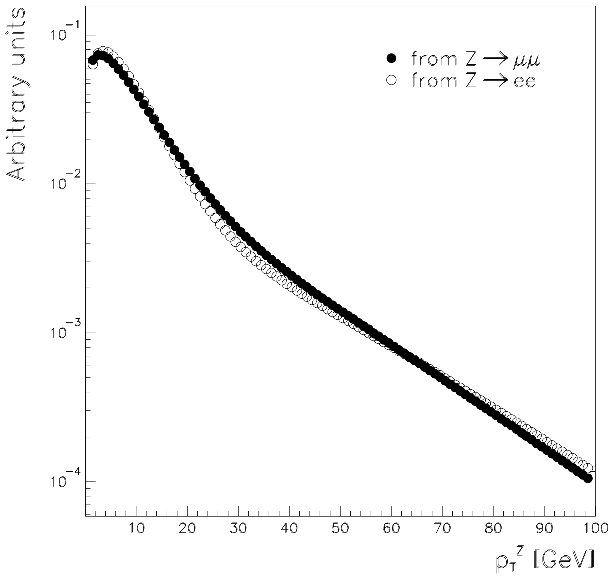

Figure 8.6: *The p_T^Z spectrum, determined from $Z \to ee$ and $Z \to \mu\mu$ data.*

Recoil Model:

The recoil model consists of response and resolution functions derived from the $Z \to ee$ data. By using $Z \to \mu\mu$ data instead there are slight variations in the coefficients of the model, which are used here to evaluate the systematics associated with the determination of the parameters. Each of the parameters is changed and the α_2 values measured. The dispersion of the set of new measurements is taken as the systematic error. The error increases with p_T^W. The recoil model is one of the main sources of background here since it is constrained with a statistical sample much smaller than the W sample itself. In past analyses [21], it has been preferred to determine the recoil model by including the W-recoil distribution to optimise the fit while keeping a set of parameters that describe well the Z data. In this analysis, the W-recoil distribution has not been used to optimise the fit to avoid a possible source of bias. As a further check of the impact of a slight disagreement of the W transverse-momentum distribution between the data and the simulation, α_2 has been measured by shifting the bin edges one at a time by 0.1 GeV only in the data but not in the Monte Carlo, so as to simulate an event migration between bins with the consequent impact on the shape of the transverse-mass distribution. The value of 0.1 GeV is the upper limit of disagreement between data and simulation of the mean of the p_T^W distribution in this analysis. α_2 has been observed to shift between 0.01 and 0.04 in the four bins. This is not considered in the final systematic error estimate as it only evaluates the sensitivity of the measurement to the bin edges and it should be included in the recoil model systematic error estimate given above.

The angular coefficients and α_1 input value:

Although the distribution of $|\cos\theta|$ should only depend on α_2 and all the remaining angular coefficients should integrate out, in practice acceptance cuts may cause other angular coefficients to enter the distribution. During the fit for α_2, the angular coefficients A_2 and A_3 (see Equation 1.17) are set to their Standard Model expectation (which is approximately a quadratic function of p_T^W). A_1, A_5, A_6, A_7 are expected to be very small and hence set to zero. To evaluate the sensitivity to these terms, a linear approximation to the SM prediction of A_2 and A_3 would shift α_2 by $0.02-0.07$ in the four p_T^W bins. However, these values are not included in the systematic error since the uncertainty on the theoretical SM calculation is expected to be smaller.

Also α_1 (angular coefficient A_4) is coupled to α_2. Figure 8.7 shows the maximum of the likelihood function in the 2D plane where both α_1 and α_2 are varied simultaneously. α_1 could be measured in this way, with a 2-dimensional fit, but the sensitivity is too low, and significantly model-dependent. α_1 is discussed in its own right in the next section. The contours show that there is only a weak correlation between the two parameters.

Backgrounds:
The main source of uncertainty from backgrounds comes from the estimate of the QCD background. The background is estimated using the lepton isolation cut and the angular distribution between lepton and jets in the event. The uncertainty on the muon channel is higher due to the lower yields. The systematic error is derived by changing the QCD background content in each bin, by the uncertainty given by the background estimate.

8.2 The prospects for a measurement of α_1

Despite the efforts to determine the sign on $\cos\theta$ in the Collins-Soper W rest-frame, as described in Chapter 4, the sensitivity for the measurement of α_1 is too low. The reason is obviously the poor resolution of the neutrino ambiguity. Figure 8.8 shows an example of the transverse-mass plot with the $\cos\theta$-sign separation. The plot shows how small the sensitivity of the templates is to different α_1 values.

The most appropriate way of using the distributions of Figure 8.8 is to subtract the positive and the negative parts of the plot, and to look at the difference between the two. This cancels most of the systematics associated with the measurement. By doing so, the sensitivity to α_1 looks even further reduced. In fact, the biggest part of the variation on the templates is not due to the sign identification, but to the dependence of the transverse-mass on α_1. The dependence comes

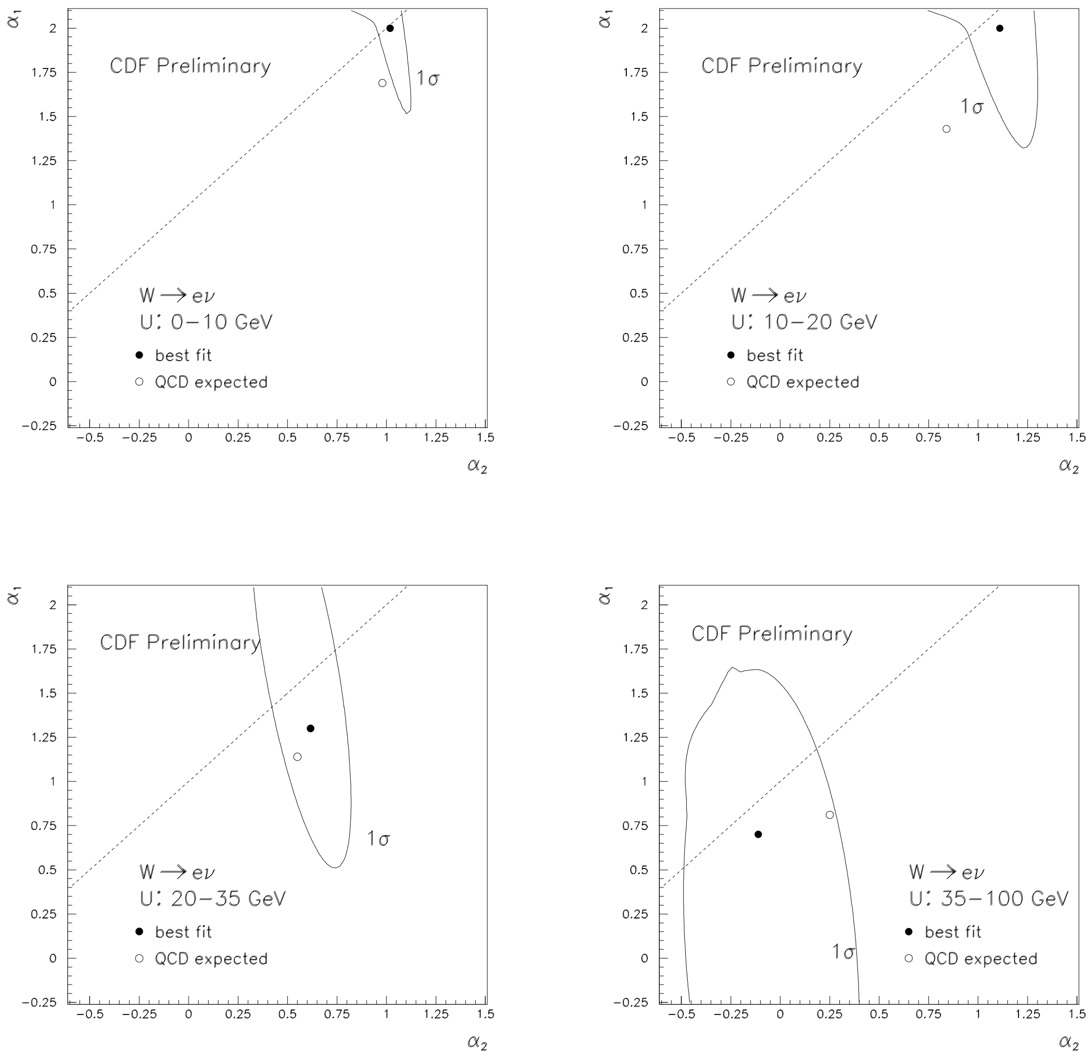

Figure 8.7: *Simultaneous fits for α_2 and α_1. The filled circles indicate the maximum of the likelihood function, the open circles are the SM expectation and the contour line is the 1σ error.*

from the acceptance cuts, as noted in the previous section. Such dependence is highly model-dependent. In particular, it is dependent on the perfect simulation of acceptance cuts and efficiencies and therefore liable to large systematic error. By fitting the difference of the negative and the positive parts of the transverse-mass histogram, estimates of α_1 can be obtained – these are shown in Figure 8.9. The error bars are from statistics only.

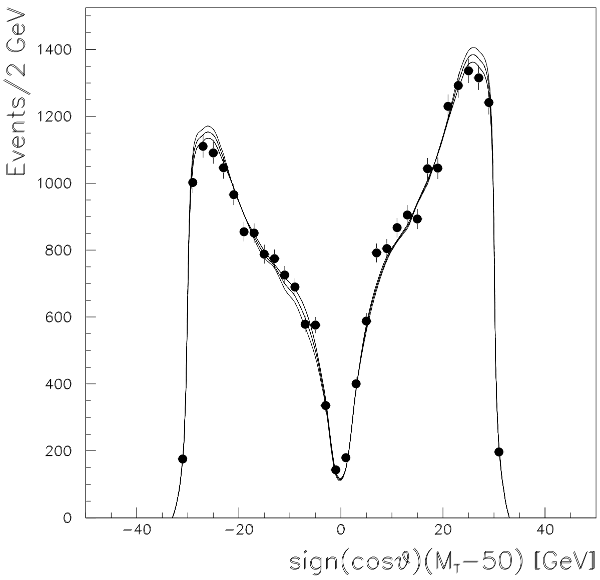

Figure 8.8: *Distribution of the transverse-mass signed with the sign of* $\cos\theta$*. The points are* $W \to e\nu$ *data with* p_T^W *<10 GeV, the lines are from the simulation where* $\alpha_1 = 0., 1.0, 2.0$*. The transverse-mass is signed with the sign of* $\cos\theta$ *and shifted by 50 GeV, so that the 50–100 GeV range is plotted as 0–50 GeV.*

In the future, a handle on the measurement of α_1 at CDF will come from using information from the new plug calorimeter. In this analysis it has been shown that it is not possible to distinguish efficiently the sign of $\cos\theta$ at the Tevatron, by using only transverse quantities. An estimate of the energy imbalance in the longitudinal direction would greatly help in solving the neutrino ambiguity. Also, using leptons in the high-rapidity region of the detector will increase the sensitivity.

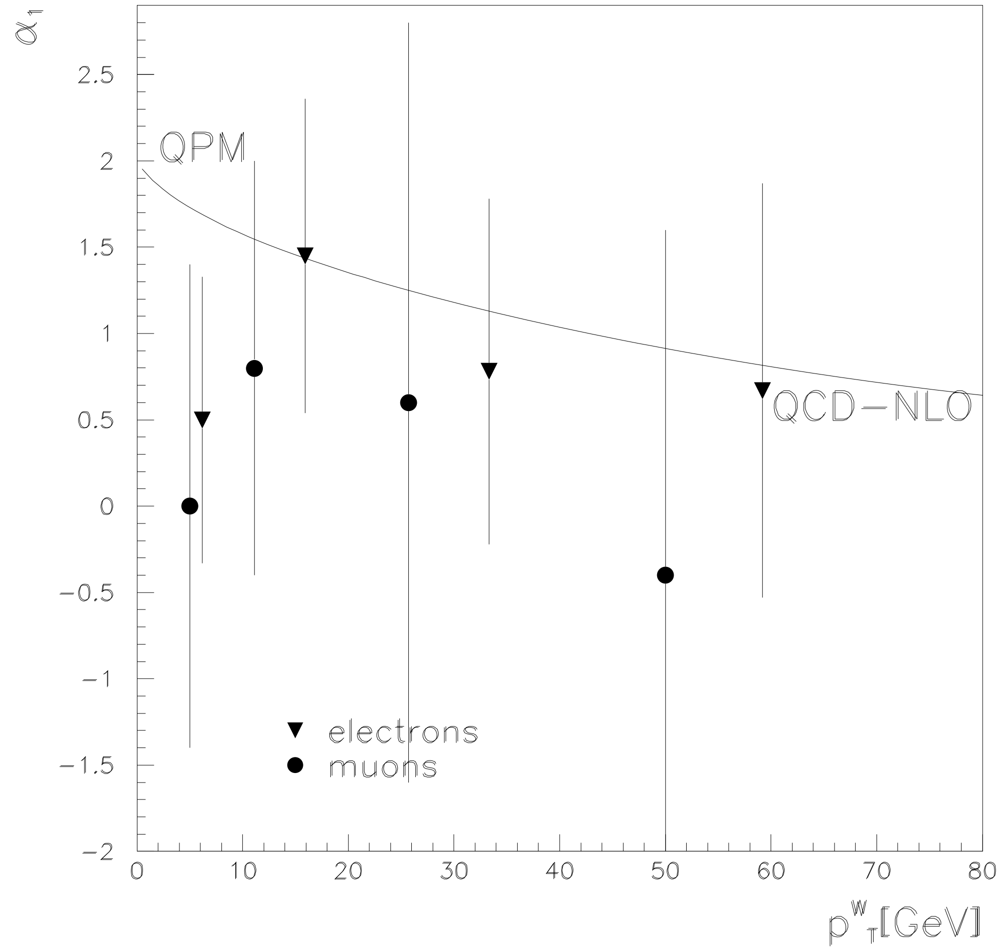

Figure 8.9: *The measurement of* α_1 *with the muon channel (filled circles) and electron channel (triangles) channels. The error-bars are from statistics only.*

Conclusions

This thesis describes a measurement of the polar-angle distribution of electrons and muons from W decay data, as a function of the W transverse-momentum. The measurement exploits the dependence of the shape of the W-boson transverse-mass distribution on the leptonic angular distribution. To start with, the strategy for the measurement was studied with a fast Monte Carlo. From this study, the α_2 coefficient seemed to be measurable with good sensitivity using the CDF Run Ib data-sample of high-p_T W-bosons. However, the measurement of α_1 is made particularly difficult by the poor resolution of the neutrino ambiguity. Due to the high energy of the beam, only a limited discrimination is provided by the study of the W boost in the laboratory-frame.

Chapters 4 to 8 describe in detail the extraction of the α_2 coefficient. The Monte Carlo simulation of the W events and the detector response has been shown to reproduce well the data. The implementation of the angular distribution, the p_T^W spectrum and the detector response to the recoil against the W, have been tuned and developed for this measurement. The sample of selected W leptonic decays consisted of about 50,000 events with p_T^W up to 100 GeV. The main sources of backgrounds have also been considered and added to the transverse-mass spectra in the simulation. The results of the measurement of α_2 agree with the theoretical prediction of the Standard Model, in particular, the expectations of Leading-Order (and Next-to-Leading Order) QCD.

Appendix A:

The position of the α_2 measurement points

The best-fit values for the α_2 coefficient are extracted at different W-recoil ranges. To make the results readily comparable with the theory, each measurement should be associated with a value of p_T^W such that if it were really described by the theoretical curve, the pair (p_T^W, α_2) would indeed lie on that curve.

There are two stages involved. Firstly, a particular range of the W-recoil does not corresponds to the same range of p_T^W, since the recoil is not a precise measurement of the W-boson transverse-momentum. The smearing and inefficiency in the calorimeters make the two quantities related by approximately a second-order polynomial with a Gaussian spread (see Sections 6.5 and 6.6). Therefore, the Monte Carlo is used to map a W-recoil range to the corresponding distribution of "true" p_T^W.

The second stage is to express α_2, measured over a distribution of "true" transverse-momenta, as a measurement at an effective $\hat{p}_T$ [83]. It is easy to show that the mean value ($\bar{p}_T$) of the p_T distribution ($f(p_T)$) is an approximate solution for $\hat{p}_T$. In fact, since it is plausible that the measured α (α_{meas}) is the average over p_T

with density $f(p_T)$:

$$\alpha_{meas} = \frac{\int f(p_T) \cdot \alpha(p_T) \mathrm{d}p_T}{\int f(p_T) \mathrm{d}p_T}, \tag{2}$$

and, by definition of $\bar{p}_T$:

$$\bar{p}_T = \frac{\int f(p_T) \cdot p_T \mathrm{d}p_T}{\int f(p_T) \mathrm{d}p_T}, \tag{3}$$

by expanding $\alpha(p_T)$ about $\bar{p}_T$:

$$\alpha(p_T) = \alpha(\bar{p}_T) + \left.\frac{\mathrm{d}\alpha(p_T)}{\mathrm{d}p_T}\right|_{p_T=\bar{p}_T} (p_T - \bar{p}_T) + ... \tag{4}$$

and substituting Equation 4 into Equation 2 leaves:

$$\alpha_{meas} \simeq \alpha(\bar{p}_T). \tag{5}$$

The correction due to the dropping of higher order terms in Equation 4 is small (the next-order term is proportional to $\mathrm{d}^2\alpha(p_T)/\mathrm{d}p_T^2$ and the SM expectation for $\alpha_2(p_T^W)$ is with good approximation a linear dependence between 10 and 80 GeV). The validity of this approximation is cross-checked with the Monte Carlo simulation of the measurement procedure, as detailed in Section 4.3. It can be shown that in general $\hat{p}_T$ satisfies the following equation:

$$\sum_n a_n \mu^{(n)} = \sum_n a_n \hat{p}_T^n \tag{6}$$

where $\mu^{(n)}$ are the n-th moments of $f(p_T)$ and a_n are the coefficients of the polynomial expansion of $\alpha(p_T)$.

Bibliography

[1] M. Wu *et al.*, Phys. Rev. **105**, (1957) 1413

[2] D.E. Groom *et al.*, The European Physical Journal **C15** (2000) 1

[3] Particle Data Group, http://pdg.lbl.gov/ (2002)

[4] The HERA facility, http://desyntwww.desy.de/hera/

[5] G. Arnison *et al.*, Phys. Lett. **166B** (1986) 484

[6] G. Arnison *et al.*, Europhys. Lett. **1** (1986) 327

[7] G. Bonner *et al.*, Phys. Lett. **122B** (1983) 476

[8] K. Borer *et al.*, Helv. Phys. Acta **57** (1984) 290

[9] G. Arnison *et al.*, Phys. Lett. **122B** (1983) 103

[10] G. Arnison *et al.*, Phys. Lett. **126B** (1983) 398

[11] G. Arnison *et al.*, Phys. Lett. **129B** (1983) 273

[12] G. Arnison *et al.*, Phys. Lett. **134B** (1984) 469

[13] G. Arnison *et al.*, Phys. Lett. **147B** (1984) 241

[14] C. Albajar *et al.*, Z. Phys. C − Particles and Fields **44** (1989) 15−61

[15] Cheng and Li, “Gauge Theory of Elementary Particle Physics”, Clarendon Press (1984)

[16] F. Mandl and G. Shaw, “Quantum Field Theory”, Wiley (1984)

[17] F. Halzen and A.D. Martin, “Quark and Leptons”, Wiley (1984)

[18] T. Affolder *et al.*, Phys. Rev. Lett. **87** 131802 (2001)

[19] F. Abe *et al.*, Phys. Rev. Lett. **81** (1998) 5754

[20] U.K. Yang, A. Bodek and Q. Fan, “Parton Distributions, d/u, and Higher Twists at High x”, Proceedings of the 33th Rencontres de Moriond: QCD and High-Energy Hadronic Interactions, Les Arcs, France, UR-1518 (1998)

[21] F. Abe *et al.*, Phys. Rev. **D64** 052001 (2001)

[22] R.K. Ellis, W.J. Stirling and B.R. Webber, “QCD and Collider Physics”, Cambridge University Press

[23] H. Haber *et al.*, hep-ph/9703391 (1997)

[24] G. Altarelli, CERN-TH.97-278 (1997)

[25] G.Abbiendi *et al.*, The European Physics Journal **C7** 407−435

[26] F. Bedeschi *et al.*, Nucl. Inst. and Meth. **A268** (1988) 50

[27] W. Blum and L. Rolandi, “Particle Detection with Drift Chambers”, Springer Verlag (1993)

[28] W. Riegler *et al.*, CDF note 5050 (1999)

[29] W. Orejudos, CDF note 5656 (2001)

[30] J. Bialek *et al.*, CDF note 4570 (1998)

[31] D. Khazins, "COT sense wire shape under electric field", CDF document (1998)

[32] JLC Physics Group, "Introduction to Helical Track Manipulations", CDF document (1997)

[33] A. Gordon, CDF note 4013 (1997)

[34] B. Ashmanskas and A. Mukherjee, CDF note 4456 (1998)

[35] M. Jacob, Lett. Nuovo Cimento **9** (1958) 826

[36] B. Abbott *et al.*, Phys. Rev. **D63** 072001 (2001)

[37] A.D. Martin *et al.*, Eur. Phys. J. **C4** (1998) 463

[38] E. Mirkes, Nucl. Phys. **B387** (1992) 3−85

[39] J.C. Collins and D.E. Soper, Phys. Rev. **D16** vol.7 (1977) 2219−2225

[40] A. Mukherjee, "CTC and VTX Tracking", (1995)

[41] W. Ashmanskas, A. Mukherjee, "CTC Alignment for Run Ib", CDF note 4456 (1998)

[42] F. Abe *et al.*, "The CDF II Detector Techinical Design Report", FERMILAB-Pub-96/390-E

[43] J. Mariiner *et al.*, "The Tevatron Run II Handbook", www document *http://www-bd.fnal.gov/lug/runII_handbook/RunII_index.html*

[44] "The Fermilab Main Injector Technical Design Handbook", www document *http://www-fmiinternal.fnal.gov/MI_Technical_Design/index.html*

[45] P. Azzi *et al.*, "SVX′: The new CDF Silicon Vertex Detector", Nucl. Inst. and Meth. **A360** (1995) 137

[46] A. Sill and CDF Collaboration, Nucl. Inst. and Meth. **A447** (2000) 1–8

[47] L. Balka *et al.*, "The CDF Central Electromagnetic Calorimeter", Nucl. Inst. and Meth. **A267** (1988) 272

[48] P. Schoessow *et al.*, Proc. DPF. Santa Fe (1984) 366

[49] K. Yasuoka *et al.*, Nucl Inst. and Meth. **A267** (1988) 315

[50] G. Ascoli *et al.*, Nucl. Inst. and Meth. **A268** (1988) 33

[51] G. Ascoli *et al.*, Nucl Inst. and Meth. **A268** (1988) 41

[52] J.D. Lewis *et al.*, "The 1992 CDF Muon System Upgrade", CDF note 2858

[53] D. Amidei *et al.*, Nucl. Inst. and Meth. **A269** (1988) 51

[54] T. Carroll *et al.*, Nucl. Inst. and Meth. **A263** (1988) 199

[55] G.W. Foster *et al.*, Nucl. Inst. and Meth. **A269** (1988) 93

[56] K. Byrum *et al.*, Nucl. Inst. and Meth. **A364** (1995) 144

[57] D. Ramos, PhD Thesis, Universidad de Zaragoza (1996)

[58] G. Cowan, "Statistical Data Analysis", Oxford University Press (1998)

[59] C. Stubenrauch, PhD Thesis, University Paris-Sud, note CEA-N-2532 (1987)

[60] W.J. Ashmanskas, PhD thesis, Univeristy of California at Berkeley, CDF note 4719 (1998)

[61] F.A. Berends, R. Pittau, R. Kleiss, Nucl.Phys. **B424** (1994) 308–342

[62] E. Barberio and Z. Was, Comput. Phys. Comm. **79** (1994) 291

[63] E. Barberio, B. van Eijk and Z. Was, Comput. Phys. Comm. **66** (1991) 115

[64] U. Baur, S. Keller and D. Wackeroth, Phys. Rev. **D59** (1999) 013992

[65] A. Gordon, PhD thesis, Harvard University, CDF note 4897 (1998)

[66] M. Lancaster, CDF note 4048 (1997)

[67] A. Gordon, CDF note 3994 (1996)

[68] M. Lancaster, CDF note 4046 (1997)

[69] M. Lancaster, CDF note 4048 (1997)

[70] Y.K. Kim, CDF note 4067 (1997)

[71] Q. Fan and A. Bodek, CDF note 3585 (1996)

[72] P.B. Arnold, R.P. Kauffman, Nucl. Phys. **B349** (1991) 381

[73] P.B. Arnold, M. Reno, Nucl. Phys. **B319** (1989) 37

[74] P.B. Arnold, M. Reno, R.K. Ellis, Phys. Rev. **D40** (1989) 912

[75] W.T. Giele, S. Keller, Phys. Rev. **D57** (1998) 4433

[76] M.H. Reno, University of Iowa preprint UIOWA-94-01, (1994)

[77] G.A. Ladinsky, C.-P. Yuan, Phys. Rev. **D50** (1994) 4239

[78] R.K. Ellis and S. Veseli, Nucl. Phys. **B511** (1998) 649

[79] R.K. Ellis, D.A. Ross, S. Veseli, Nucl. Phys. **B503** (1997) 309

[80] F. Abe *et al*, Phys. Rev. **D44** (1991) 29−44

[81] A.D. Martin, R.G. Roberts and W.J. Stirling, RAL-92-099 (1993)

[82] Lep WW Working Group, LEPEWWG/WW/99-01

[83] G.D. Lafferty and T.R. Wyatt, CERN-PPE/94-72 and MAN/HEP/94/3 (1994)